NOTICE

May 1980

(NASA-CR-163006) STUDIES IN OCCULTATION ASTRONOMY Final Report, 1 Feb. 1975 - 31 Mar. 1979 (Cornell Univ., Ithaca, N. Y.) 46 p HC A03/MF A01 CSCL 03A

N80-23227

Unclas

G3/89 18052

CORNELL UNIVERSITY

Center for Radiophysics and Space Research

ITHACA, N. Y.

FINAL TECHNICAL REPORT

to the

National Aeronautics and Space Administration

for

NASA Grant NSG 7126

"Studies in Occultation Astronomy"

February 1, 1975 to March 31, 1979

Principal Investigator: Professor Joseph Veverka

CENTER FOR RADIOPHYSICS AND SPACE RESEARCH
CORNELL UNIVERSITY
ITHACA, NEW YORK 14853

FINAL TECHNICAL REPORT

to the

National Aeronautics and Space Administration

for

NASA Grant NSG 7126

"Studies in Occultation Astronomy"

February 1, 1975 to March 31, 1979

Report prepared by: Prof. Joseph Veverka
Principal Investigator
May 1980

TABLE OF CONTENTS

ABSTRACT

This final report summarizes the major scientific results of the research carried out under NASA Grant NSG-7126.

I. INTRODUCTION

NASA Grant NSG-7126 supported a wide range of work in occultation astronomy under the direction of Professors J. Veverka and J. Elliot. The effort at Cornell was terminated in 1979, after Professor Elliot accepted a new position at the Massachusetts Institute of Technology.

2. MAJOR RESULTS

A) Observations of the 8 April 1976 Occultation of ε Gem by Mars

The results of this study were published in three papers:

- Occultation of ε Geminorum by Mars: Evidence of Atmospheric Tides (1977). Science, 195, 485-486.
- Martian Occultation of ε Gem as Observed from the C. E. Kenneth Mees Observatory (1978). Icarus 34, 182-187.
- Occultation of ε Geminorum by Mars. II. The Structure and Extinction of the Martian Upper Atmosphere (1977). Astrophys. J., 217, 661-679.

Copies of these three papers are included in Appendix 1.

B) Studies in Occultation Techniques

Two major papers resulted from this aspect of our investigation:

- Analysis of Stellar Occultation Data (1978). Icarus 33, 186-202.

- Uranus Occults SAO 158687 (1977). _Nature_ _265_, 609-611.

Texts of these two papers appear in Appendix 2.

C) _Studies of the March 1974 Occultation of Saturn by the Moon_

The results of this phase of our effort were published in two papers:

- Lunar Occultation of Saturn. II. The Normal Reflectances of Rhea, Titan, and Iapetus (1978). _Icarus_ _35_, 237-246.
- Lunar Occultation of Saturn. III. How Big is Iapetus? (1978). _Icarus_ _33_, 301-310.

These two papers are reproduced in Appendix 3.

In addition we have refined our analysis of the Titan observations obtained during this occultation. The initial analysis was published in _Icarus_ _26_, 387-407 (1975). The conclusions of our re-analysis are summarized in the following section.

D) _Re-Analysis of the 1974 Lunar Occultation of Titan_

Observations of the March 30, 1974, occultation of Titan by the moon are an important data set with which to compare models of Titan's atmosphere. Elliot _et al_. (1975, _Icarus_ _26_, 387-407) fitted the data assuming zero phase angle and using a Minnaert scattering law. They concluded that strong limb darkening was present and that Titan's diameter, D, $\gtrsim$ 5800 km.

We have extended the analysis with the following objectives:

1) to determine if assuming the proper occultation geometry modifies Elliot's conclusions,

2) to fit a variety of model ligh. .rves to the data,

3) to compare the occultation observations with observed limb-darkening laws for Jupiter and Saturn,

4) to determine the constraints that the observations might place on the wavelength dependence of acceptable limb-darkening models;

5) to investigate systematic effects and other sources of error.

Our conclusions are:

1) Elliot's results are almost unaffected by proper inclusion of the event geometry. The inferred diameter of Titan changes by only 15 km, although the residuals of the fit drop dramatically.

2) Of the many homogeneous models we tried, the Minnaert law, $I(\mu,\mu_o) = (\mu\mu_o)^k/\mu$ gave the lowest residuals, with formal error $k = 1.64 \pm 0.35$. All models which gave low residuals required very strong limb darkening ($k \leq 1$).

3) Observations of $I(\mu)$ for Saturn and Jupiter were used to produce model light curves which were fit to the observations. The observed limb darkening corresponds closely to a Lambert surface for Jupiter ($k = 1$), and slightly smaller k for Saturn. Neither model gave a good fit to the occultation data.

4) Observations of the geometric albedo (P_λ) and phase coefficient (β_λ) of Titan allow the parameters g and ω_o in the Henyey-Greenstein scattering model to be determined uniquely. For each wavelength observed, the corresponding g and ω_o were used to generate a model light curve which was then fit to the data. In each case, the corresponding limb darkening was much less than for the best Minnaert fit. Additionally, the trend of increasing limb darkening with increasing wavelength implied by the β_λ observations was not detectable in the individual channel data. No simple homogeneous model is capable of fitting the observations of P_λ, β_λ, and the occultation results. However, if the atmosphere of Titan is modelled as a patchy haze layer over a uniform cloud deck, all of the observations can be reconciled, with a suitable choice of model parameters, corresponding to a haze coverage of about 95 percent of the satellite, with clear patches over the remaining 5 percent. Although the model works reasonably well, it is difficult to imagine how clear patches could be maintained in a photochemical smog.

5) All of the preceding discussion assumes that the lunar limb is a straightedge over the 2 km horizontal distance subtended by Titan at the moon. A careful study shows that lunar

limb topography can in principle lower the fit residuals drastically, even if Titan is assumed to be a uniformly bright disk. However, the required lunar limb slopes are unrealistically steep, and individual channels of data do not give consistent results. Furthermore, if lunar topography were important, a detectable timing difference would be present for the separate observing stations. No such timing difference was found. We conclude that lunar topography can be very important in some observations, but that it is not responsible for the extreme limb darkening inferred from the observations.

An extensive analysis of the power spectrum of the residuals of the light curve shows that the light curve is quite asymmetric about its half-intensity point; more than can be explained by event geometry alone. We find that there is only a 10 percent chance of this being due to noise alone, and we conclude that the more likely explanation is that Titan's atmosphere is not homogeneous. If Titan were truly a Lambert surface, there is only a 7 percent chance that noise would simulate the much stronger limb darkening we obtain in our fits.

Thus, our principle conclusions are:

- Titan is strongly limb darkened, with $D \gtrsim 5800$ km.
- There is internal evidence in the data that Titan's atmosphere is inhomogeneous.
- The observations are inconsistent with any simple homogeneous model atmosphere which matches the P_λ and β_λ observations of Titan.

APPENDIX 1

Occultation of ε Gem by Mars: Evidence for Atmospheric Tides? (1977). Science 195, 485-486.

Martian Occultation of ε Gem as Observed from the C. E. Kenneth Mees Observatory (1978). Icarus 34, 182-187.

Occultation of ε Geminorum by Mars. II. The Structure and Extinction of the Martian Upper Atmosphere (1977). Astrophys. J. 217, 661-679.

Occultation of ε Geminorum by Mars: Evidence for Atmospheric Tides?

Abstract. *Temperature profiles of the martian atmosphere have been derived from airborne observations of the 8 April 1976 occultation of ε Geminorum. Within the altitude range from 50 to 90 kilometers, these profiles show peak-to-peak variations of 35°K with a vertical scale of 20 kilometers and represent evidence for strong tides in the martian atmosphere. However, more information is necessary to conclusively rule out a radiative explanation for the temperature variations.*

The martian occultation of ε Geminorum (visual magnitude = +3.1, spectral class G8Ib) on 8 April 1976 was observed with the 91-cm telescope aboard the National Aeronautics and Space Administration Kuiper Airborne Observatory, the first occultation observations made with this facility (*1*). High-quality light curves for both immersion and emersion were obtained simultaneously at three wavelengths (0.37, 0.45, and 0.75 μm) with a time resolution of 4 msec. A similar occultation of β Scorpii by Jupiter on 13 May 1971 yielded temperature and number density profiles of the jovian atmosphere (*2*), as well as a measurement of its He abundance (*3*). From our ε Gem occultation data we have obtained temperature, pressure, and number density profiles of the martian atmosphere and information about its composition from a differential refractivity measurement. Our result indicated that no more than 30 percent Ar (and N_2) is mixed with pure CO_2 (*4*) and is consistent with the low abundance of Ar and N_2 obtained by the Viking entry probe (*5*). In addition, we have obtained the wavelength dependence of the extinction of the martian atmosphere from the first observation of the central flash—a bright feature in the light curve that was recorded when ε Gem was aligned with the center of Mars (*1*). We report here the temperature profiles deduced from the occultation data, which were obtained above the martian coordinates 27°S, 331°W (immersion) and 28°N, 152°W (emersion) and cover an altitude range of about 50 to 90 km above the mean surface. These results are compared with those of Viking 1 (*5*) and with theoretical predictions of thermally driven tides in the martian atmosphere (*6*). The details of our observations, data analysis procedures, and other results are given elsewhere (*4*).

Temperature profiles were obtained from the occultation light curves with a new inversion procedure (*7*). This method is mathematically equivalent to standard inversion techniques (*2*, *8*) but has the advantage that error bars (calculated from the known noise in the light curve) can be assigned to the temperature profiles. Thus we can have confidence in separating those features in the temperature profiles that are caused by the martian atmosphere from the variations arising from the noise in the light curve.

The temperature profiles obtained are given in Figs. 1 and 2. The profiles are for the light curves at 0.45 μm, the channel with the best signal-to-noise ratio; the profiles from our other two channels agree within their errors. The upper boundary condition for the inversion is determined by an isothermal fit to the upper part of the light curve, indicated by the shaded region at the top of Figs. 1 and 2. The temperatures and their error bars are obtained from the inversion calculation matched to the boundary condition. For each temperature point the error bars represent ± 1 standard deviation expected from the noise in the light curve. Neighboring temperature points agree better than the error bars because the noise affecting the points is correlated (*7*). The inversion calculation is terminated when the uncertainty in the lower base line of the light curve produces an error as large as the random error.

Both the immersion and emersion profiles show peak-to-peak temperature variations of 35°K, much larger than variations expected from random noise. Temperature maxima occur at an altitude of about 55 to 60 km on both profiles. The mean temperature of the emersion profile is somewhat warmer than the mean for immersion. A temperature difference is to be expected from the difference in solar energy absorption, since the subsolar latitude is 19°N, close to the emersion latitude of 28°N, but 46° from the immersion latitude of 27°S. The mean temperatures for both profiles (as well as this quantity can be defined) agree with the mean temperatures obtained from Mars 6 (*9*) and Viking 1 entry data (*5*).

A striking similarity between the occultation temperature profiles and the Viking entry profile is the wavelike vertical structure with wavelength between two and three pressure scale heights and a peak-to-peak amplitude about 35°K at a number density of 10^{16} cm^{-3}, roughly eight scale heights above the 5-mbar pressure level. The wavelength and amplitude are in agreement with the general character of tidal waves predicted by Zurek (*6*) for clear (not dusty) conditions. Detailed comparison of temperature profiles, including phase information, with his predictions is not meaningful for several reasons. The details of profiles depend upon the amount and distribution of traces of dust in the atmosphere, and these factors are unknown. There may be significant additional forcing due to boundary layer convergence, neglected in Zurek's treatment. The large amplitude of the tides probably leads to instabilities and, as a result, to turbulence. Zurek pointed out that such turbulence would influence the structure of the tide but in a manner difficult to predict.

There are other possible explanations for the thermal structure. McElroy's detailed radiative equilibrium calculations (*10*) suggested that oscillations of temperature with height might occur near these levels on Mars because the concentration of (and solar absorption by) photodissociation products varies. Dütsch (*11*) discussed temperature variations in Earth's atmosphere caused by the stratification of photochemical products due to flow "fingering." Finally, aerosols have been observed by the Viking orbiter at heights as great as 40 km on Mars (*12*), and stratification into layers could lead to varying radiative heating with height. Purely thermal layering due to slowly varying (not tidal) large-scale flows is probably not a possibility, because radiative relaxation times are less than 1 day (*6*).

There is one point of disagreement between our data and Zurek's predictions, namely, the isothermal (not wavy) thermal structure above 70 km on emersion. However, radiative damping increases rapidly with height at these levels, and Zurek remarked that its influence is difficult to predict accurately.

We believe that the wavelength and amplitude of temperature variations shown by the data are best explained in terms of the existence of tides. A definitive test of this interpretation may be possible if several more temperature profiles of sufficiently high signal-to-noise ratio are available from other observers of the ε Gem occultation. These profiles, in conjunction with the Viking entry profiles, would provide information on the atmospheric temperature structure above different locations on Mars, which could be compared with the predictions of the tidal model.

J. L. Elliot, R. G. French
E. Dunham, P. J. Gierasch
J. Veverka, C. Church
Carl Sagan

Laboratory for Planetary Studies, Cornell University, Ithaca, New York 14853

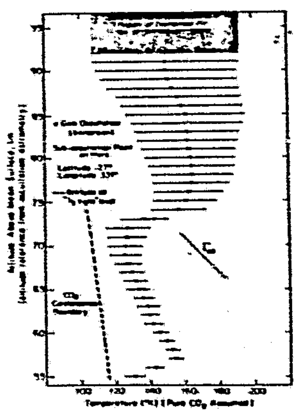

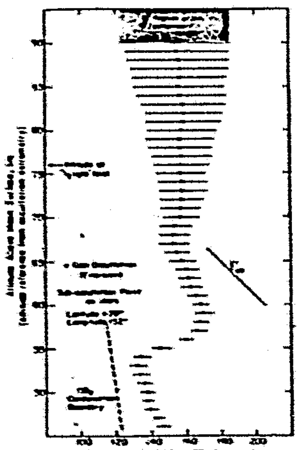

Fig. 1 (left). Temperature profiles for immersion. The plotted points and their error bars were obtained from the immersion light curve for a pure CO_2 atmosphere. A correction for the small amount of N_2 and Ar present would lower the temperatures about 3°K. The uncertainty in the altitude scale is ± 5 km, and an altitude of 65 km corresponds to a number density of 2.0×10^{16} cm^{-3}. The shaded region represents the uncertainty in the temperature obtained from the isothermal fit used to establish the boundary condition for the inversion calculation. The largest temperature gradients are subadiabatic (Γ_{ad} = −5°K km^{-1}). The wavelike structure strongly suggests the presence of tides in the martian atmosphere. At the time of the occultation, the martian subsolar latitude was + 19.2° and the planetocentric longitude of the sun (L_s) was 51.6°. Immersion occurred above the suboccultation point on Mars at about 0330 local solar time. Fig. 2 (right). Temperature profile for emersion, which occurred above the suboccultation point on Mars at about 1530 local solar time. For details, see the legend for Fig. 1.

References and Notes

1. J. L. Elliot, E. Dunham, C. Church, *Sky Telescope* 52, 23 (1976).
2. W. B. Hubbard, R. E. Nather, D. S. Evans, R. G. Tull, D. C. Wells, G. W. van Citters, B. Warner, P. Vanden Bout, *Astron. J.* 77, 41 (1972); L. Vapillon, M. Combes, J. Lecacheux, *Astron. Astrophys.* 29, 135 (1973); J. Veverka, L. H. Wasserman, J. L. Elliot, C. Sagan, W. Liller, *Astron. J.* 79, 73 (1974). An extensive critical review of the results of the β Scorpii occultation by Jupiter is given by D. M. Hunten and J. Veverka [in *Jupiter*, T. Gehrels, Ed. (Univ. of Arizona Press, Tucson, 1976), p. 247].
3. J. L. Elliot, L. H. Wasserman, J. Veverka, C. Sagan, W. Liller, *Astrophys. J.* 190, 719 (1974).
4. A preliminary report containing temperature, pressure, and number density profiles, as well as the composition and extinction results for the martian atmosphere from the ε Gem occultation was presented to the Viking Project in June 1976. These results are being submitted for publication (J. L. Elliot, R. G. French, E. Dunham, P. J. Gierasch, J. Veverka, C. Church, C. Sagan, in preparation).
5. A. O. Nier, W. B. Hanson, A. Seiff, M. B. McElroy, N. W. Spencer, R. J. Duckett, T. C. D. Knight, W. S. Cook, *Science* 193, 786 (1976).
6. R. W. Zurek, *J. Atmos. Sci.* 33, 321 (1976).
7. This method is described by R. G. French, J. L. Elliot, and P. J. Gierasch (in preparation) and requires the three assumptions necessary for inversion of the light curves: (i) the refractivity gradients in the martian atmosphere are parallel to the local gravity gradient, (ii) ray crossing is not severe, and (iii) the atmosphere is in hydrostatic equilibrium. J. Alcazar, G. de Vaucouleurs, D. S. Evans, R. E. Fisher, R. E. Nather, C. Palm, E. Silverberg, J. Wiant, W. B. Hubbard, and J. R. Jokipii (*Astrophys. J.*, in press) have reduced their ε Gem occultation data obtained at McDonald Observatory, assuming the lowest temperature fluctuations allowed in an isothermal atmosphere.
8. J. Kovalevsky and F. Link, *Astron. Astrophys.* 2, 398 (1969); L. H. Wasserman and J. Veverka, *Icarus* 20, 322 (1973).
9. V. V. Kerzhanovich, *Icarus*, in press.
10. M. B. McElroy, *J. Geophys. Res.* 74, 29 (1969).
11. H. U. Dütsch, *Adv. Geophys.* 15, 219 (1971).
12. M. H. Carr *et al.*, *Science* 193, 766 (1976).
13. We are extremely grateful to R. Cameron, C. Gillespie, J. McClenahan, and the rest of the staff of the Kuiper Airborne Observatory for their advice, cooperation, and assistance. We thank G. Taylor for supplying occultation predictions and star coordinates [illegible] for data reduction; A. T. Young, R. Zurek, R. Millis, L. H. Wasserman, and W. B. Hubbard for helpful discussions; and J. Goguen, M. Roth, and S. Arden for help in preparing for our observations. We thank D. M. Hunten, W. A. Baum, J. Pollack, S. I. Rasool, and N. Boggess for their interest and encouragement. We thank R. T. Fellows for prompt consideration of our proposal. Supported by NASA grant NSG-7202; partial support was also provided by NASA grants NGR 33-010-082, NGL 33-010-186, and NSG 7126, and by NSF grant MPS 75-04676. P.J.G. is supported in part by an Alfred P. Sloan Foundation research fellowship.

10 September 1976; revised 26 October 1976

Science, Vol. 195

ORIGINAL PAGE IS
OF POOR QUALITY

ICARUS 34, 182–187 (1978)

Martian Occultation of ε Gem as Observed from the C. E. Kenneth Mees Observatory

R. G. FRENCH AND J. D. GOGUEN

Center for Radiophysics and Space Research, Laboratory for Planetary Studies, Cornell University, Ithaca, New York 14853

AND

J. G. DUTHIE

Department of Physics and Astronomy, University of Rochester, Rochester, New York 14627

Received July 5, 1977; revised October 7, 1977

Ground-based observations of the occultation of ε Gem by Mars on April 8, 1976 have been reduced in the manner of French *et al.* [Icarus 33, 186–202 (1978)] to yield the scale height and temperature profiles of the Martian atmosphere for number densities between 10^{14} and 10^{16} cm^{-3}. The deduced variations in temperature are remarkably similar to those obtained by Elliot *et al.* [*Astrophys. J.* 217, 661–679 (1977)] and to the *in situ* measurements from the Viking landers.

I. INTRODUCTION

ε Geminorum ($m_v = +3.1$, Sp. G8I b) was occulted by Mars on 8 April 1976. Several observations of this occultation have been reported both by ground-based observatories (Wasserman *et al.*, 1977; Texas-Arizona Occultation Group, 1977) and by observers with the 91-cm telescope on the Kuiper Airborne Observatory (Elliot *et al.*, 1976, 1977). In this paper we present the observations obtained with the 60-cm telescope of the C. E. Kenneth Mees Observatory. From the immersion and emersion light curves we have determined accurate times of half-light, and temperature profiles of the Martian atmosphere were obtained by numerical inversion under the assumption that the density gradients are parallel to the gravity gradients (Elliot and Veverka, 1976). The correctness of this assumption has been challenged (Young, 1976; Jokipii and Hubbard, 1977). The present observations strongly support the model in so far as they produce differential temperature profiles remarkably similar to those produced from the airborne observations of the same event although the two observations probed regions more than 400 km apart in the Martian atmosphere. Similar, wavelike structures were observed during the entry of Viking 1 on 20 July 1976 (Nier *et al.*, 1976), and Viking 2 on 3 September 1976 (Seiff and Kirk, 1976).

II. OBSERVATIONS

Light curves of the occultation were obtained with one channel of our two-color photometer attached to the Cassegrain focus of the C. E. Kenneth Mees Observatory (latitude = +42°42!0, longitude = 77°24!5). The photometer channel had a

0019-1035/78/0341-0182$02.00/0

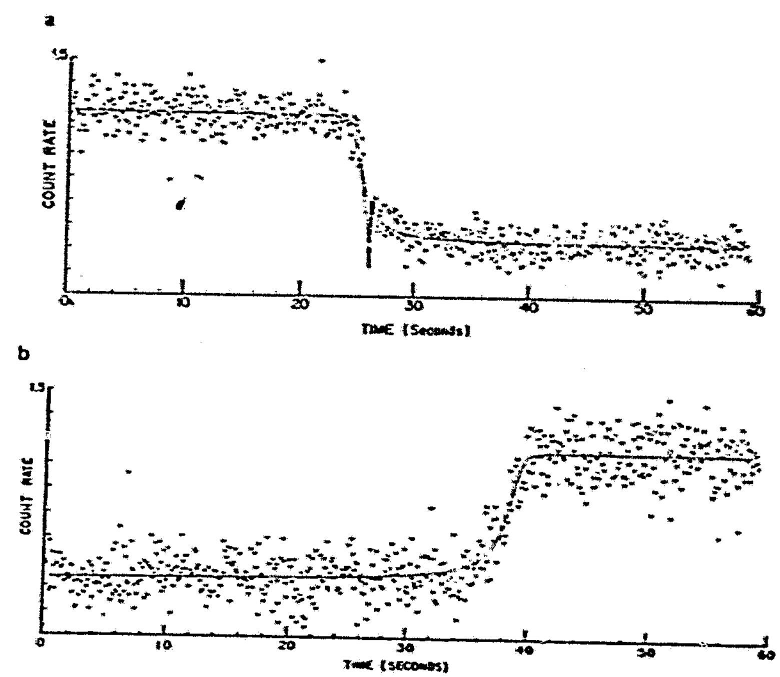

FIG. 1. Immersion and emersion light curves at 100-msec resolution. The count rate axis is incremented in units of 0.15 × 10⁵ photoelectrons per period. A zero of 5 × 10⁴ has been suppressed. In Fig. 1a the time starts at 00:56:15 UT while in Fig. 1b the time origin is at 01:01:15 UT. The arrow at 2.6 sec in Fig. 1a indicates the spike in the light curve.

central wavelength of 4500 Å and a bandwidth of 100 Å FWHM; identical filters were used by Elliot *et al.* (1977), Wasserman *et al.* (1977), and Groth *et al.* (1978). The phototube was operated in a pulse counting mode and the total photoelectric count was recorded, without interruption, every 10 msec. For the present analysis, data were averaged at 100-msec resolution. The data system clock was synchronized to within 2 msec of UT by comparison with signals from W.W.V. 4 hr before the event. Immediately following the observations the clock was again checked against W.W.V. and found to have remained within 2 msec of UT.

At the time of the occultation, both Mars and ε Gem were contained within an aperture 150 arcsec in diameter. Continuous data recording began at 0ʰ50ᵐ and ended at 1ʰ10ᵐ UTC. Figures 1a and b show the immersion and emersion events at 0.1-sec resolution. The data are considerably more noisy than those obtained from the Airborne Observatory, testifying to one of the advantages of using that platform for occultation observations. In addition, the present emersion light curve is considerably noisier than the immersion curve. Throughout the observation the photometric quality of the night degraded appreciably. As with the airborne observations, spikes in the light curve are much less pronounced than for previous occultations by Neptune and Jupiter (Elliot and Veverka, 1976). Nevertheless, the principal spike in the airborne data as given at $0^h57^m20^s.5$ UTC in Fig. 2. of Elliot *et al.* (1977) also appears in our ground-based data. This feature was also noted in the ground based observations of Wasserman *et al.* (1977).

III. RESULTS

The first step in the reduction process was to make a least-squares fit to an occultation curve assuming an isothermal atmosphere after the method of Baum and Code (1953). Parameters fit to this for both immersion and emersion are the mean photon count rates from Mars and from ε Gem, the half-light time, and the scale height divided by the perpendicular component of the Martian velocity. The results of this fit are given separately in Table I. The mean count rates so obtained defined the zero and unit stellar intensity levels which were used in the numerical inversion of the light curves. The half-light time is a useful quantity for occultation astrometry, and has been used to deduce the oblateness of the Martian atmosphere (Taylor, 1976). We attribute little significance to the isothermal fit value of the scale height; it has been shown (Wasserman and Veverka, 1973) that such fits can give badly erroneous mean scale heights.

We have calculated the temperature versus altitude for the Martian atmosphere in the manner discussed by Elliot *et al.* (1977). In so doing the following assumptions are made: (i) the density gradients in the atmosphere are parallel to the local gravity gradient; (ii) the atmosphere is in hydrostatic equilibrium; and (iii) ray-crossing is not severe. Under these assumptions, the desired profiles were obtained using the inversion technique of French *et al.* (1978).

TABLE I

RESULTS OF ISOTHERMAL FITS TO THE DATA OF FIGS. 1a AND b

Parameter[a]	Fit value	Fractional error[b]
Immersion		
$n_♂$ (sec^{-1})	5.34×10^6	0.0011
H/v_1 (sec)	0.501	0.107
n_* (sec^{-1})	8.28×10^4	0.0097
t_0[half-lt. time]	$00^h56^m40^s.36$ UT	±0.066 sec
	$H = 6.54 \pm 0.70$ km	
Emersion		
$n_♂$ (sec^{-1})	5.34×10^6	0.0015
H/v_1 (sec)	0.422	0.242
n_* (sec^{-1})	8.04×10^4	0.0157
t_0	$01^h01^m53^s.16$ UT	±0.128 sec
	$H = 9.17 \pm 1.39$ km	

[a] The parameters are the mean count rates $n_♂$ and n_* from Mars and ε Gem, respectively, half light time t_0, the atmospheric scale height H and the apparent velocity, v_1, of the star perpendicular to the level of Mars.

[b] The errors given are formal errors from the fit.

The temperature profiles for immersion and emersion are shown in Figs. 2a and b, respectively. The suboccultation coordinates on Mars are 18°S 332°W, and 35°N 151°W, respectively. The error bars have a total length of two standard deviations and reflect the uncertainty due to the known amount of shot noise present in the signal. The hatched region in the immersion profile corresponds to the region of the isothermal fit used to initiate the inversion, as discussed by French *et al.* (1978). Such a region is not shown for the emersion profile; because of the significantly higher noise level, the least-squares fitting routine was unable to find an isothermal fit unless the entire light curve was used. The formal errors are large; however, they do encompass the mean value of about 145°K found by Elliot *et al.* (1977), Wasserman *et al.* (1977), Viking 1

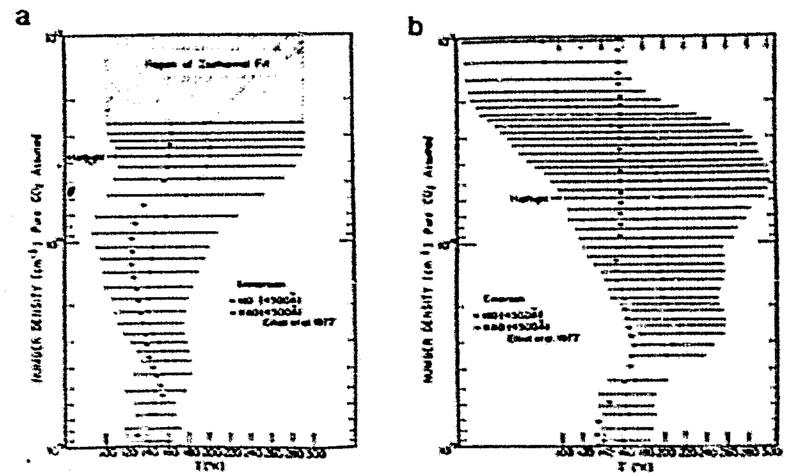

FIG. 2. Immersion and emersion temperature profiles obtained by numerical inversion of the occultation light curve. The uncertainty in the isothermal fit to the initial immersion data is shown in hatched area. The effects of random noise are shown by the error bars, which have a total length of two standard deviations. Because errors in successive points of the profile are highly correlated, short scale temperature gradients are more reliable than implied by the error bars, which more properly reflect uncertainty in the positioning of the profile. Successive points are separated by 1 km in altitude.

(Nier *et al.*, 1977), and Viking 2 (Seiff and Kirk, 1976). The temperature profiles obtained by Elliot *et al.* (1977) are shown for comparison.

Because relative temperature variations as a function of altitude are more accurate than absolute temperature profiles (Elliot *et al.*, 1977), we have fit linear temperature gradients to the temperature profiles of Figs. 2a and 2b. The deviations from the least-squares fit to a constant temperature gradient are shown in Figs. 3a and b, respectively. Also shown on these diagrams are the temperature variations obtained from the airborne data. The profiles are aligned in altitude relative to the altitude corresponding to the half-light point of each light curve. The remarkable similarity is readily apparent, especially for the immersion event. Pronounced wavelike structures are evident in both immersion and emersion profiles. We conclude that turbulence in the Martian atmosphere is of minor import in interpreting the ε Gem occultation light curves as opposed to the viewpoint of the Texas-Arizona Occultation Group (1977). This result fortifies the similar conclusion reached by Wasserman *et al.* (1977). We also conclude that the consistency of the results obtained by the present and previously reported work, both airborne and ground-based, confirms that wavelike temperature variations in the Martian atmosphere extend horizontally over distances of at least several hundred kilometers.

The similarity of the temperature profiles obtained by several workers implies that the light curves of the occultation are similar. A cross-correlation analysis of the residuals in the unprocessed light curves will be presented as part of a

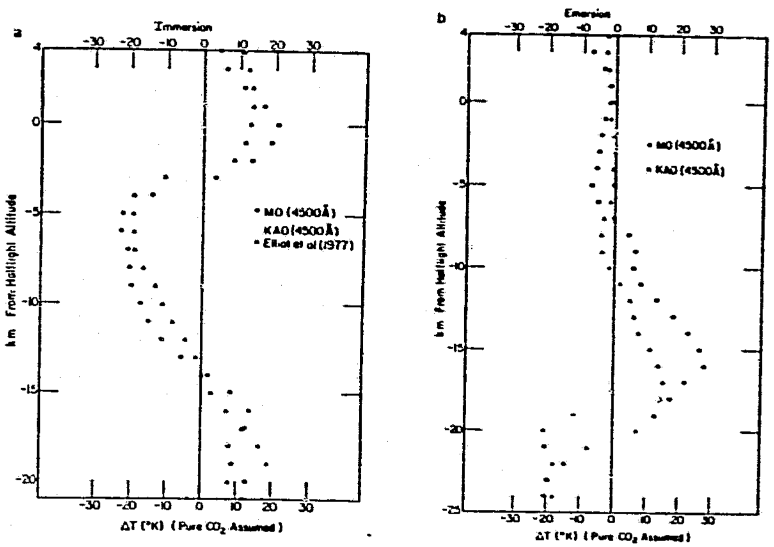

FIG. 3. Deviations of temperature profiles from a constant temperature gradient for immersion and emersion. For the altitude interval shown, a linear temperature gradient was fit to the temperature profile. ΔT is the deviation of the true profile from the fit at each point. The agreement with similar curves from Elliot *et al.* (1977) is excellent, particularly for the immersion event. This suggests that the wavelike temperature structures maintained their character over several hundred kilometers separating the points sampled by the two sets of observations.

detailed comparison, in preparation, of available observations of the ε Geminorum occultation.

ACKNOWLEDGMENTS

We wish to thank J. L. Elliot, who suggested that we observe the occultation. This work was supported in part by NASA Grant NSG-7126. R. A. Berg and K. Hardwick assisted in translating the data tapes and C. Bonapace made some preliminary sorting of the data.

REFERENCES

BAUM, W. A., AND CODE, A. D. (1953). A photometric observation of the occultation of σ Arietis. *Astron. J.* 58, 108–112.

ELLIOT, J. L., FRENCH, R. G., DUNHAM, E., GIERASCH, P. J., VEVERKA, J., SAGAN, C., AND CHURCH, C. (1976). The occultation of ε Geminorum by Mars: A pre-Viking assessment of results. Report prepared for Viking Project use.

ELLIOT, J. L., AND VEVERKA, J. (1976). Stellar occultation spikes as probes of atmospheric structure and composition. *Icarus* 27, 359–386.

ELLIOT, J. L., FRENCH, R. G., DUNHAM, E., GIERASCH, P. J., VEVERKA, J., CHURCH, C., AND SAGAN, C. (1977). Occultation of ε Geminorum by Mars. II. The structure and extinction of the Martian upper atmosphere. *Astrophys. J.* 217, 661–679.

FRENCH, R. G., ELLIOT, J. L., AND GIERASCH, P. J. (1978). Analysis of stellar occultation data: Effects of photon noise and initial conditions. *Icarus* 33, 186–202.

GROTH, E. J., KLOPFENSTEIN, J. B., WICKES, W. C., AND CALDWELL, J. J. (1978). The occultation of ε Geminorum by Mars as observed at Princeton. Submitted to *Astron. J.*

JOKIPII, J. R., AND HUBBARD, W. H. (1977). Stellar occultations by turbulent planetary atmospheres: The Beta Scorpii events. *Icarus* 30, 537–550.

NIER, A. O., HANSON, W. B., SEIFF, A., MCELROY, M. B., SPENCER, N. W., DUCKETT, R. J., KNIGHT, T. C. D., AND COOK, W. S. (1976). Composition and structure of the Martian atmosphere: Preliminary results from Viking 1. *Science* 193, 786–788.

SEIFF, A., AND KIRK, D. B. (1977). Structure of Mars' atmosphere up to 100 kilometers from the entry measurements of Viking 2. *Science* 194, 1300–1303.

TAYLOR, G. E. (1976). Oblateness of the atmosphere of Mars. *Nature* 264, 160–161.

Texas-Arizona Occultation Group (1977). The occultation of Epsilon Geminorum by Mars: Analysis of McDonald data. *Astrophys. J.* 214, 934–945.

WASSERMAN, L. H., MILLIS, R. L., AND WILLIAMON, R. M. (1977). An analysis of the occultation of ε Geminorum by Mars. *Astron. J.*, 82, 506–510.

WASSERMAN, L. H., AND VEVERKA, J. (1973). On the reduction of occultation light curves. *Icarus* 20, 322–345.

YOUNG, A. T. (1976). Scintillations during occultations by planets. *Icarus* 27, 335–358.

THE ASTROPHYSICAL JOURNAL, 217:661–679, 1977 October 15

OCCULTATION OF ϵ GEMINORUM BY MARS. II. THE STRUCTURE AND EXTINCTION OF THE MARTIAN UPPER ATMOSPHERE

J. L. ELLIOT, R. G. FRENCH, E. DUNHAM, P. J. GIERASCH, J. VEVERKA, C. CHURCH, AND CARL SAGAN
Laboratory for Planetary Studies, Cornell University
Received 1976 December 20; accepted 1977 April 13

ABSTRACT

The occultation of ϵ Geminorum by Mars on 1976 April 8 was observed at three wavelengths and 4 ms time resolution with the 91 cm telescope aboard NASA's G. P. Kuiper Airborne Observatory. Since most of the Earth's atmosphere was below the telescope, scintillation noise in the light curves was greatly reduced from that encountered by ground-based observers. Temperature, pressure, and number-density profiles of the Martian atmosphere were obtained for both the immersion and emersion events. Within the altitude range 50–80 km above the mean surface, the mean temperature is ~145 K, and the profiles exhibit wavelike structures with a peak-to-peak amplitude of 35 K and a vertical scale of about 20 km. The ratio of the refractivity of the atmosphere at 4500 Å and 7500 Å, determined from the time shift of the light curves for these wavelengths, is consistent with the atmospheric composition measured by *Viking 1*, 15 weeks later. From the "central flash"—a bright feature in the light curve midway between immersion and emersion—we find an optical depth at 4500 Å of 3.3 ± 1.7 per km atm (about 0.23 per equivalent Martian air mass) for the atmosphere about 25 km above the mean surface, near the south polar region. This large value and its weak wavelength dependence rule out Rayleigh scattering as the principal cause of the observed extinction.

Subject headings: occultations — planets: Mars — stars: individual

I. INTRODUCTION

The occultation of ϵ Geminorum ($m_v = +3.1$, G8 Ib) by Mars on 1976 April 8 was observed at three wavelengths with the 91 cm telescope aboard the Kuiper Airborne Observatory. A highlight of these observations was the discovery of the "central flash" when ϵ Gem was directly behind the center of Mars (Elliot, Dunham, and Church 1976). The records of the central flash yielded unexpected data on extinction in the Martian lower atmosphere—a new application for stellar occultation observations.

From the immersion and emersion light curves we have obtained temperature, pressure, and number-density profiles for the Martian atmosphere under the assumption that the density gradients are parallel to the gravity gradient. In the context of the β Scorpii occultation by Jupiter, the validity of this assumption has been disputed, and no evidence exists to settle the issue conclusively (Young 1976; Elliot and Veverka 1976; Jokipii and Hubbard 1977). The ϵ Gem occultation presents a unique opportunity to compare the structure and composition of the Martian upper atmosphere, obtained under the gravity-gradient assumption, with the in situ measurements made during the entry of *Viking 1*. A significant aspect of our analysis is the use of a new inversion technique (French, Elliot, and Gierasch 1977) that assigns error bars to the temperature, pressure, and number-density profiles.

II. OBSERVATIONS

Light curves of the occultation were obtained with our three-channel photometer (Elliot, Veverka, and Goguen 1975) attached to the bent Cassegrain focus of the 91 cm telescope aboard NASA's Kuiper Airborne Observatory (KAO). From the predictions by Taylor (1976*a*), the flight path was planned so that the apparent velocity of ϵ Gem was strictly perpendicular to the limb of Mars. This course was chosen to facilitate the analysis of the differential refractivity measurements (see § IV) but also resulted in the discovery of the "central flash" (see § V).

At the time of the occultation, the Martian subsolar latitude was +19°2 and the planetocentric longitude of the Sun (L_s) was 51°6. Immersion occurred at about 0330 local Martian time above the suboccultation point 27° S and 331° W longitude. The suboccultation point for emersion was 28° N, 152° W longitude, and the event occurred at about 1530 local solar time.

According to the inertial navigation system on board the KAO, the telescope was located at latitude 35°26'4 N and longitude 69°48'0 W at immersion and latitude 36°04'3 N and longitude 69°43'3 W at emersion. The times for immersion ($00^h57^m19^s68 \pm 0^s04$ UTC) and emersion ($01^h02^m34^s01 \pm 0^s04$ UTC) are defined to be the "half-light" times obtained by fitting an isothermal light curve to the data (Baum and Code 1953). Errors in the telescope coordinates, owing to uncalibrated internal errors in the inertial

TABLE 1

MEAN WAVELENGTHS AND PASSBANDS

Channel No.	Mean Wavelength (Å)	Passband (FWHM, Å)†	$n_s/(n\bar{c}+n_s)$ (ratio of counting rates)	$\epsilon(\phi)$ Normalized rms Noise (for 1 s integration)
1.	3800‡	(150)	0.09	0.013
2.	4500	100	0.17	0.007
3.	7500	200	0.12	0.008

† Full width at half-maximum.

‡ The filter used had a center wavelength of 3700 Å, but the steep spectrum of ϵ Gem in this region must be accounted for before the mean wavelength for this channel can be known precisely. For the present we have adopted 3800 Å as the mean wavelength for this channel.

navigation system, are probably less than 2'. For both events the altitude of the plane was 12.5 km above sea level; its ground speed of 0.22 km s^{-1}, on a heading of 357°, was only 1% of the shadow velocity (21.9 km s^{-1}; Taylor 1976*a*).

The center wavelengths and passbands of the three photometric channels are given in Table 1. The photomultiplier for channel 1 had an S-4 photocathode response while those for channels 2 and 3 had an S-20 response. Each was contained in an uncooled, *rf*-shielded housing. Because of the large photon fluxes incident on the photomultipliers, voltage-to-frequency converters (Dunham and Elliot 1977) were used instead of pulse amplifiers. The alignments of the photomultipliers and their respective field lenses were carefully adjusted to make the photometer response independent of the position of a source within the entrance aperture of the photometer. Deviations from an ideal flat response could cause errors in the light curve in the event of poor telescope tracking. In fact, throughout the observations the telescope tracking was excellent, as confirmed by watching the image of Mars on a television screen that monitored a portion of the light received from a beam splitter within the photometer.

The data were recorded as a continuous series of 4 ms integrations, made simultaneously in all three channels, with a data-recording system described previously (Elliot, Veverka, and Goguen 1975). The data system clock was synchronized with time signals from radio station WWV when the KAO made its closest approach to Boulder, Colorado, a few hours before the occultation.

At the time of the occultation, both Mars and ϵ Gem were contained within an aperture 90" in diameter. Continuous data recording began at 0030 and ended at 0116 UTC. A light curve of the entire event at 4500 Å is shown in Figure 1, at 1 s time resolution,

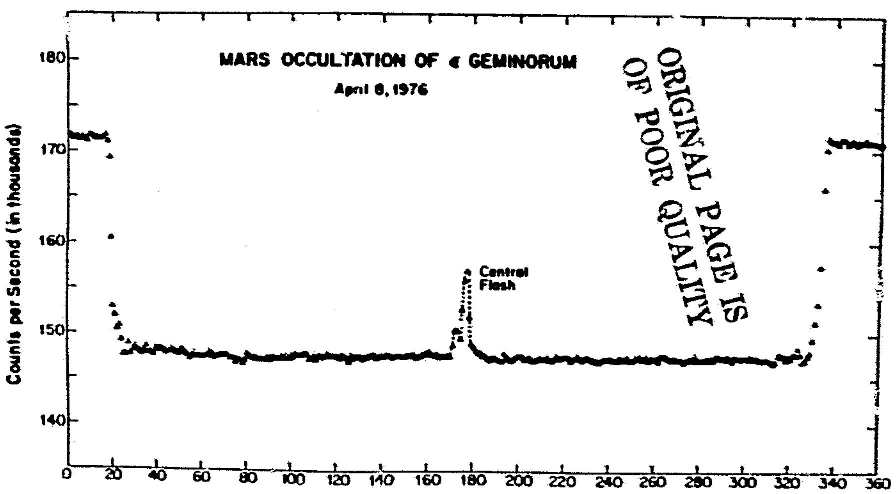

FIG. 1.—Light curve of the occultation obtained at 4500 Å; each point represents a 1 s integration. The central flash was produced by radially symmetric refraction when ϵ Gem was directly behind the center of the planet.

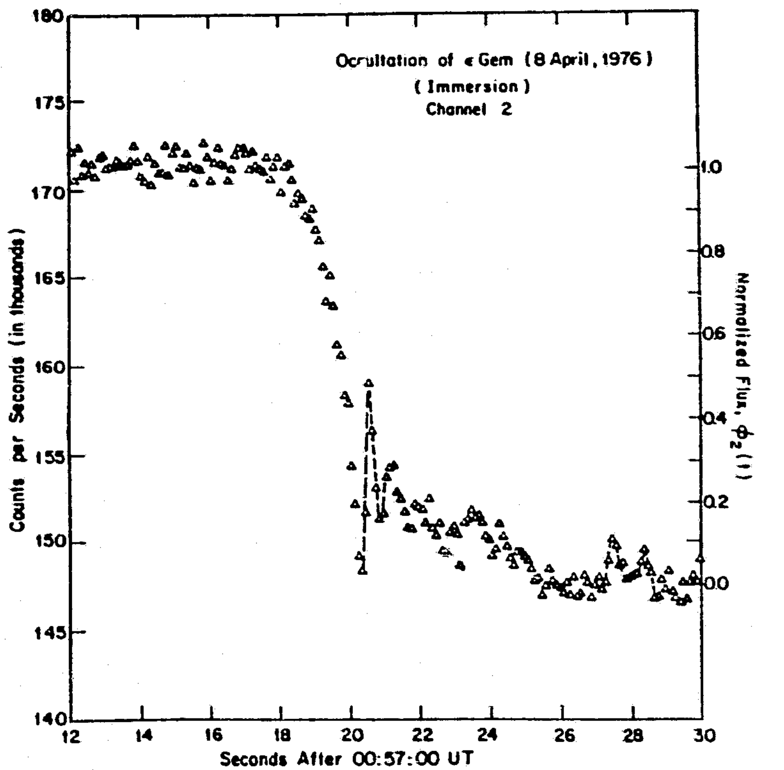

FIG. 2.—Immersion of ϵ Gem observed at 4500 Å; each point represents a 0.1 s integration. Prominent spikes are indicated by dashed lines.

where the central flash occurs exactly at mid-occultation. Figures 2 and 3 show light curves for immersion and emersion at 0.1 s time resolution. Spikes in the light curve are much less pronounced than for previous occultations by Neptune and Jupiter (Elliot and Veverka 1976), at least partially because of a large projected diameter of ϵ Gem at Mars (~6 km; de Vegt 1976).

Since our observations represent the first optical photometry performed with the airborne telescope, we shall briefly assess the photometric quality of the data. As seen in Figure 1, the baseline of the light curve is stable, showing little drift. The fourth column of Table 1 gives the ratio of the counting rate from ϵ Gem (n_*) to that from Mars (n_{σ}^{3}), and the background (n_b sky, dark counts, and v-to-f offset). For all channels $n_{\sigma}^{3} \gg n_b$. The fifth column gives the rms noise in each channel for a 1 s integration, expressed as a fraction of the counting rate from ϵ Gem. We denote this rms noise by $\epsilon(\phi)$ and compute it from several seconds of data before the occultation, when any variation in the data would be due to the noise only. If $n(t_j)$ is the mean counting rate for the jth integration bin of duration Δt (4 ms), N the number of integration bins, and $\bar{n}$ the average counting rate for all N integration bins, then

$$\epsilon(\phi) = \frac{(\Delta t)^{1/2}}{n_*}\left\{\frac{1}{N-1}\sum_{j=1}^{N}[n(t_j) - \bar{n}]^2\right\}^{1/2} . \quad (1)$$

We consider two sources as likely causes of the rms noise level $\epsilon(\phi)$: photon noise (shot noise), and terrestrial scintillation. We believe that photon noise, and not scintillation noise, makes the dominant contribution for the following reason. The level of scintillation noise from Mars and ϵ Gem for a telescope at 12.5 km altitude predicted by equation (2.1.6) of Young (1974) yields $\epsilon(\phi) \approx 0.004$ for our channel 2, which is less than the value calculated from the

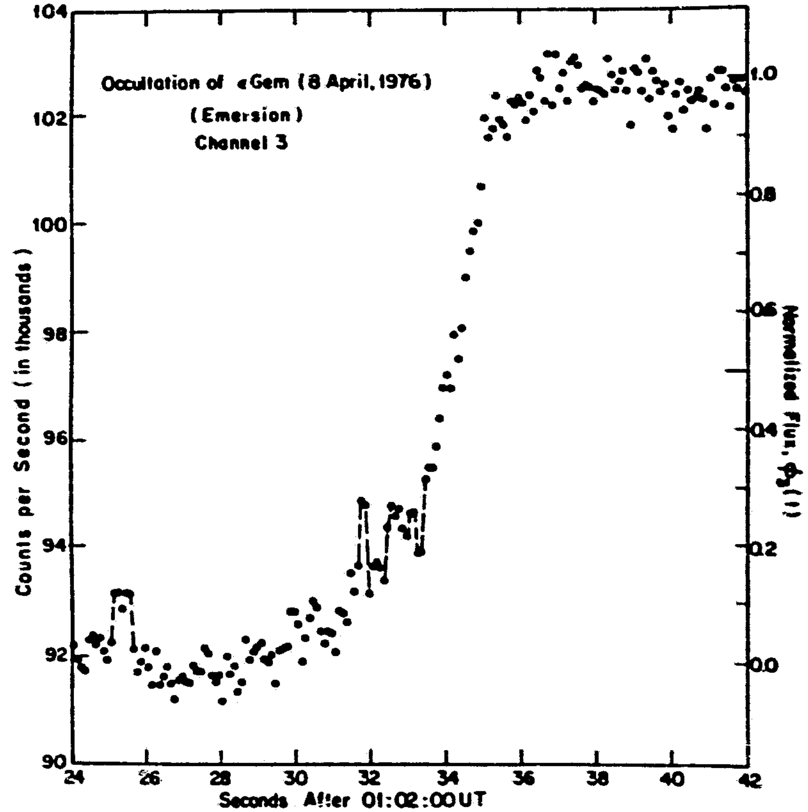

FIG. 3.—Emersion of ϵ Gem observed at 7500 Å; each point represents a 0.1 s integration. Prominent spikes are indicated by dashed lines.

observations (Table 1). Furthermore, the rms scintillation noise decreases exponentially with the altitude of the telescope above sea level. Hence Young's equation would also predict that a light curve for this occultation obtained from a ground-based telescope of similar aperture would have a rms noise level $\epsilon(\phi) = 0.02$ owing to scintillation alone. This would imply that the light curves obtained from ground-based telescopes would be about 3 times noisier than the airborne data, which appears to be confirmed (Wasserman, Millis, and Williamon 1977; Texas-Arizona Occultation Group 1977). Later, we hope to expand upon this necessarily brief discussion of noise encountered in airborne photometry.

III. TEMPERATURE, PRESSURE, AND NUMBER-DENSITY PROFILES

a) *Method*

When ϵ Gem was occulted by Mars, the process that caused the starlight to dim was differential refraction by the Martian atmosphere. From the light curves of Figures 2 and 3 we can obtain temperature, pressure, and number-density profiles for the Martian atmosphere if the following assumptions are satisfied: (i) the density gradients in the atmosphere are parallel to the local gravity gradient (i.e., perpendicular to the limb); (ii) the atmosphere is in hydrostatic equilibrium; and (iii) ray crossing is not severe (see § V of Elliot and

Veverka 1976). Under these assumptions we can obtain the desired profiles through the inversion technique of French, Elliot, and Gierasch (1977), which is similar to the "standard" inversion method (Kovalevsky and Link 1969; Hubbard *et al.* 1972; Wasserman and Veverka 1973), but has the advantage of assigning error bars to the temperature profiles. In the following discussion we use the notation for the occultation geometry shown in Figure 1 of French, Elliot, and Gierasch (1977).

From the observations we obtain the starlight intensity $\phi_\lambda(t)$ at a wavelength λ as a function of the time t. The intensity is normalized by the unocculted stellar intensity so that $\phi_\lambda(t)$ begins at 1.0 and drops to 0.0 for an immersion event. Invoking the assumptions of no ray crossing and no density gradients parallel to the limb, we can write an implicit equation for the time $t_\lambda(h - \Delta h)$ at which the asymptotic path of the starlight on the occultation curve has probed a level Δh deeper into the atmosphere at a previous time $t_\lambda(h)$:

$$\Delta h = v_\perp \int_{t_\lambda(h)}^{t_\lambda(h-\Delta h)} \phi_\lambda(t')dt' . \qquad (2)$$

In equation (2), $v_\perp$ is the apparent velocity of the star perpendicular to the limb of Mars. For the same shell of atmosphere of thickness Δh, the refraction angle $\theta_\lambda(h)$ changes by $\Delta\theta_\lambda(h)$:

$$\Delta\theta_\lambda(h) = \frac{-v_\perp}{D}\int_{t_\lambda(h)}^{t_\lambda(h-\Delta h)} [1 - \phi_\lambda(t')]dt' , \qquad (3)$$

where D is the Earth-Mars distance.

The function $\Delta\theta_\lambda(h)$ is the fundamental relation, obtained as a linear function of the occultation flux $\phi_\lambda(t)$, from which we can derive information about the Martian atmosphere. In addition to its dependence on refraction by the Martian atmosphere, $\phi_\lambda(t)$ contains noise that propagates into the values of Δh and $\Delta\theta_\lambda(h)$. If the noise that affects $\phi_\lambda(t)$ is Gaussian white noise (photon noise, for example), then $\sigma[\Delta h]$ and $\sigma[\Delta\theta_\lambda(h)]$, the rms errors for Δh and $\Delta\theta_\lambda(h)$, are given by

$$\sigma[\Delta h] = v_\perp\left[\int_{t(h)}^{t(h-\Delta h)} \sigma^2[\phi_\lambda(t')]dt'\right]^{1/2}$$

$$\sigma[\Delta\theta_\lambda(h)] = \frac{\sigma[\Delta h]}{D} , \qquad (4)$$

where the integrand is the variance of $\phi_\lambda(t')$ for the time interval dt'.

We can write an equation for the number-density profile, $n(h)$:

$$n(h) = \frac{2\mathscr{L}}{\pi(2R_p)^{1/2}\nu_{STP}(\lambda)}\int_h^\infty (h' - h)^{1/2}d\theta_\lambda(h') , \qquad (5)$$

where $\mathscr{L}$ is Loschmidt's number, R_p is the radius of Mars, and $\nu_{STP}(\lambda)$ is the refractivity of the atmosphere at STP. A similar integral can be given for the pressure profile $p(h)$ (French, Elliot, and Gierasch 1977):

$$p(h) = \frac{4g\bar{\mu}\mathscr{L}}{3\pi(2R_p)^{1/2}N_A\nu_{STP}(\lambda)}\int_h^\infty (h' - h)^{3/2}d\theta_\lambda(h') , \qquad (6)$$

where $\bar{\mu}$ is the (constant) mean molecular weight of the atmosphere, N_A is Avogadro's number, and g is the gravitational acceleration.

The atmospheric scale height $H(h)$ is defined by

$$H(h) = RT(h)/\bar{\mu}g , \qquad (7)$$

where R is the universal gas constant and $T(h)$ is the temperature profile. To write equations (5) and (6), we have assumed $R_p \gg H(h)$. Combining equations (5)–(7) and the perfect gas law $p(h) = n(h)RT(h)/\bar{\mu}$, we can write an equation for the scale height that is independent of the atmospheric composition:

$$H(h) = \tfrac{2}{3}\int_h^\infty (h' - h)^{3/2}d\theta_\lambda(h') \Big/ \int_h^\infty (h' - h)^{1/2}d\theta_\lambda(h') . \qquad (8)$$

Errors caused by the light curve noise enter into the values of $n(h)$, $p(h)$, and $H(h)$ through the integrands $d\theta_\lambda(h')$, and the magnitudes of the errors can be evaluated from the variances given by equation (4).

b) Application of the Method

To use the method outlined in the previous section we must first obtain the normalized occultation flux $\phi_\lambda(t)$. If t_j is the midtime of the jth 4 ms integration bin, then $\phi_\lambda(t_j)$ is given by

$$\phi_\lambda(t_j) = n(t_j) - [\alpha + \beta(t_j - t_0)]/n_* , \qquad (9)$$

where $n(t_j)$ is the mean counting rate for the jth integration bin, n_* is the unocculted counting rate for ε Gem, t_0 is an arbitrary reference time, α is the background counting rate at time t_0, and β is the slope of the background counting rate. The value of $\phi_\lambda(t)$ for any time t is found by linear interpolation between the two appropriate values of $\phi_\lambda(t_j)$.

The constants n_*, α, and β were determined by a least-squares fit to an occultation curve appropriate for an isothermal atmosphere (Baum and Code 1953)[1] to each of our six light curves. The data interval used for each fit was 60 s, commencing 20 s before "half-light" for the immersion curves and covering the equivalent time interval for the emersion curves. In the fits, the counting rates α, β, and n_*, the scale height H, and the "half-light" time $t_{1/2}$, were free parameters. The background slope β was found to be comparable with its formal error in all cases and was therefore fixed at 0.0, while the other four parameters were varied. Values of α and n_* (with $\beta = 0.0$) obtained from these fits were used to obtain $\phi_\lambda(t)$ from equation (9).

[1] Although eq. (11) given by Baum and Code (1953) does not include the lateral focusing effects of a spherical planetary atmosphere, French *et al.* (1977) show that the resulting error introduced into the values of $n(h)$, $p(h)$, and $H(h)$ is negligible.

To evaluate the two fundamental integrals appearing in equations (5), (6), and (8), we have adopted the procedure of French, Elliot, and Gierasch (1977). First we obtained the $\Delta\theta(h)$ relation from the data by using equation (3) for equal Δh intervals of 1.0 km. Then two values of h were chosen: h_{max} [corresponding to $\phi_\lambda(t) \approx 0.99$] and h_0 [corresponding to $\phi_\lambda(t) \approx 0.7$]. The function $\Delta\theta(h) = (\theta_0/H)e^{-h/H}\Delta h$ (valid for an isothermal atmosphere of scale height H) was fitted by least squares to the values obtained from the data over the interval $h_0 \leq h \leq h_{max}$. The two free parameters in the fit were H and $\theta_0 H^{1/2}$, chosen to be independent. Our preference for this method over previous ones for establishing the boundary condition to begin the inversion calculation is explained in detail by French, Elliot, and Gierasch (1977).

The desired integrals were then evaluated in two parts. For $h_0 \leq h' < \infty$ the integrand was computed from the fitted $\Delta\theta(h)$ relation, and for $h \leq h' \leq h_0$ the integrand was computed from the $\Delta\theta(h)$ values obtained directly from the data. The errors in $n(h)$, $p(h)$, and $H(h)$ were computed with equations (21), (23), and (25) of French, Elliot, and Gierasch (1977).

Values used for the mean molecular weight $\bar{\mu}$ and the refractivity ν_{STP} are those for pure CO_2 gas (Old, Gentili, and Peck 1971). In addition to CO_2, the *Viking I* lander found the atmosphere near the surface to contain 1%–2% argon and 2%–3% nitrogen (Owen and Biemann 1976). If the larger of these values applies to the atmosphere probed by the occultation events, then $\bar{\mu}$ and ν_{STP} for the Martian atmosphere are 1.3% and 1.8% less than the values for pure CO_2 gas. Hence our derived number densities will be 1.3% low, the temperatures 1.8% high, and the pressures 0.5% high.

c) Results

The number-density profiles obtained from equation (5) are shown in Figure 4 for the three immersion light curves and Figure 5 for the emersion light curves. The profiles have been dashed for altitudes greater than h_0

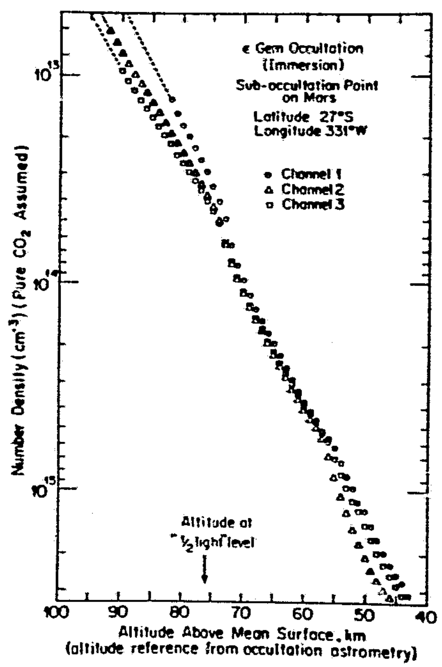

FIG. 4

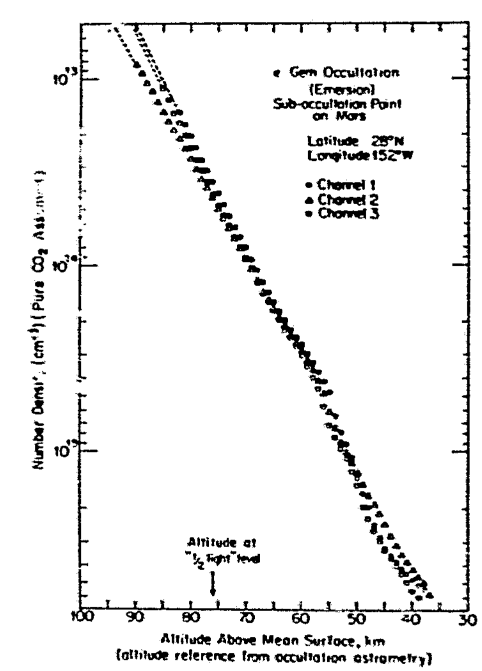

FIG. 5

FIGS. 4, 5.—Number-density profiles of the Martian atmosphere obtained by numerical inversion of the occultation light curve. The "half-light" altitude is estimated from occultation astrometry, and may be in error by several kilometers (see text). Internal and systematic errors are smallest in the region from 50 to 70 km. The dashed lines are computed from an isothermal fit to the initial data in each channel. As noted in the text, if the atmospheric composition measured by *Viking I* lander (95% CO_2, 3% N_2, and 2% Ar; Owen and Biemann 1976) applies to the occultation level, the number densities shown here are 1.3% too low, the temperatures 1.8% too high, and the pressures 0.5% too high.

(region of the isothermal fit). The altitude scales for these and subsequent figures were obtained from a preliminary astrometric solution (Taylor 1976*b*).

The zero points for the immersion and emersion altitude scales are 3401 ± 5 km and 3404 ± 7 km from the center of Mars. From these values our altitude scales can be related to the altitude above the true surface for any model of the surface figure. The accuracy of the relative altitude scales for the same event but different channels depends on the integration of occultation light curve (eq. [2]); these should have errors of only 1–2 km. For clarity we have not plotted error bars on Figures 4 and 5, but the scatter of the values for the three different channels gives a good indication of the magnitude of the errors. Near the top of the profiles the errors are the largest. Then they decrease, reaching their minimum value (~3%) for number densities which correspond to an altitude of ~60 km before increasing again. The uncertainty in the baseline (α) of the occultation curve also causes an additional error in the profiles for low altitudes. We have ended our plots at levels where we believe the error caused by baseline uncertainty about equals the error caused by shot noise in the light curve.

Figures 6 and 7 show the pressure profiles for immersion and emersion obtained from equation (6). The behavior of the errors in these profiles is similar to that for the number-density profiles discussed above.

In Figures 8 and 9 we have plotted temperature versus number-density profiles for our light curves at 4500 Å; these had the lowest noise level (see Table 1). The shaded portion of the figure corresponds to altitudes greater than h_0, the region of the isothermal fit. The portions of the light curves required to generate these profiles are the segments shown in Figures 2 and 3. The error bars have been calculated from the light curve noise as described in the previous section. Since the noise that affects neighboring points in the profile is correlated, the random scatter of neighboring points is much less than the absolute error in temperature for each point (indicated by the error bars). The profiles show wavelike variations, with peak-to-peak amplitudes of ~35 K and a vertical scale of 20 km. These

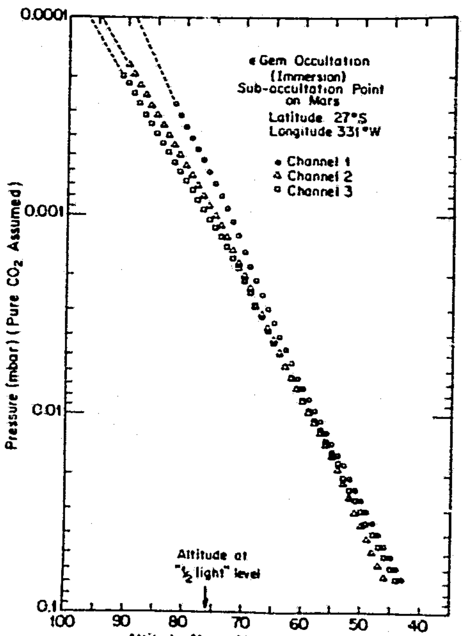

FIG. 6

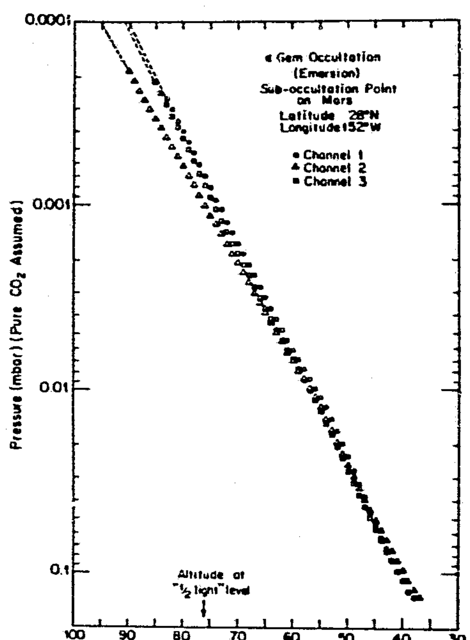

FIG. 7

FIGS. 6, 7.—Pressure profiles of the Martian atmosphere obtained by numerical inversion of the occultation light curve. The "half-light" altitude is estimated from occultation astrometry, and may be in error by several kilometers. Internal and systematic errors are smallest in the region from 50 to 70 km. The dashed lines are computed from an isothermal fit to the initial data for each channel.

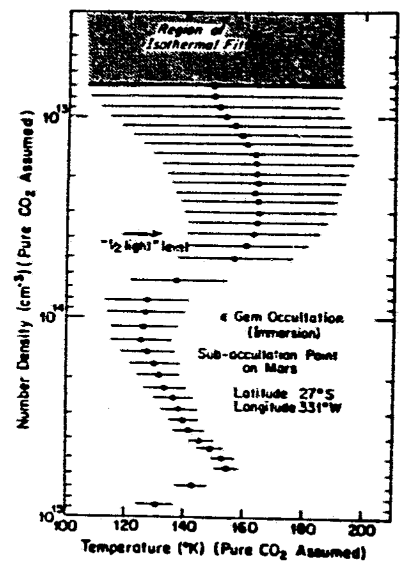

FIG. 8

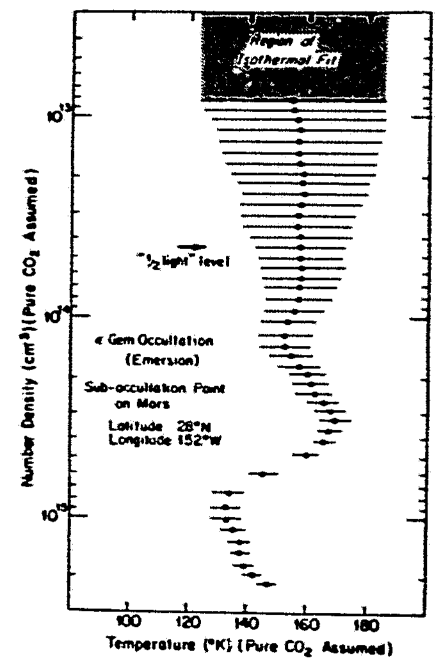

FIG. 9

FIGS. 8, 9.—Immersion and emersion temperature profiles obtained by numerical inversion of the channel 2 occultation light curve. The uncertainty in the isothermal fit to the initial data is shown dashed. The effects of random noise are shown by the error bars, which have a total length of two standard deviations. Because errors in successive points of the profile are highly correlated, short-scale temperature gradients are more reliable than implied by the error bars, which more properly reflect uncertainty in the positioning of the profile.

variations clearly exceed any that could be attributed to noise.

Temperature versus altitude profiles for all three channels are shown in Figures 10 and 11. The errors for each channel are proportional to the rms noise for that channel $\epsilon(\phi)$ (Table 1; French, Elliot, and Gierasch 1977), so that the error bars for channel 1 are about twice as large as those for channel 2 (see Figs. 7, 8); the errors for channel 3 are comparable with those for channel 2. The profiles mutually agree within their error bars.

The temperature *variations* on these profiles show better agreement than the absolute temperatures, because the variations are not sensitive to the large initial errors which affect the profile for several scale heights. Since the errors in successive points are correlated, short-scale temperature gradients are more reliable than implied by the error bars, which more properly reflect the uncertainty in the positioning of the profiles.

To see how well the short-scale temperature variations agree among the profiles for our three channels, we have removed a linear temperature fit from each profile. We write the temperature $T(h)$ in the following form:

$$T(h) = \left[\bar{T} + \overline{\frac{dT}{dh}}(h - \bar{h})\right] + \Delta T(h), \qquad (10)$$

where $\bar{T}$ is the mean temperature and $\overline{dT/dh}$ is the mean temperature gradient over an altitude interval that has a mean altitude $\bar{h}$. The quantity $\Delta T(h)$ is the difference between $T(h)$ and the linear function in brackets (eq. [10]).

For each temperature profile we fit by least-squares for $\bar{T}$ and $\overline{dT/dh}$ over the altitude interval 55–80 km for the immersion profiles and 42–80 km for the emersion profiles. The (unweighted) average of the $\bar{T}$'s obtained from the three immersion profiles was 143 ± 11 K, and the average $\bar{T}$ for the emersion profiles was 146 ± 9 K. The mean temperature gradients obtained from the fits were 0.4 ± 0.7 K km⁻¹ and −0.3 ± 0.5 K km⁻¹ for immersion and emersion. Clearly, these values depend on the altitude interval

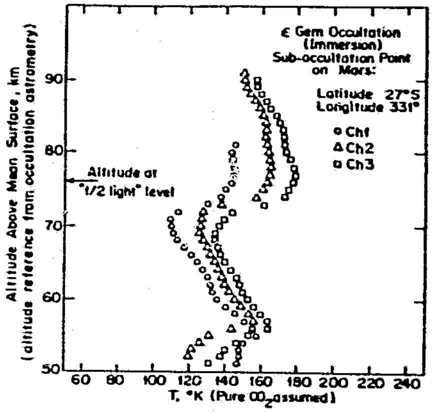

Fig. 10

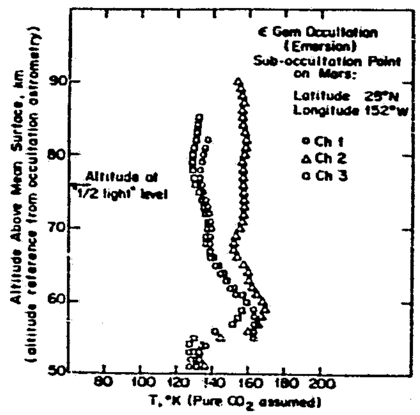

Fig. 11

Figs. 10, 11.—Immersion and emersion temperature profiles obtained by numerical inversion of the occultation light curve. Internal and systematic errors are smallest between number densities of 2×10^{16} and 2×10^{13} cm^{-3}. Large-scale temperature variations with height are evident in all of the profiles. The largest temperature gradients are subadiabatic. The altitude corresponding to these measurements may be estimated from Figs. 4 and 5.

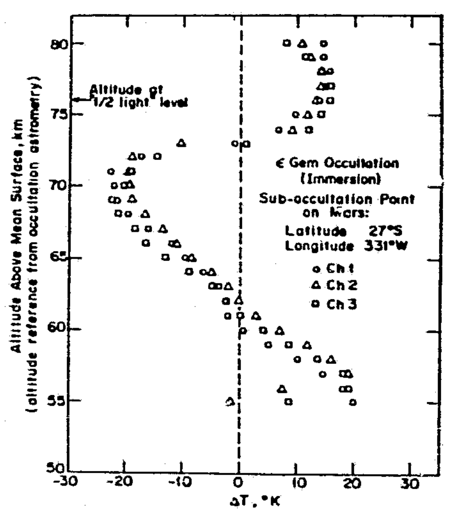

Fig. 12

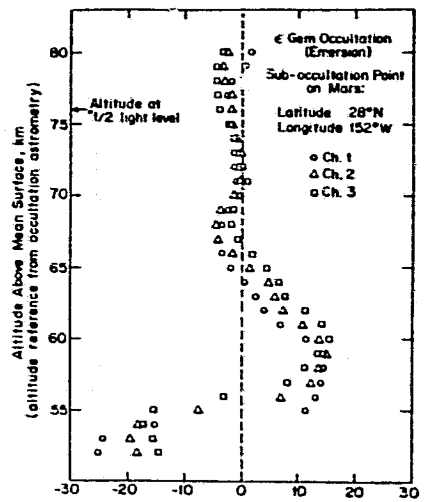

Fig. 13

Figs. 12, 13.—Deviations of temperature profiles from a constant temperature gradient for immersion and emersion. For the altitude interval shown, a linear temperature gradient was fitted to the temperature profile obtained for each channel. ΔT is the deviation of the true profile from the fit at each point. The agreement among channels is excellent, with an average rms dispersion of 2–3 K, except near the end points. Pronounced wavelike structures are evident in both immersion and emersion profiles.

used for the fit—particularly its relation to the phase of the wavelike structures. Hence from this analysis we conclude only that our "mean" temperatures for immersion and emersion are not significantly different and that we see no large-scale gradients greater than ± 0.7 K km^{-1}.

After subtracting the linear fits from the temperature profiles, we have plotted the temperature residuals $\Delta T(h)$ in Figures 12 and 13. The agreement among the three profiles is excellent, with an average rms dispersion of 2–3 K except near the end points. The wavelike structures appear in both figures. The main difference among the profiles is the nearly isothermal character of the emersion profiles above about 70 km. We note that the immersion and emersion profiles are nearly identical in their region of overlap if the emersion profile is displaced 17 km upward. The altitude difference is significant, since the difference in the zero points of the immersion and emersion altitude scales should be not more than 12 km (see previous discussion). Further support for this conclusion is found from examination of Figures 8 and 9 where we see that a temperature maximum occurs at a number density of 6×10^{14} cm^{-3} for immersion; for emersion, however, the temperature maximum nearest to this occurs at a number density of 3.5×10^{14} cm^{-3}. This comparison is independent of the altitude scales and shows that the phase of the wavelike temperature variations, relative to the number density of the atmosphere, differs for the regions of the atmosphere probed by the immersion and emersion events.

We emphasize that other data and models can be compared directly with the profiles of Figures 12 and 13 only after a linear temperature fit is subtracted (eq. [10]).

IV. REFRACTIVITY DISPERSION AND ATMOSPHERIC COMPOSITION

From our light curves we can determine the ratio of the refractivity of the Martian atmosphere at two wavelengths, and from this measurement place limits on the amount of gases other than CO_2 in the atmosphere. The precision of this technique is inferior to that of the methods used by *Viking 1* (Nier *et al.* 1976; Owen and Biemann 1976), but is comparable with the precision of other remote sensing methods used to determine the helium fraction of Jupiter's atmosphere (Hunten and Veverka 1976). Hence a comparison of our results with the more accurate measurements of *Viking* is an important test of the occultation method for determining the composition of planetary atmospheres.

During the occultation, refractive dispersion of the gases that compose the Martian atmosphere caused the light curve $\phi_i(t)$ at wavelength λ_i to be delayed by a time τ relative to the light curve $\phi_j(t)$ obtained at wavelength λ_j, so that

$$\phi_i[t + \tau(t)] = \phi_j(t) . \qquad (11)$$

The delay $\tau(t)$ is related to the refractivities of the atmosphere, ν_i and ν_j, at wavelengths λ_i and λ_j by the relation (derived from eqs. [6]–[9] of Elliot *et al.* 1974),

$$\tau(t) = \left(\frac{\nu_i}{\nu_j} - 1\right) \int_{-\infty}^{t} [1 - \phi_j(t')]dt' . \qquad (12)$$

The refractivity ratio ν_i/ν_j for the atmosphere is the ratio of the sum of the refractivities of its constituent gases. If $f(\mathrm{Ar})$ and $f(CO_2)[=1 - f(\mathrm{Ar})]$ are the fractions by number of argon and CO_2 in a CO_2–argon atmosphere, then

$$\frac{\nu_i}{\nu_j} = \frac{f(CO_2)\nu(CO_2, \lambda_i) + f(\mathrm{Ar})\nu(\mathrm{Ar}, \lambda_i)}{f(CO_2)\nu(CO_2, \lambda_j) + f(\mathrm{Ar})\nu(\mathrm{Ar}, \lambda_j)} , \qquad (13)$$

where the ν's are the refractivities of argon and CO_2 at wavelengths λ_i and λ_j. Fortunately, modern laboratory measurements of the refractivities of argon and CO_2 are available (Old, Gentili, and Peck 1971; Peck and Fisher 1964).

To use equation (13) we must also know the mean wavelengths of our three photometric channels, which are determined by combining the spectrum of ϵ Gem and the transmission profiles of the interference filters used. The mean wavelengths for channels 2 and 3 are nearly equal to the center wavelengths of the interference filters (Table 1), but the ultraviolet spectrum of ϵ Gem is steep, causing a significant and as yet undetermined shift of the mean wavelength of channel 1 to a larger value. Hence the light curve of channel 1 was not used in the present analysis.

For the Martian atmosphere, the refractivity ratio $\nu_3/\nu_2 - 1$ for $\lambda_2 = 4500$ Å, $\lambda_3 = 7500$ Å was determined by the following procedure. A portion of the light curve $\phi_2(t)$ (at 4500 Å) containing one or more spikes was selected for analysis, and for a test value of $\nu_3/\nu_2 - 1$, the time delays $\tau(t)$ were computed for each 4 ms integration bin with the aid of equation (12). The delays $\tau(t)$ were applied to the light curve $\phi_3(t)$ (at 7500 Å) to produce $\phi_3[t + \tau(t)]$. Then the sum of the squared differences, $\{\phi_2(t) - \phi_3[t + \tau(t)]\}^2$, was computed for 4 ms increments of t over the internal selected for analysis. The computation was carried out for test values of $\nu_3/\nu_2 - 1$ (in increments of 0.0005) within the range $-0.0300 \leq \nu_3/\nu_2 - 1 \leq -0.0100$. The test value that produced the minimum sum of squared differences was chosen as the best estimate of $\nu_3/\nu_2 - 1$ for that portion of the light curve.

The above procedure was applied to several regions of the immersion and emersion light curves that contained obvious spikes, and the resulting refractivity ratios are given in Table 2A. The error in their mean was computed from the internal consistency of the individual values. Next the procedure was applied to essentially the entire immersion light curve, from the beginning of the main intensity drop to the last major group of spikes, and to a corresponding interval of the emersion light curve. The refractivity ratios so obtained are given in Table 2B.

Since the two approaches to finding the refractivity are based on essentially the same data, we might expect somewhat better agreement between the two results. However, both are consistent with pure CO_2,

TABLE 2

REFRACTIVITY RATIOS FOR THE MARTIAN ATMOSPHERE

Event	Beginning of Fitted Segment (s after 00:57:00 UT)	Length of Fitted Segment (s)	Refractivity Ratio $[\nu(7500 \text{Å})/\nu(4500 \text{Å})] - 1$
A. Segments of Light Curves			
Immersion..............	20.0	8.6	−0.0208
Immersion..............	35.2	1.5	−0.0205
Immersion..............	51.0	0.8	−0.0225
Emersion................	322.4	11.3	−0.0205
Emersion................	315.4	1.2	−0.0185
		(Unweighted) Mean...	−0.0206 ± 0.0006
B. Major Portions of Light Curves			
Immersion..............	19.0	22.0	−0.0205
Emersion................	315.0	20.7	[illegible]
		(Unweighted) Mean...	−0.0215 ± 0.0010

for which $\nu_3/\nu_2 - 1 = -0.0209$ (−0.0169 for pure argon). Version (B) of our analysis has the advantage of including all the data but probably has a greater error, since the spikeless portions of the curves contribute noise but no refractivity information. Hence we prefer version (A) of our analysis, since it presumably has a smaller error. This value (−0.0206 ± 0.0006) has been plotted in Figure 14, along with curves for the refractivity ratios for various gases. Our measurement corresponds to an argon fraction by number, $f(\text{Ar})$, equal to 10%(+20%, −10%). We note that this value applies to any combination of nitrogen and argon, since the refractivity ratios for these two gases are nearly equal (see Fig. 14). The amounts of argon and nitrogen found by *Viking* are 1%–2% and 2%–3% (Owen and Biemann 1976), consistent with our result.

V. ATMOSPHERIC EXTINCTION AND THE CENTRAL FLASH

The discovery of the central flash, the bright feature in the occultation light curve midway between immersion and emersion, presents an unexpected opportunity to determine an average for extinction in the Martian atmosphere at lower altitudes than probed by the immersion and emersion events. We shall show that the flash was formed through symmetric refraction by the Martian atmosphere when ε Gem was directly behind the center of Mars; our calculations show that this light passed through the atmosphere about 25 km above the mean surface. The integrated density along this slant path equals about 4 Martian air masses. The most abrupt variation in our observations of the central flash is the sharp rise at 00:59:56 UTC (Fig. 16), which has a duration $\Delta t \sim 0.5$ s; this establishes a minimum distance scale for large intensity variations within the Martian shadow of $v\Delta t \approx 10$ km. Since this is much greater than the Fresnel scale (0.2 km), we believe that a geometrical optics treatment is adequate for a preliminary analysis. From the optics and the astrometry, we estimate the mean optical depth of the atmosphere at the altitude sampled by the flash, and, by comparing the integrated flux of the central flash at different wavelengths, we determine the wavelength dependence of the atmospheric extinction.

a) Intensity Profile of the Central Flash

i) Spherical Planet

For an occultation by a spherical planet with an isothermal atmosphere, Baum and Code (1953) have derived an implicit equation for the occulted stellar intensity which is valid only near the limb of the planet's shadow (i.e., the immersion and emersion events). Hence to obtain an intensity profile for the central flash, we must write an equation for the stellar intensity that is valid throughout the shadow. To do this we use the derivation of Baum and Code (1953), with two additional effects included: (i) the curvature of the limb perpendicular to the line of sight, which causes the convergence of the light rays at the center of the shadow, producing the central flash; and (ii) the additional contribution of light from the "emersion limb." For a point a distance ρ from the center of the shadow, we define the "immersion limb" to be the point on the shadow limb closest to ρ and the "emersion limb" to be the most distant. We shall derive an equation for the normalized stellar intensity, $\phi(\rho)$; $\phi(t)$ can be obtained when $\rho(t)$ is specified.

If the atmosphere of the planet has a scale height H, then $\phi(\rho)$ is given by the equation derived by French (1977),

$$\phi(\rho) = 2H/\rho + \phi_+[1 - H/\rho] - \phi_-[1 + H/\rho] . \quad (14)$$

The functions ϕ_+ and ϕ_- are the intensities from the immersion and emersion limbs that would be obtained by neglecting the effects of limb curvature and are

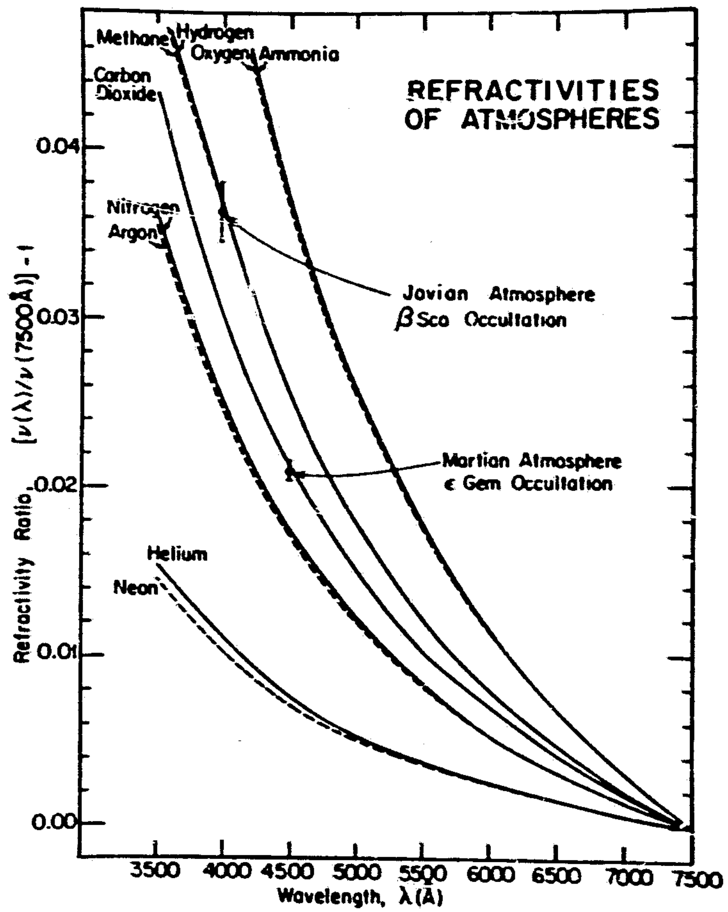

FIG. 14.—Refractivity ratio for the Martian atmosphere. The refractivity ratio $[\nu(\lambda)/\nu(7500 \text{Å})] - 1$ for various gases is plotted, along with the value measured from the ε Gem occultation. The result indicates an atmosphere with 10%(+20%, −10%) argon and/or nitrogen, a value consistent with the composition found by *Viking 1* (Owen and Biemann 1976). The refractivity ratio determined for the Jovian atmosphere from the β Scorpii occultation (Elliot *et al.* 1974) has also been plotted. For purposes of comparison with the present result, the value of $[\nu(6201 \text{Å})/\nu(3934 \text{Å})] - 1$ actually measured for Jupiter has been scaled to $[\nu(3934 \text{Å})/(7500 \text{Å})] - 1$.

given implicitly by Baum and Code's equation (11):

$$\rho_0 - \rho = H\left[\left(\frac{1}{\phi_+} - 2\right) + \ln\left(\frac{1}{\phi_+} - 1\right)\right] , \quad (15)$$

$$\rho_0 + \rho = H\left[\left(\frac{1}{\phi_-} - 2\right) + \ln\left(\frac{1}{\phi_-} - 1\right)\right] . \quad (16)$$

Here ρ_0 is the "half-light" radius of the shadow and is defined by $\rho_0 = \rho$ when $\phi_+ = \frac{1}{2}$.

Near the limb of the shadow, $\rho \gg H$ and $\phi_- \approx 0$. Making these approximations in equation (14), we find that $\phi(\rho) \approx \phi_+$, a result equivalent to Baum and Code's equation (11). Near the center of the shadow $\rho \approx H$ and $\phi_+ \approx \phi_- \ll 1$. From equation (14) we see that $\phi(\rho) \approx 2H/\rho$—the intensity of the central flash falls as ρ^{-1} away from its point of perfect geometrical focus in the center of the shadow.

The maximum intensity of the central flash is not infinite and will depend on the radius of the occulted star and diffraction, two effects not considered in the present model. If the stellar radius is the dominant effect and ρ_* is its projected radius at the distance of the planet from its shadow, then the maximum intensity at the center of the shadow is $4\,H/\rho_*$ for a uniformly bright stellar disk. The minimum intensity in the shadow occurs near $\rho = \rho_0/2$ and is approximately $16\,H/3\rho_0$. For the present occultation, this value is 0.016.

ii) *Oblate Planet*

Since Mars is significantly oblate, we have extended the model of the previous section to include this effect. The limb is assumed to be an ellipse, and consequently the radius of curvature varies from point to point along the limb. The locus of perfect focusing is no longer confined to the point $\rho = 0$, but forms a curve known as the evolute of the ellipse. To illustrate the situation, we refer to the ray optics diagram in Figure 15, where normals to the ellipse have been drawn at equal intervals along its perimeter; the evolute is seen as a concave diamond shape. However, the density of lines in Figure 15 is not a true indicator of the intensity throughout the shadow, since the decreasing intensity of each ray with increasing distance from the limb has not been illustrated.

If r_e and r_p are the equatorial and polar radii of the planet, the (x, y)-coordinates of the limb obey the equation for an ellipse,

$$\frac{x^2}{r_e^2} + \frac{y^2}{r_p^2} = 1\,, \tag{17}$$

and the (x, y)-coordinates of the corresponding evolute

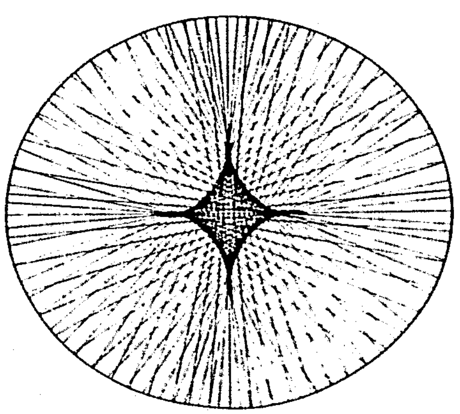

FIG. 15.—Ray tracing for the central flash. Surfaces of equal bending angle are assumed to be elliptical in shape. Density variations are assumed to be perpendicular to these surfaces, so that light is refracted along the normals to the ellipse. The intersections of these normals form a caustic curve—the evolute of the ellipse.

are obtained from the following implicit equation (Beyer and Selby 1976):

$$(r_e x)^{2/3} + (r_p y)^{2/3} = (r_e^2 - r_p^2)^{2/3}\,. \tag{18}$$

To calculate the intensity $\phi(x_0, y_0)$ for a point (x_0, y_0) within the shadow of an oblate planet, we used the following procedure. For each point (x_0, y_0) on the observer's path through the shadow, we find the points on the limb (x_i, y_i) whose normals intersect (x_0, y_0). After finding the distance d_i between (x_0, y_0) and (x_i, y_i), we calculate the intensity at (x_0, y_0) from Baum and Code's equation (11) for an atmosphere of scale height H. The intensity is then enhanced by the factor r_c/d, where r_c is the radius of curvature of the ellipse at (x_i, y_i) and d is the distance between (x_0, y_0) and the center of curvature of the ellipse at (x_i, y_i). Then the intensities from all points (x_i, y_i) on the limb whose normals intersect (x_0, y_0) are added to obtain $\phi(x_0, y_0)$. The procedure outlined involves exactly the same steps that were used to obtain the analytic solution $\phi(\rho)$ for a spherical planet (eq. [14]). Further details of the methods used for calculating $\phi(x_0, y_0)$ are given by French (1977).

In this model we have smoothed the central flash along the (x, y)-path (i.e., in one dimension only) by a triangular function that approximates the strip brightness distribution of ε Gem. If the atmosphere has a total optical depth τ through the path traversed by each ray, we can include this extinction effect by multiplying the entire profile by $e^{-\tau}$. Some of the light removed by extinction will in fact be scattered by the Martian atmosphere. Unless this scattering is strongly peaked at angles of a few arcsec (an unlikely possibility), this effect will not be important for our analysis.

b) *Atmospheric Extinction*

In the upper frame of Figure 16, we present light curves of the central flash at 0.1 s time resolution for all three wavelengths (Table 1). The values of the background intensity, α, and ε Gem intensity, n_*, used to obtain $\phi_\lambda(t)$ (eq. [9]) were the means of the values found for immersion and emersion. The lower frames of Figure 16 contain three model profiles of the central flash generated by the procedure described in the previous section. The path of the telescope relative to the evolute for each profile is shown in Figure 17. The shape of each profile was determined by five parameters: (i) $\epsilon = (r_e - r_p)/r_e$, the ellipticity of the model planet; (ii) ρ_m, the closest approach of the telescope path to the center of the planet; (iii) ψ, the angle between the telescope path and the shadow equator; (iv) H, the scale height of the model planet's atmosphere; and (v) τ, the optical depth of the atmosphere along the path traversed by the light rays, which is assumed to be the same for all rays. For all our model profiles we chose $H = 8$ km and varied τ to find the profile intensity scale that appeared to best fit the data.

For case A we adjusted all parameters except H to achieve the best agreement with the data. Note that

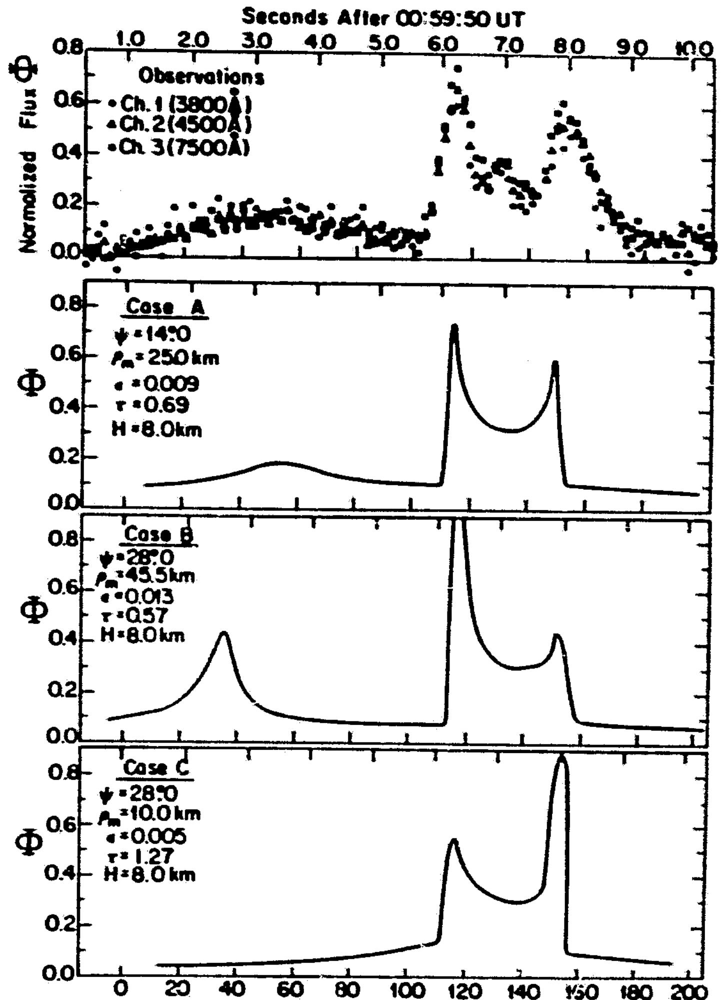

FIG. 16.—High time resolution data of the central flash and model central flash profiles. The relative areas under the profiles in the top frame provide information about the wavelength dependence of atmospheric extinction. Three model profiles are shown below, providing an estimate of the global atmospheric extinction along the slant path probed by the light which forms the central flash. The profiles have been smoothed by convolving with a uniformly bright stellar image with a radius of 3 km; ψ is the angle of the path of the telescope relative to the equator of the ellipse shown in Fig. 15, ρ_m is the closest approach of the path to the center of the ellipse, ϵ is the assumed oblateness of surfaces of equal bending angles, τ is the total optical depth through the atmosphere, and H is the scale height used in the calculation. The origin of the distance scale is arbitrary.

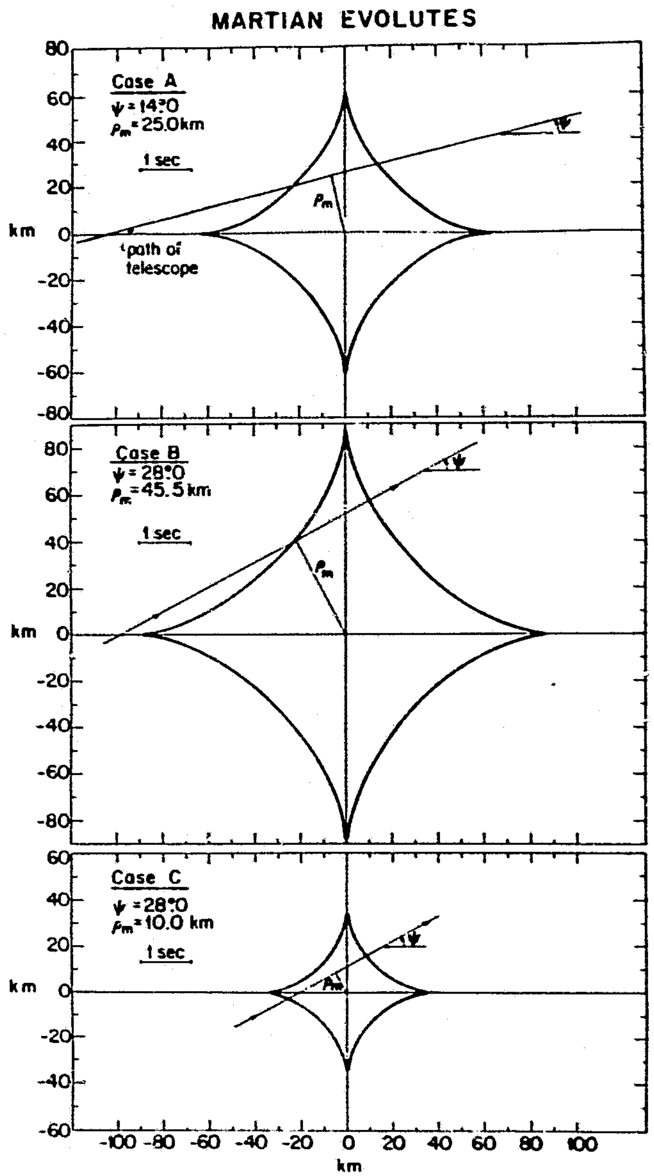

FIG. 17.—Martian evolutes, or loci of perfect focusing for rays refracted by an oblate planet with an isothermal atmosphere. The evolutes correspond to the concave diamond in the center of Fig. 15. The path of the telescope relative to the evolute is shown for each of the synthetic central flashes in Fig. 16. It is evident that the peaks in the synthetic profiles correspond to points nearest the evolute, where focusing is strongest.

the main features of the central flash can be reproduced: the broad wing at the left occurs when the path passes near a cusp of the evolute, and the two sharp peaks occur when the boundaries of the evolute are crossed.

For case B we set ψ and ϵ equal to the values indicated by the preliminary astrometric solution (Taylor 1976*b*), and adjusted ρ_m and τ for best agreement with the data. The last profile was obtained by fixing ψ at its value from the astrometric solution and fixing ϵ at 0.005, the ellipticity of the Martian surface (Christensen 1975). Again ρ_m and τ were varied to achieve the best fit to the data.

The values for ρ_m, ψ, and ϵ selected for the three model profiles would seem to bracket most reasonable possibilities, and these cases reproduce the main features of the data. Case A matches the data best, but the others use a more realistic value for ψ. We feel that the average optical depth τ along the path should lie somewhere between the extremes of cases A and C. For a definite value we chose the mean for these two cases, with error bars that include both extremes: $\tau = 0.90 \pm 0.45$. This is the total optical depth at 4500 Å along a slant path through the atmosphere sampled by the flash.

In order to relate this extinction to a definite column density of Martian atmosphere, we first write an equation for the number density $n(h_f)$ of the Martian atmosphere at the height h_f probed by the central flash,

$$n(h_f) = \frac{\mathscr{L} H^{1/2} \theta(h_f)}{\nu_{STP}(\lambda)[2\pi(R_p + h_c)]^{1/2}}\,. \tag{19}$$

We have assumed an isothermal atmosphere of scale height H, and the other quantities in equation (19) have been defined in § III. To evaluate equation (19), we note that at the center of the shadow the refraction angle of the light which forms the central flash is $\theta(h_f) = (R_p + h_c)/D$, and we make the approximation $h_f/R_p \ll 1$. For a CO_2 atmosphere, $\nu_{STP}(4500\ \text{Å}) = 4.55 \times 10^{-4}$, and letting $H = 8$ km, we find $n(h_f) = 1.75 \times 10^{16}\ \text{cm}^{-3}$. The main uncertainty in $n(h_f)$ is the scale height H, which must vary around the limb of the planet, for a $\pm 20\%$ variation in scale height $n(h_f)$ will be uncertain by $\pm 10\%$.

The column density $N(h_f)$ of atmosphere traversed by the light that forms the central flash is given by

$$N(h_f) = \frac{n(h_f)[2\pi(R_p + h_f)H]^{1/2}}{\mathscr{L}} = \frac{HR_p}{D\nu_{STP}(\lambda)}\,. \tag{20}$$

From equation (20) we find $N(h_f) = 0.27$ km atm[3] where again the main uncertainty enters through the scale height H. This value of $N(h_f)$ is equivalent to about 4 Martian air masses if we assume one Martian air mass to be 0.070 km atm (Young 1969). Hence the optical depth of 0.90 ± 0.45 is about 3.3 ± 1.7 per km atm, or about 0.23 ± 0.12 per Martian air mass.

Finally, we write an equation for the altitude of the atmosphere probed by the central flash:

$$h_f = \bar{H} \ln\left[\frac{n(0)}{n(h_f)}\right]\,, \tag{21}$$

where $n(0)$ is the number density at the mean surface and $\bar{H}$ is an average scale height between the surface and h_f. For $\bar{H} = 10$ km and a surface number density of $2.1 \times 10^{17}\ \text{cm}^{-3}$, we find $h_f = 25$ km. For different values of $n(0)$ and $\bar{H}$ that occur around the planet, h_f would lie in the range 20–30 km.

c) Wavelength Dependence of the Extinction

We can also determine the wavelength dependence of the optical depth by comparing the light curves of the central flash at different wavelengths. If $\tau(\lambda_i)$ is the optical depth of the Martian atmosphere for the ith channel (Table 1) and $\phi_i(t)$ is the normalized flux for that channel (eq. [9]), then the following equation holds:

$$\begin{aligned}\phi_1(t)\exp[+\tau(\lambda_1)/f(\lambda_1)] &= \phi_2(t)\exp[+\tau(\lambda_2)/f(\lambda_2)]\\ &= \phi_3(t)\exp[+\tau(\lambda_3)/f(\lambda_3)]\,,\end{aligned} \tag{22}$$

where $f(\lambda)$ is a function that accounts for the fact that each wavelength samples a slightly different altitude because of the variation of refractivity with wavelength (§ V). For these calculations we let $f(\lambda) = 1$. We adjusted the value of the optical depth difference, $\tau(\lambda_1) - \tau(\lambda_2)$, to minimize the squared difference between $\phi_1(t)$ and $\phi_2(t)$ within the time interval containing the central flash (from 00:59:46.9 to 01:00:02.9 UTC; see Fig. 16) and obtained the value $\tau(3800\ \text{Å}) - \tau(4500\ \text{Å}) = 0.06 \pm 0.03$. The same procedure applied to $\phi_2(t)$ and $\phi_3(t)$ yielded the optical depth difference $\tau(4500\ \text{Å}) - \tau(7500\ \text{Å}) = 0.13 \pm 0.02$.

We have plotted these results in Figure 18, where we see that the relative extinction at different wavelengths is determined much better than the absolute value. The wavelength dependence of the optical depth is weaker than calculated for Rayleigh scattering, and the lower bounds on the optical depths greatly exceed the Rayleigh scattering value. We conclude that other extinction processes—by haze, dust, or high-level water-vapor clouds—were dominant at the 25 km level of the Martian atmosphere at the time of our observations.

Although our model explains several features of the central flash, the best model profile does not fit the data within the uncertainties of the random noise on the light curves. To extend this analysis, values of ρ_m and ψ can be fixed when the final astrometric solution is available and the isothermal assumption can be replaced by a more realistic representation of horizontal and vertical temperature gradients. Also, since each segment of the central flash originates from a different region of the limb, it may be possible to obtain regional, rather than global, extinction information. The present astrometric solution (Taylor

[3] One km atm (kilometer atmosphere) is the thickness of the gas column in kilometers when compressed to standard temperature and pressure (i.e., 2.687×10^{24} molecules per cm²).

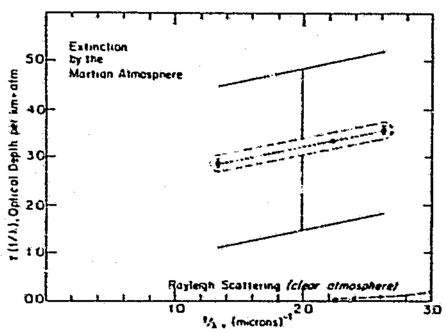

FIG. 18.—Extinction by the Martian atmosphere as a function of wavelength, determined from the central flash. The central flash probes the atmosphere along a slant path whose closest approach to the Martian surface is at an altitude of 25 km. This corresponds to a column density of about 4 Martian atmospheres. The large error bar represents the uncertainty in the absolute optical depth, estimated by comparing synthetic central flash profiles to the data. The small error bars show the uncertainty in the *relative* extinction from channel to channel, determined from relative fluxes of the central flash in each channel.

1976*b*) indicates that the airborne telescope passed north of the shadow center. For this path the preceding broad shoulder of the central flash was formed by light passing near the Martian equator (near 150° W longitude), while the light in the two larger peaks passed over the south polar region.

VI. DISCUSSION

The ϵ Gem occultation occurred just 15 weeks before *Viking I* entry experiments, which measured the structure of the Martian atmosphere within the same altitude range probed by the occultation. Before *Viking I* landed on Mars, the results of § IV and some of the results of §§ III and V were issued in a report (Elliot *et al.* 1976*b*). These results served to assure the *Viking* Project that the entry dynamics had been configured for a proper model Martian atmosphere. The number densities probed by the occultation event correspond to the critical level for the aerodynamic braking of an entry probe.

Now for the first time we can compare temperature profiles obtained from a stellar occultation with in situ measurements. The preliminary *Viking I* temperature profile (Nier *et al.* 1976) shows a mean temperature of ~130 K, slightly cooler than our values (~145 K), in the altitude range 50–80 km. Wavelike temperature structures, with a vertical scale of 20 km, appear on both our immersion and emersion profiles as well as the *Viking I* temperature profile. The pressure profiles from the occultation are comparable to that of *Viking I* (see Fig. 5 of Nier *et al.* 1976). As mentioned in § IV, the composition inferred from our measurement of the refractivity ratio agrees within its error to the composition determined by *Viking*. Our values of the extinction are comparable with those found by the *Viking* landers (Mutch *et al.* 1976*a*, *b*, *c*; Pollack 1976), but the *Viking* results on the wavelength dependence of the extinction are not yet available for comparison.

Since different regions of atmosphere were probed at different times by the occultation and *Viking I*, we would not expect precise agreement of the temperature profiles. More detailed comparison should be done on the basis of a model that describes the time and space behavior of the temperature of the upper atmosphere. But it is clear that the agreement of the mean temperatures and the qualitative features of the wavelike structures are significant evidence for the validity of both procedures.

In the context of the β Scorpii occultation Elliot and Veverka (1976) discuss the validity of two important assumptions used to obtain our present results—that ray crossing is not severe and that the density gradients are parallel to local gravity. For Jupiter they concluded that (i) at least some atmospheric structures that cause the spikes extend several km along the limb; and (ii) there is no compelling evidence to prove that the spike-producing structures either do or do not extend for several thousand km. Young (1976) proposed that the spikes and other irregularities in occultation light curves are caused by atmospheric turbulence, which must necessarily be anisotropic to explain certain features of the β Scorpii data. If Young's proposal is correct, the details of the temperature inversions obtained from the β Scorpii data would be indicative of turbulence, but not of any large-scale atmospheric structures. However, other quantities derived from the data on the basis of the gravity-gradient model (i.e., the [He]/[H_2] ratio and the diameters and separation of β Scorpii A_1 and A_2) would be essentially the same as would be obtained from an anisotropic turbulence model. On the basis of the same data, Jokipii and Hubbard (1977) argue for an isotropic turbulence model, which would discount all quantities derived from the β Scorpii data except for the mean temperature of the atmosphere obtained from isothermal fits. The McDonald Observatory observations of the ϵ Gem occultation have been analyzed in terms of the isotropic turbulence model by the Texas-Arizona Occultation Group (1977), who find a mean temperature of 190 ± 50 K—a mean value and probable error substantially greater than our results and the *Viking I* results.

We now consider what region of the atmosphere must have no horizontal refractivity gradients for our assumption to be satisfied for the purposes of inversion of the ϵ Gem data. As illustrated for the β Scorpii occultation by Jupiter in Figure 12 of Elliot and Veverka (1976), we see that at any given time the atmosphere causing 67% of the refraction is in the shape of a "squashed cylinder" (refraction cylinder) with its long axis along the line of sight. For the ϵ Gem occultation, the length of the cylinder is $2(R_p H)^{1/2} \approx$ 300 km, and its diameter about 6 km (the projected diameter of ϵ Gem at Mars) when the occultation begins. The axis of the cylinder perpendicular to the

limb decreases by the factor ϕ (normalized occultation flux) as the occultation proceeds. Since the airborne telescope was arranged to be on the center line, the motion of the refraction cylinder parallel to the limb was only a few km. The refraction cylinder extended almost exactly along a parallel of Martian latitude, and its length was about 6° of longitude.

Large-amplitude waves with long horizontal and vertical wavelengths satisfy all the assumptions of the spherical shell model used to invert the light curves. Large amplitudes allow identification of the waves in the presence of random noise. Long horizontal wavelength implies that a given shell maintains its character over the entire path of integration, and long vertical wavelengths mean that the wave is associated with broad features in the light curve, and does not depend on detailed structure of a sharp spike.

One method of checking for horizontal refractivity gradients along longitudes is to compare the light curves and temperature profiles with other ϵ Gem occultation observations of sufficiently high signal-to-noise ratio (Wasserman, Millis, and Williamon 1977). This work is in progress.

Another check on our assumptions is to compare the direct measurements of atmospheric composition made by *Viking I*. Within the errors of the present occultation measurement, the occultation result (see Fig. 14 and § IV) agrees with the composition found by *Viking*. Hence we must conclude either that the method is insensitive to horizontal refractivity gradients (turbulence, for an example) or that the Martian atmosphere has small horizontal refractivity gradients.

VII. CONCLUSIONS

The Martian atmosphere probed by our occultation observations has temperatures within the range ~130–170 K for altitudes between 50 and 90 km above the mean surface. The wavelike structure of the temperature variations on a vertical scale of 20 km may be due to tides (Elliot *et al.* 1976*a*) or may represent the equilibrium atmospheric structure—perhaps arising from photochemical processes. The atmosphere extinction (at an altitude of 25 km) has a wavelength dependence too weak and a magnitude too large to be explained entirely by Rayleigh scattering.

The mean temperature, its wavelike structure, and the atmospheric composition inferred by our differential refractivity measurement agree with in situ measurements made by *Viking I*. We feel that this agreement strongly supports the use of occultations as reliable and inexpensive probes of planetary upper atmospheres. The technique seems particularly sensitive to variations in temperature that have a large horizontal scale but a vertical scale of 2 scale heights or less. Only the events of intrinsically high signal-to-noise ratio are potentially useful, and to obtain good temperature profiles and other information from these relatively rare events, light curves with low noise and stable baselines are essential.

In this regard, airborne observations offer the advantages of telescope mobility, reduced scintillation noise, and operation above possible clouds. For this particular occultation our temperatures, pressures, number densities, and differential refractivity measurement would have been at least 3 times noisier (due to scintillation), and the extinction information of the central flash would not have been obtained, had we observed from the ground—even using a large telescope.

We are extremely grateful to R. Cameron, C. Gillespie, J. McClenahan, and the rest of the staff of the Kuiper Airborne Observatory for their advice, cooperation, and able assistance. The central flash would not have been discovered without G. E. Taylor's reliable predictions, based on an accurate Martian ephemeris from JPL, and the skill of navigator Bob Morrison and pilot Ron Gerdes. We thank A. T. Young, R. Zurek, R. Millis, L. H. Wasserman, and W. B. Hubbard for helpful discussions, and J. Goguen, M. Roth, and S. Arden for help in preparing for our observations. We appreciate the interest in this project of D. M. Hunten, W. A. Baum, J. B. Pollack, and C. B. Leovy, and thank S. I. Rasool and N. W. Boggess for their encouragement. The observations would not have been possible without the rapid consideration of our proposal by R. F. Fellows, which resulted in NASA grant NSG 7243 to support this work. Partial support was also provided by NASA grants NGR 33-010-082, NGR 33-010-186, NSG 2174, and NSG 7126, and NSF grant MPS 75-06670. Peter J. Gierasch is supported in part by an Alfred P. Sloan Research Fellowship.

REFERENCES

Baum, W. A., and Code, A. D. 1953, *A.J.*, 58, 108.
Beyer, W. H., and Selby, S. M. 1976, *Standard Mathematical Tables* (24th ed.; Cleveland: CRC Press), p. 319.
Christensen, E. J. 1975, *J. Geophys. Res.*, 80, 2909.
de Vegt, C. 1976, *Astr. Ap.*, 47, 457.
Dunham, E., and Elliot, J. L. 1977, in preparation.
Elliot, J. L., Dunham, E., and Church, C. 1976, *Sky Tel.*, 52, 23.
Elliot, J. L., French, R. G., Dunham, E., Gierasch, P. J., Veverka, J., Church, C., and Sagan, Carl. 1976*a*, *Science*, 195, 485.
Elliot, J. L., French, R. G., Dunham, E., Gierasch, P. J., Veverka, J., Sagan, C., and Church, C. 1976*b*, report prepared for *Viking* Project use, June.
Elliot, J. L., and Veverka, J. 1976, *Icarus*, 27, 359.
Elliot, J. L., Veverka, J., and Goguen, J. 1975, *Icarus*, 26, 387.
Elliot, J. L., Wasserman, L. H., Veverka, J., Sagan, Carl, and Liller, W. 1974, *Ap. J.*, 190, 719.
French, R. G. 1977, Ph.D. thesis, Cornell University.
French, R. G., Elliot, J. L., and Gierasch, P. J. 1977, *Icarus*, in press.
Hubbard, W. B., Nather, R. E., Evans, D. S., Tull, R. G., Wells, D. C., Van Citters, G. W., Warner, B., and Vanden Bout, P. 1972, *A.J.*, 77, 41.
Hunten, D. M., and Veverka, J. 1976, in *Jupiter*, ed. T. Gehrels (Tucson: University of Arizona Press), p. 247.
Jokipii, J. R., and Hubbard, W. B. 1977, *Icarus*, 30, 537.
Kovalevsky, J., and Link, F. 1969, *Astr. Ap.*, 2, 398.
Mutch, T. A., *et al.* 1976*a*, *Science*, 193, 791.
———. 1976*b*, *Science*, 194, 87.

Mutch, T. A., *et al.* 1976c, *Science*, **194**, 1277.
Nier, A. O., Hanson, W. B., Seiff, A., McElroy, M. B., Spencer, N. W., Duckett, R. J., Knight, T. C. D., and Cook, W. S. 1976, *Science*, **193**, 786.
Old, J. G., Gentili, K. L., and Peck, E. R. 1971, *Opt. Soc. Am.*, **61**, 89.
Owen, G. T., and Biemann, K. 1976, *Science*, **193**, 801.
Peck, E. R., and Fisher, D. J. 1964, *J. Opt. Soc. Am.*, **54**, 1362.
Pollack, J. B. 1976, private communication.
Taylor, G. E. 1976*a*, personal communication.
Taylor, G. E. 1976*b*, *Nature*, **264**, 160.
Texas-Arizona Occultation Group. 1977, *Ap. J.*, **214**, 934.
Wasserman, L. H., Millis, R. L., and Williamon, R. M. 1977, *A.J.*, in press.
Wasserman, L. H., and Veverka, J. 1973, *Icarus*, **20**, 322.
Young, A. T. 1974, in *Methods of Experimental Physics: Astrophysics*, ed. N. Carleton (New York: Academic Press), p. 95.
———. 1976, *Icarus*, **21**, 335.
Young, L. D. G. 1969, *Icarus*, **11**, 386.

C. CHURCH, E. DUNHAM, J. L. ELLIOT, R. G. FRENCH, P. J. GIERASCH, CARL SAGAN, and J. VEVERKA: Laboratory for Planetary Studies, Cornell University, Center for Radiophysics and Space Research, Ithaca, NY 14853

PRECEDING PAGE BLANK NOT FILMED

APPENDIX 2

Analysis of Stellar Occultation Data (1978). Icarus 33, 186-202.

Uranus Occults SAO 158687 (1977). Nature 265, 609-611.

ICARUS 33, 186–202 (1978)

Analysis of Stellar Occultation Data

Effects of Photon Noise and Initial Conditions

R. G. FRENCH, J. L. ELLIOT, AND P. J. GIERASCH

Laboratory for Planetary Studies, Center for Radiophysics and Space Research, Cornell University, Ithaca, New York 14853

Received December 23, 1976; revised June 7, 1977

A new inversion technique for obtaining temperature, pressure, and number density profiles of a planetary atmosphere from an occultation light curve is described. This technique employs an improved boundary condition to begin the numerical inversion and permits the computation of errors in the profiles caused by photon noise in the light curve. We present our assumptions about the atmosphere, optics, and noise and develop the equations for temperature, pressure, and number density and their associated errors. By inverting in equal increments of altitude, Δh, rather than in equal increments of time, Δt, the inversion need not be halted at the first negative point on the light curve as required by previous methods. The importance of the boundary condition is stressed, and a new initial condition is given. Numerical results are presented for the special case of inversion of a noisy isothermal light curve. From these results, simple relations are developed which can be used to predict the noise quality of an occultation. It is found that fractional errors in temperature profiles are comparable to those of pressure and number density profiles. An example of the inversion method is shown. Finally, we discuss the validity of our assumptions. In an appendix we demonstrate that minimum fractional errors in scale height determined from the inversion are comparable to those from an isothermal fit to a noisy isothermal light curve.

I. INTRODUCTION

Observations of stellar occultations by planets have been used to obtain temperature and number density profiles of the occulting planet's atmosphere, through the numerical inversion of the light curve (Kovalevsky and Link, 1969; Hubbard *et al.*, 1972; Vapillon *et al.*, 1973; Veverka *et al.*, 1974). An objection to this technique for reducing occultation data is that there has been no way of associating quantitative uncertainties with the results of the inversion. The uncertainties are of two types. First, the assumptions concerning the planetary atmosphere necessary to do the inversion calculation may not be valid (Young, 1976; Elliot and Veverka, 1976; Jokipii and Hubbard, 1977). Second, the photometric errors affecting the light curve—photon noise, terrestrial scintillation, and baseline uncertainties, for example —must necessarily propagate into the temperature and number density profiles, but these effects have not been evaluated with any generality (Hubbard *et al.*, 1972; Wasserman and Veverka, 1973; Hunten and Veverka, 1976).

In this paper we present a method for calculating the errors due to photon noise in the temperature, pressure, and number density profiles, making the usual assumptions necessary for the inversion of an occultation light curve. To accomplish this task we have recast the inversion equa-

0019-1035/78/0331-0186$02.00/0

tions into a simplified form, more appropriate for treating photon noise. Our analysis explicitly demonstrates the importance of the initial condition used for the inversion calculation, long recognized as critically influencing a large portion of the profiles. We describe a new procedure for establishing this initial condition and evaluating the uncertainty that it produces.

Assuming the basic validity of the inversion method, our final prescription for obtaining number density, pressure and temperature profiles, and their errors is directly applicable to light curves whose dominant photometric error is photon noise—such as the airborne observations of the ε Gem occultation (Elliot *et al.*, 1977b). For this class of light curves, the formulas developed here can be used to estimate, in advance of the occultation, the errors to be expected in temperature, pressure, and number density. For light curves containing significant amounts of other photometric noise, the errors calculated on the basis of our photon noise model are lower limits for the actual errors.

II. A NEW METHOD FOR INVERSION OF LIGHT CURVES

A. Notation and Assumptions

The occultation geometry for an immersion event is illustrated in Fig. 1. Starlight, incident from the left side of the figure, is refracted by a planetary atmosphere and received by a telescope a distance D from a spherical planet of radius R_p. As seen by the telescope, the apparent velocity of the occulted star perpendicular to the limb of the planet is $v_\perp$, and the starlight varies in intensity due to the process of differential refraction. A light ray whose unrefracted path makes the closest approach h to the center of the planet is refracted through an angle $\theta(h)$, which has a negative algebraic sign for the angles indicated in the figure. The x-axis lies parallel to the original direction of the light rays and coordinate r is the distance from the center of the planet. The atmosphere has a refractivity $\nu(r)$, the index of refraction minus unity. The shell notation of the figure will be defined later, when it is used for computations.

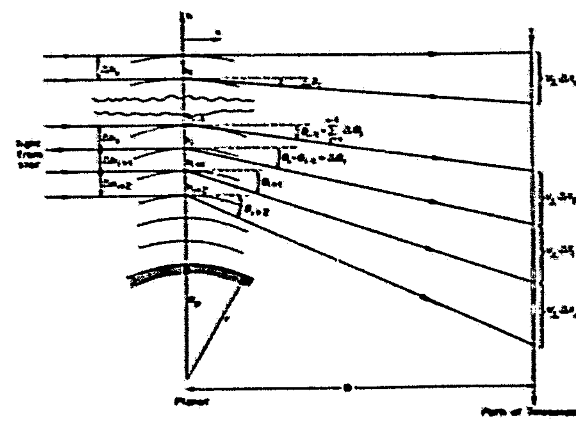

FIG. 1. Occultation geometry for an immersion event. Starlight is incident from the left and is received by a telescope a distance D from a spherical planet of radius R_p. As seen by the telescope, the starlight varies in intensity due to the process of differential refraction. Refer to the text for a complete description of notation.

To obtain the number density, pressure and temperature profiles of the planetary atmosphere from the occultation light curve, we make the following assumptions:

Atmosphere

(i) The approximate scale height H of the atmosphere satisfies the condition $H \ll R_p$.

(ii) The refractivity of the atmosphere $\nu(r)$ is a function of r only.

(iii) The atmosphere has uniform composition.

(iv) The atmosphere is in hydrostatic equilibrium.

(v) Rayleigh scattering and other forms of extinction are negligible when compared to the decrease in intensity due to differential refraction. This will be true if the distance D is large (Baum and Code, 1953).

Optics

(vi) The occulted star is a point source.

(vii) Diffraction effects are negligible (i.e., the ray optics approximation is used).

(viii) There is no ray-crossing (i.e., $d\theta(h)/dh < -1/D$; see Section V of Elliot and Veverka, 1976).

(ix) Bending angles are small (i.e., $|\theta| \ll 1$).

Noise

(x) The light curve received by the telescope contains photon noise.

B. Fundamental Equations

If $H/R_p \ll 1$, it can be shown that (Wasserman and Veverka, 1973)

$$\nu(h) = \frac{2}{\pi(2R_p)^{1/2}} \int_h^\infty (h' - h)^{1/2} d\theta(h'). \quad (1)$$

Then the number density $n(h)$ (cm^{-3}) is given by

$$n(h) = \mathfrak{L}\nu(h)/\nu_{STP}, \quad (2)$$

where $\mathfrak{L}$ is Loschmidt's number and ν_{STP} is the refractivity of the atmosphere at standard temperature and pressure for the wavelength of the observation. The pressure $p(h)$, can be found by integrating the equation of hydrostatic equilibrium

$$dp(h) = -\bar{\mu} g n(h) dh/N_A, \quad (3)$$

where $\bar{\mu}$ is the mean molecular weight of the atmosphere and N_A is Avogadro's number. The gravitational acceleration g is assumed to be constant, but an altitude dependence could be included here if necessary. Integration of (3) yields

$$p(h) = \frac{4g\bar{\mu}\mathfrak{L}}{3\pi(2R_p)^{1/2}\nu_{STP}N_A} \times \int_h^\infty (h' - h)^{3/2} d\theta(h'). \quad (4)$$

Finally, the temperature $T(h)$ can be determined by combining (2), (4) and the perfect gas law:

$$T(h) = N_A p(h)/Rn(h), \quad (5)$$

where R is the universal gas constant.

The scale height $H(h) = RT(h)/\bar{\mu}g$ can be found from (5):

$$H(h) = \frac{2}{3} \int_h^\infty (h' - h)^{3/2} d\theta(h') \Big/ \int_h^\infty (h' - h)^{1/2} d\theta(h'). \quad (6)$$

We note that $H(h)$ is independent of the atmospheric composition. Since the scale height is the ratio of two differently weighted integrals of the same variable, much of the noise cancels out, and we shall find in Section III that a consequence of this is that temperature profiles can have smaller fractional errors than number density and pressure profiles.

To evaluate the integrals in (6), we will write them as summations. In Fig. 1 we have divided the atmosphere into shells of thickness Δh. For the ith shell we define the following quantities: h_i and h_{i-1}, the altitude of its lower and upper boundaries; $\Delta\theta(h_i)$, the increment in refraction angle for the $(i-1)$th and ith rays; Δt_i, the amount of time between the receipt of the $(i-1)$th and ith rays by the telescope; and ϕ_i, the average of the normalized stellar flux received by the telescope during the time interval Δt_i.

The function $\Delta\theta(h_i)$ can be found from the light curve flux $\phi(t)$ by a two-step process. Starting at a reference level h_{i-1}, we can find an implicit equation for the time Δt_i,

$$\Delta h = |h_i - h_{i-1}| = v_\perp \int_{t_{i-1}}^{t_{i-1}+\Delta t_i} \phi(t) dt. \quad (7)$$

After finding Δt_i from (7), we can now find the desired increment in refraction angle $\Delta\theta(h_i)$:

$$\Delta\theta(h_i) = \Delta h - v_\perp \Delta t_i / D \quad (8a)$$

$$= \left(\frac{-v_\perp}{D}\right) \int_{t_{i-1}}^{t_{i-1}+\Delta t_i} [1 - \phi(t)] dt. \quad (8b)$$

C. Errors Caused by Photon Noise

The noise-free occultation flux $\phi(t)$ is not directly obtained from the observations, since photon noise (shot noise) is present in the light curve. Let the quantity $\epsilon^2(\phi)$ be the variance of the shot noise integrated for one second, computed from the Poisson statistics obeyed by photons. For a one second interval when $\phi(t)$ has a constant value ϕ, the average number of detected photons will be $\phi n_* + n_b$, where n_* and n_b are the rates of photons detected per second from the unocculted star and the background. (It is convenient to use units of seconds because the time scale for an occultation is $H/v_\perp$, which is typically of order one second.) For Poisson statistics the variance is equal to the mean, and after normalizing by n_*,

$$\epsilon(\phi) = (\phi n_* + n_b)^{1/2}/n_*. \quad (9)$$

The value of $\epsilon(\phi)$ for two limiting cases will be of interest later:

$$\epsilon(\phi) = (\phi/n_*)^{1/2} \quad \text{for } n_b = 0, \quad (10)$$

$$\epsilon(\phi) = n_b^{1/2}/n_* \quad \text{for } n_b \gg n_*. \quad (11)$$

Finally, the variance in the flux from the ith shell is given by

$$\sigma^2(\phi_i) = v_\perp \phi_i \epsilon^2(\phi_i)/\Delta h. \quad (12)$$

This equation is the fundamental relation for propagating errors from the light curve into number density, pressure, and temperature profiles. In this formulation, the fluxes $\{\phi_i\}$ are taken to be a set of independent random variables. All times $\{\Delta t_i\}$, defined by $\Delta h_i = v_\perp \phi_i \Delta t_i$, are taken to be known exactly, but there is an uncertainty in the location of the shell boundaries which correspond to known times on the light curve.

D. An Improved Initial Condition

There are two kinds of initial errors in the evaluation of the integrals in (1) and (4). First, there is truncation error, since in practice the limits of the integral must be finite. Second, the bending angle is so small at the onset of the occultation that noise fluctuations will completely dominate intensity variations due to the atmosphere. The first requires that the numerical inversion begin early enough to include all true variation, while the second indicates that starting too early will introduce additional errors. The problem we are left with can be stated as follows: Can we find an initial condition which utilizes all of the data in the light curve and which allows an accurate estimate of the errors due to random noise?

In previous work, three approaches have been used. The first is to begin the summation at some value for which $\phi_i \simeq 1$ and $\Delta\theta = 0$ (Wasserman and Veverka, 1973). The difficulty with this method is that an unnecessarily large error is introduced into the computation if the inversion is begun too soon, and information is lost if the in-

ORIGINAL PAGE IS
OF POOR QUALITY

version is begun too late. Additionally, as is shown in Section V, the results are sensitive to the starting point used. A second method has been to generate a sequence of $\Delta\theta_i$'s for the initial part of the light curve by assuming that the atmosphere is isothermal with the scale height determined from a least squares fit to the refractivity profile (Hubbard *et al.*, 1972). These $\Delta\theta_i$'s are then used to start the inversion until the flux has fallen to ~0.98. The objection to this approach has been that small uncertainties in the flux of the first point used in the inversion lead to large errors in estimated $\Delta\theta_i$. A final method has been to specify an initial temperature at an arbitrary altitude (Vapillon *et al.*, 1973).

We have developed an initial condition which utilizes an isothermal fit to the initial part of the light curve only. The procedure has the following features: (a) truncation errors are eliminated; (b) information further down on the light curve does not bias the initial isothermal fit; (c) the fit utilizes uncorrelated random variables whose errors can be determined directly; and (d) the arbitrary features of the other methods are avoided. The method assumes that the upper and lower baselines ($\phi = 1$ and 0 levels) have already been determined by some means.[1] First, $d\theta(h)/dh$ is determined from the data, using (7) and (8), between $h = h_{max}$ and $h = h_0$. The altitude h_{max} corresponds to some point on the light curve which precedes the onset of the occultation, and h_0 corresponds to a point on the light curve where the flux has clearly diminished. The procedure used to determine h_0 is described below.

The function

$$\frac{d\theta}{dh}(h') = ca^{1/2}e^{-a(h'-h_0)} \qquad (13)$$

is fit to the data in the least-squares sense. The form of (13) is chosen so that a and c are uncorrelated random variables whose errors, $\sigma(a)$ and $\sigma(c)$, can be determined from the fit. The scale height of the initial fit is given by $H_0 = 1/a$, and $c = H_0^{1/2}d\theta(h_0)/dh$. Since the fit is performed on data which are equally spaced in altitude rather than in time, the formal errors in the fit have to be modified to account for the interpolation involved in converting data from the time to the space domain. If data are analyzed at very high time resolution, $\Delta\tau$, so that the condition $v_i\Delta\tau \ll \Delta h$ is satisfied, then many data points in time will be included in each Δh shell, and the effects of interpolation will be negligible. (In any case, we require $\Delta h \ll H$; there must be many shells per scale height in order for the numerical approximations to the integrals to be valid.) On the other hand, practical considerations often require $v_i\Delta\tau > \Delta h$ in order that $\Delta h \ll H$, and in this case it is important to correct the formal errors, $\sigma(a)_{formal}$ and $\sigma(c)_{formal}$. We have derived the following correction factor:

$$\sigma_{true} = \left(\frac{3}{2}\frac{v_i\Delta\tau}{\Delta h}\right)^{1/2}\sigma_{formal}. \qquad (14)$$

In computing this factor, we have assumed that the initial fit is halted before $\phi \ll 1$. We emphasize that this correction is appropriate only if $v_i\Delta\tau > \Delta h$.

Finally, the value of h_0 is chosen so that the fitted scale height H_0 is established with an error comparable to that associated with the inversion of later sections of the light curve. In practice this means experimenting with a range of h_0 and selecting the largest value for which $H_0(h_0)$ has settled down to a slowly varying function. With very noisy data, this point can be far down the light curve. Examples are discussed in Sections III and V.

[1] These can be estimated by fitting the Baum and Code equation to the light curve. Both the inversion scheme and the Baum and Code equation assume that all bending of rays by the planetary atmosphere is in the plane of Fig. 1. However, the lateral focussing effects of a spherical atmosphere can be important. For example, they are responsible for the formation of the central flash, a bright feature midway between immersion and emersion in the occultation of ε Gem by Mars (Elliot *et al.*, 1977b). It can be shown, however, that these effects can be neglected when determining baselines, as long as $H/R_p \ll 1$ (French, 1977). A briefer treatment is presented in Pannekoek (1904).

E. Number Density, Pressure, and Temperature Profiles and Their Associated Errors

We are now in a position to write the full expressions for $n(h)$, $p(h)$ and $H(h)$ and their associated errors. Let

$$I_m(h_i) = \int_{h_0}^{\infty} (h'-h_i)^m ca^{1/2}e^{-a(h'-h_0)}dh' \qquad (15)$$

and

$$\Sigma_m(h_i) = \frac{1}{1+m}(\Delta h)^m \sum_{j=j_{min}+1}^{i} \Delta\theta_j \times[(i-j)^{m+1}-(i-j+1)^{m+1}], \qquad (16)$$

where j_{min} is the index of the shell between $h = h_0$ and $h = h_0 + \Delta h$. In (16), we have preintegrated the factor $(h' - h_i)^m$. Expressed in terms of the set of independent variables $\{\phi_i\}$, (16) can be written as

$$\Sigma_m(h_i) = \frac{1}{D(1+m)} \sum_{j=j_{min}+1}^{i} \left(\frac{1-\phi_j}{\phi_j}\right) \times\left[\left(\sum_{k=j}^{i} v_k\phi_k\Delta t_k\right)^{m+1}-\left(\sum_{k=j+1}^{i} v_k\phi_k\Delta t_k\right)^{m+1}\right]. \qquad (17)$$

The random error associated with $\Sigma_m(h_i)$ is

$$\sigma^2[\Sigma_m(h_i)] = \sum_{j=j_{min}+1}^{i} \left[\frac{\partial\Sigma_m(h_i)}{\partial\phi_j}\right]^2\sigma^2(\phi_j) \qquad (18)$$

and the variance of $I_m(h_i)$ is

$$\sigma^2[I_m(h_i)] = [\partial I_m(h_i)/\partial a]^2\sigma^2(a) + [\partial I_m(h_i)/\partial c]^2\sigma^2(c). \qquad (19)$$

The number density in the ith shell is given by

$$n(h_i) = \frac{2\mathcal{L}}{\pi(2R_p)^{1/2}\nu_{STP}} \times [I_{1/2}(h_i) + \Sigma_{1/2}(h_i)]. \qquad (20)$$

The fractional error in $n(h_i)$ is

$$\frac{\sigma[n(h_i)]}{n(h_i)} = \frac{\{\sigma^2[I_{1/2}(h_i)] + \sigma^2[\Sigma_{1/2}(h_i)]\}^{1/2}}{I_{1/2}(h_i) + \Sigma_{1/2}(h_i)}. \qquad (21)$$

Similarly,

$$p(h_i) = \frac{4g\bar{\mu}\mathcal{L}}{3\pi(2R_p)^{1/2}\nu_{STP}N_A} \times [I_{3/2}(h_i) + \Sigma_{3/2}(h_i)], \qquad (22)$$

$$\frac{\sigma[p(h_i)]}{p(h_i)} = \frac{\{\sigma^2[I_{3/2}(h_i)] + \sigma^2[\Sigma_{3/2}(h_i)]\}^{1/2}}{I_{3/2}(h_i) + \Sigma_{3/2}(h_i)}, \qquad (23)$$

$$H(h_i) = \frac{2[I_{3/2}(h_i) + \Sigma_{3/2}(h_i)]}{3[I_{1/2}(h_i) + \Sigma_{1/2}(h_i)]}, \qquad (24)$$

$$\sigma^2[H(h_i)] = \left(\frac{\partial H}{\partial a}(h_i)\right)^2\sigma^2(a) + \left(\frac{\partial H}{\partial c}(h_i)\right)^2\sigma^2(c) + \sum_{j=j_{min}+1}^{i}\left(\frac{\partial H(h_i)}{\partial(\phi_j)}\right)^2\sigma^2(\phi_j). \qquad (25)$$

Finally the error in the altitude difference $(h_j - h_i)$ is given by

$$\sigma^2(h_j - h_i) = \sum_{k=j+1}^{i} (\Delta h/\phi_k)^2\sigma^2(\phi_k). \qquad (26)$$

The evaluation of these quantities is described in Appendix A.

III. THE NATURE OF THE ERRORS

In order to gain insight into the nature of fractional errors in number density, pressure, and scale height, we have obtained solutions to (21), (23), and (25) for the special case of an isothermal atmosphere with a known noise level. (We stress that these equations are valid for *any* atmosphere which satisfies the assumptions in Section IIA.) Since $\epsilon(\phi)$ is a function of both background and stellar fluxes [Eqn. (9)], we have treated two limiting cases: background flux much greater than stellar flux, $n_b \gg n_*$; and background flux much less than stellar flux throughout the light curve, or, in the limit, $n_b = 0$.

Figure 2 illustrates our results for the case $(v_\perp/H)^{1/2}\epsilon(\phi) = 0.01$, where $\epsilon(\phi)$ is evaluated at $\phi = 1.0$. Fractional errors in number density, pressure, scale height, $\Delta\theta$, and the error in altitude difference $(h_* - h)/H$ (E_n, E_p, E_H, $E_{\Delta\theta}$, and E_h, respectively) are shown as a function of depth in the atmosphere and of normalized flux of the light curve. $E_{\Delta\theta}$ has been computed for the case $(v_\perp/\Delta h)^{1/2}\epsilon(\phi) = 0.01$. Note that, in this figure, the light curve is plotted against depth in the atmosphere, rather than against time. The upper branch of each curve corresponds to the case, $n_b \gg n_*$, and the lower branch to the case, $n_b = 0$.

The fractional errors in Fig. 2 are computed using the results of Appendix A, without utilizing an initial fit to the data and assuming that the inversion was begun five scale heights above half-light. We determined the point h_0 in (15) at which the scale height error in the initial fit is equal to the scale height error, $\sigma[H(h_0)]$ for the case shown. This occurs at $\phi = 0.60$ and $h_0 = 0.41H$, for an isothermal atmosphere. If the initial fit is extended to a deeper level (smaller h_0), the fractional errors will be smaller than those shown in Fig. 2; if h_0 is larger than $0.41H$, the fractional errors in Fig. 2 will be slight underestimates for the first scale height or so below h_0. The choice of h_0 in a practical case is discussed in Section V.

Figure 2 can be best understood by examining the nature of the error in $\Sigma_m(h_i)$. In (16) there is an uncertainty in $\{\Delta\theta_i\}$ and also in $(h_j - h_i)^m$, which has been preintegrated in this equation. From (7), (8), and (12) we find

$$\frac{\sigma(\Delta\theta_i)}{\Delta\theta_i} = \left(\frac{v_\perp\phi_i}{\Delta h}\right)^{1/2} \frac{\epsilon(\phi_i)}{(1-\phi_i)}. \quad (27)$$

Equation (27) illustrates that $\sigma(\Delta\theta)/\Delta\theta$ is largest near $\phi = 1$, when noise causes much more variation in apparent flux than does the slight bending due to the atmosphere. As ϕ approaches zero, so does the fractional error in $\Delta\theta$. This is shown in Fig. 2 as $E_{\Delta\theta}$.

Equation (26) gives

$$\frac{\sigma(h_j - h_i)}{H} = \frac{(v_\perp\Delta h)^{1/2}}{H}\left[\sum_{k=j+1}^{i} \frac{\epsilon^2(\phi_k)}{\phi_k}\right]^{1/2}. \quad (28)$$

This is shown in Fig. 2 as E_h, with h_j taken as $5H$. For constant $\epsilon(\phi)$, E_h increases rapidly as $\phi \to 0$, and this is reflected in the corresponding increase in E_n, E_p, and E_H. For $n_b = 0$, $\epsilon(\phi)$ is proportional to $\phi^{1/2}$ [see Eq. (10)], and as $\phi \to 0$, E_n, E_p, and E_H approach constant limiting values.

From the form of (1), (4), and (6), it is evident that the deduced values of $n(h)$, $p(h)$, and $H(h)$ depend on the nature of the entire light curve prior to that point. This reflects the simple fact that a grazing ray at altitude h is refracted not only by the atmosphere at h, but also by the atmosphere along the rest of its path. We can see the manner in which the prior data are weighted by plotting the integrands $\mathcal{I}$ (15) with $m = \frac{3}{2}$ and $m = \frac{1}{2}$, for the case of an isothermal atmosphere. These are used in determining $p(h)$ and $n(h)$, whose ratio is proportional to the scale height. The integrands are shown in Fig. 3, where the curves have been normalized to unity at their maxima, and where altitude, z, is measured in scale heights above h. The main contribution to the integral for $n(h)$

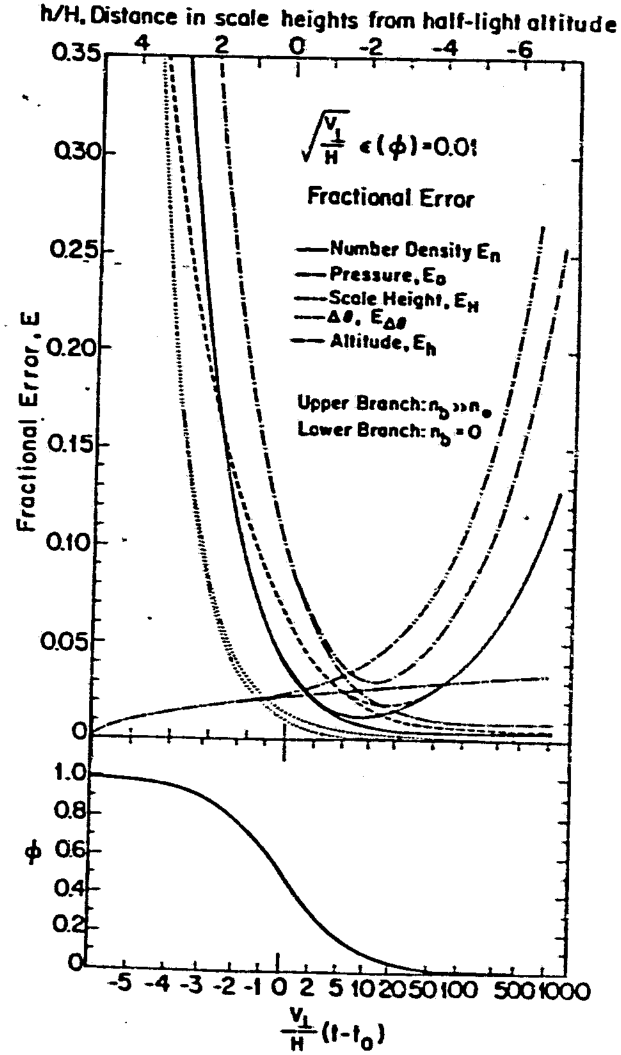

FIG. 2. Fractional errors in $n(h)$, $p(h)$, $H(h)$, $\Delta\theta(h)$, and altitude $(h_* - h)/H$, computed for an isothermal atmosphere. E_n, E_p, E_H, and E_h were determined for the case $(v_\perp/H)^{1/2}\epsilon(\phi) = 0.01$, and $h_* = 5H$, and $E_{\Delta\theta}$ for the case $(v_\perp/\Delta h)^{1/2}\epsilon(\phi) = 0.01$, where $\epsilon(\phi)$ is evaluated at $\phi = 1$. The upper branches correspond to the limit of background flux much greater than stellar flux, $n_b \gg n_*$, and the lower branches to the case, $n_b = 0$. The light curve, below, allows fractional errors at different altitudes to be related to normalized flux, ϕ, and time from half-light, t, along the light curve.

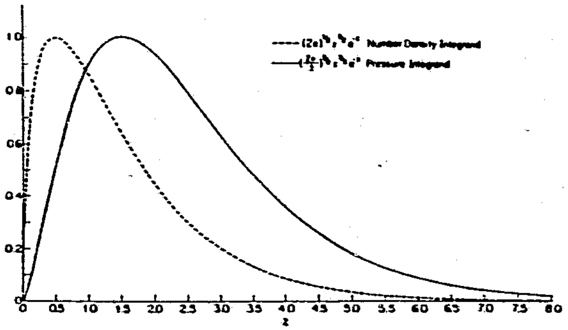

FIG. 3. Integrands used in the computation of $n(h)$ and $p(h)$, for an isothermal atmosphere. The abscissa, z, is the altitude in the atmosphere (measured in scale heights) above the altitude h at which number density and pressure are to be computed. The curves, normalized to unity at their maxima, show how the computed values of $n(h)$ and $p(h)$ depend upon a knowledge of the atmospheric structure for several scale heights above h. In computing $n(h)$, the most significant contribution comes from an altitude range, h to $h + 2.5H$, while for $p(h)$, the main contribution comes from an altitude range $h + 0.5H$ to $h + 4.5H$. This strong weighting of prior data is responsible for the characteristics of the fractional errors, shown in Fig. 2.

comes from a fairly narrow altitude range centered at about $h + 0.5H$, while the main contribution to the integral for $p(h)$ is centered at $h + 1.5H$, with significant contribution from as high as $h + 4.5H$. In other words, the data used to determine $n(h)$ are, in a sense, more "local" than those for $p(h)$.

The fractional errors in $n(h)$ and $p(h)$ are determined from similar weighted averages of the errors in $(h_j - h_i)^m$ and $\Delta\theta$ of prior data. As the inversion proceeds, E_n decreases rapidly because it weights a fairly narrow range of prior data whose fractional errors in $\Delta\theta$ are decreasing rapidly; E_p minimizes somewhat later because it weights most strongly a range of prior data at higher altitude, whose fractional errors in $\Delta\theta$ are still large. In this region the error in $(h_j - h_i)^m$ does not contribute strongly. If $n_b = 0$, the fractional errors E_n, E_p, and E_H will decrease as the inversion is continued, because $E_{\Delta\theta} \to 0$ and E_h is rising only slowly. If $n_b \gg n_*$, E_p rises from its minimum rapidly, in response to the rapid rise in E_h; E_n and E_H rise more slowly because of their weaker dependence on errors in $(h_j - h_i)$.

It is important to note that E_H is comparable to E_n and E_p; as long as all of the assumptions of the method are satisfied, temperature profiles are as accurate as number density and pressure profiles. Additionally, the flux level corresponding to minimum errors is low, due to the weighting functions of Fig. 3. Even for the case $n_b \gg n_*$, the fractional error in H does not rise to double its minimum value until $\phi = 0.001$, $h/H = -4.6$, and $v_\perp(t - t_0)H = 103$. The lesson is that inversions may be continued to deeper levels than previously suspected before errors due to photon noise become large. Inverting in shells of Δh rather than Δt is advantageous in this context because the inversion need not be terminated at the first point at which the apparent flux is negative. Ultimately, uncertainty in the lower baseline will be a more important source of error than photon noise.

ORIGINAL PAGE IS
OF POOR QUALITY

IV. THE QUALITY OF AN OCCULTATION: EFFECTS OF SHOT NOISE

It is useful to have a simple way to predict the quality of an occultation from the fundamental quantities $v_\perp$, H, ϕ, and $\epsilon(\phi)$. The calculations of fractional errors for an isothermal atmosphere, described above, can serve as a guide to the magnitude of the minimum errors we can expect. Expected fractional errors can be obtained by scaling the solutions for E_n, E_p, E_H, $E_{\Delta\theta}$, and E_h in Fig. 2 according to the relations

$$\left.\begin{array}{c}\dfrac{\sigma[n(h)]}{n(h)}\\[2ex] \dfrac{\sigma[p(h)]}{p(h)}\\[2ex] \dfrac{\sigma[H(h)]}{H(h)}\\[2ex] \dfrac{\sigma(5H-h)}{H}\end{array}\right\} = \frac{\epsilon(1.0)}{0.01}\left(\frac{v_\perp}{H}\right)^{1/2}\left\{\begin{array}{ll}E_n(h), & (29)\\[2ex] E_p(h), & (30)\\[2ex] E_H(h), & (31)\\[2ex] E_h(h), & (32)\end{array}\right.$$

$$\frac{\sigma(\Delta\theta)(h)}{\Delta\theta(h)} = \frac{\epsilon(1.0)}{0.01}\left(\frac{v_\perp}{\Delta h}\right)^{1/2} E_{\Delta\theta}(h). \tag{33}$$

For the case $n_b \gg n_*$, the upper branch solutions in Fig. 2 should be used. If $n_b = 0$, the lower branch solutions are appropriate. In (29)–(33), $\epsilon(\phi)$ has been evaluated at $\phi = 1.0$.

Expected minimum fractional errors and the flux levels at which they occur are:

$n_b \gg n_*$:

$$\left.\begin{array}{c}\dfrac{\sigma[n(h)]}{n(h)}\Big|_{\min}\\[2ex] \dfrac{\sigma[p(h)]}{p(h)}\Big|_{\min}\\[2ex] \dfrac{\sigma[H(h)]}{H(h)}\Big|_{\min}\end{array}\right\} = \left(\frac{v_\perp}{H}\right)^{1/2}\epsilon(1.0)\left\{\begin{array}{ll}1.21\ (\phi = 0.13), & (34)\\[2ex] 3.05\ (\phi = 0.09), & (35)\\[2ex] 1.96\ (\phi = 0.07), & (36)\end{array}\right.$$

$n_b = 0$:

$$\left.\begin{array}{c}\dfrac{\sigma[n(h)]}{n(h)}\Big|_{\min}\\[2ex] \dfrac{\sigma[p(h)]}{p(h)}\Big|_{\min}\\[2ex] \dfrac{\sigma[H(h)]}{H(h)}\Big|_{\min}\end{array}\right\} = \left(\frac{v_\perp}{H}\right)^{1/2}\epsilon(1.0)\left\{\begin{array}{ll}\le 0.42 & (37)\\[2ex] \le 0.93, & (38)\\[2ex] \le 0.56. & (39)\end{array}\right.$$

TABLE I

PHOTON NOISE ERRORS FOR OCCULTATIONS

Occultation	$(v_\perp/H)^{1/2}\epsilon(\phi)$[a]	$\sigma(H)/H\rfloor_{min}$	Comments
β Scorpii by Jupiter[b]	0.0004	0.0007	Other noise sources definitely more important than shot noise in determining minimum errors
ϵ Geminorum by Mars[c]	0.012	0.023	Errors due to photon noise consistent with mutual agreement of temperature profiles
SAO 158687 by Uranus[d]	0.003	0.006	

[a] Evaluated for $\phi = \frac{1}{2}$.
[b] 154-cm telescope, $\lambda_0 = 3530$ Å, $\Delta\lambda = 400$ Å (Veverka *et al.*, 1974).
[c] 91-cm telescope, $\lambda_0 = 4500$ Å, $\Delta\lambda = 100$ Å (Elliot *et al.*, 1977b).
[d] 91-cm telescope, $\lambda_0 = 8000$ Å, $\Delta\lambda = 300$ Å (Elliot *et al.*, 1977a).

In (37)–(39), the inequality signs indicate that, for $n_b = 0$, the fractional errors had not reached their limiting values before $\phi = 0.001$, the point at which calculations were stopped. This is evident in Fig. 2.

As an example of the use of these equations, we have estimated the minimum fractional errors in scale height due to shot noise for several occultations. The results are given in Table I. It should be recognized that $\epsilon(\phi)$ is not an intrinsic property of a particular occultation, and its value will depend on how the occultation is observed. For example, the telescope aperture and filter bandwidth are important factors.

V. APPLICATION OF THE INVERSION METHOD: AN EXAMPLE

To illustrate several important features of the new inversion method, we have utilized the equations developed in Section II to invert an isothermal light curve with added random noise. For this case we let $H = 10$ km, $v_\perp = 10$ km sec^{-1}, $\epsilon(\phi) = 0.02$, and $\Delta h = 1$ km. These parameters give a noise factor of $(v_\perp/H)^{1/2}\epsilon(\phi) = 0.02$, comparable to that of the airborne observations of the occultation of ϵ Gem by Mars. We assumed that $n_b \gg n_*$, so that $\epsilon(\phi)$ can be regarded as constant throughout the occultation [see Eq. (11)]. The light curve is shown in Fig. 4. The solid line is a noise-free isothermal light curve computed from the well-known equation of Baum and Code (1953).

Two methods of numerical inversion were used to deduce the scale height. The first utilizes the full theory developed above, together with the new initial condition, an isothermal fit to the initial data in the light curve. The second method does not utilize the new initial condition, and in effect assumes that $H = 0$ at the onset of the inversion.

Figure 5 presents the results of the inversions. For the case shown on the left, an isothermal fit to the initial data, using (13), gave $H_* = 10.88$ km $\pm$ 1.59. The region of the light curve used in the fit is shown in Fig. 4, and begins six scale heights above half-light, and ends at $\phi \approx 0.60$. The error bars on the temperature profile were computed from (25), and have a total length of two standard deviations. At all altitudes, the error bars are consistent with the actual scale height of 10 km. Errors in altitude are not shown, but they can be estimated from Fig. 2. The characteristics of E_H in Fig. 2 are reflected in the errors of the temperature profile: the errors are initially very large, and eventually minimize at about three scale heights below the half-light level, after which they rise slowly. An additional 56 sec of data would have had to be included in the inversion before the deduced temperature profile

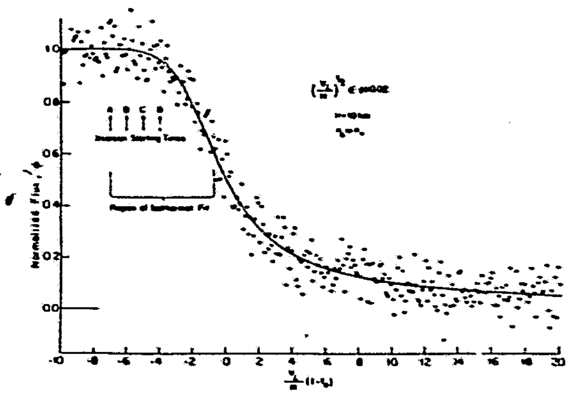

FIG. 4. Isothermal light curve with scale height $H = 10$ km and noise figure $(v_\perp/H)^{1/2}\epsilon(\phi) = 0.02$; it is assumed that $n_b \gg n_*$. The solid line is the noise-free light curve. The results of inversion of the noisy light curve are shown in Fig. 5. The inversion was terminated at $v_\perp(t - t_0)/H = 35.0$, although the curve is shown above only to $v_\perp(t - t_0)/H = 20.0$.

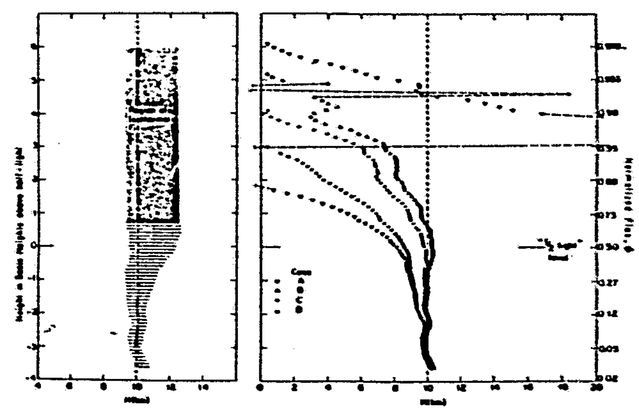

FIG. 5. Scale height profiles obtained from inversion of the light curve shown in Fig. 4. The true scale height is 10 km. The profile at the left was obtained using the new method described in this paper. The error bars are consistent with the true scale height. Errors in altitude are not shown, but the one standard deviation values are about ± 0.5 km at the half-light altitude and ± 1.5 km at the lower end of profile. On the right, profiles were obtained by assuming $H = 0$ at the onset of the inversion. The inversion starting times used for Cases A, B, C, and D are shown in Fig. 4, along with the region of the light curve used in the initial fit.

could be extended a scale height deeper in the atmosphere. At that depth, for the parameters of this example, it can be seen from Fig. 2 that $\sigma(H)/H$ would have increased only to 0.075.

It is important to recognize that the noise in successive points is correlated. For this reason, adjacent points agree better than implied by the error bars. In other words, the error bars refer to the gross positioning of the profile, rather than to the much smaller uncertainties in local temperature variations.

On the right of Fig. 5, we show the results of inversion of the same light curve, but without utilizing an isothermal fit to the initial data. The inversions were begun at four different starting times, corresponding to six, five, four, and three scale heights above half-light; see Fig. 4 for the corresponding positions on the light curve. Case A, the inversion utilizing the most data, converges most slowly to the correct scale height, H, illustrating that errors tend to diverge as the inversion is begun earlier and earlier. Cases B and C give results comparable to the inversion utilizing the initial fit. Case D illustrates the problem of beginning the inversion too late. Although the flux has dropped only to $\phi = 0.95$ at the onset of the inversion, the temperature profile does not converge to within 10% of the actual scale height until $\phi = 0.30$.

We have obtained four substantially different temperature profiles from the same initial data, by changing only the starting point of the inversion and assuming that $H = 0$ initially. Lacking *a priori* knowledge of the true temperature profile, there would be no clear best choice among the curves. In contrast, the new inversion method is less sensitive to the starting time, does not assume a zero temperature at the onset of inversion, and provides a quantitative measure of the error at all altitudes due to a known source of noise.

An important consideration in the use of the new method is the choice of how much of the light curve should be included in the initial isothermal fit. In the parlance of (15), what governs the choice of h_s? If only the first part of the curve is used, (27) shows that the data are noise dominated, and the errors in the fit [$\sigma(a)$ and $\sigma(c)$] will be enormous; they will propagate down through the entire light curve, as seen in (25). On the other hand, if too much of the light curve is used in the initial fit, information about detailed temperature variation will be masked. Additionally, errors in a and c may actually grow as more data are fit, because the assumption that the atmosphere is isothermal may become less realistic. The method may be unreliable if the isothermal approximation is strongly violated.

Although we have found that, for an isothermal atmosphere, it is optimum to fit to the $\phi = 0.60$ level, this can only serve as a rough guide in actual practice, because there is no guarantee that the sampled atmosphere is isothermal. Our strategy is to fit successively larger sections of the data until the deduced scale height, H_c, is insensitive to changes in h_s which are small compared to H_c. In Table II, we give the results of a variety of fits to the initial data in this example to show the change in H_c as the region of the fit is varied. By this means, the initial fit serves the function of damping the erratic initial behavior of the inversion and of rendering the inversion insensitive to its starting point. It provides an estimate of errors due to photon noise, and by stopping the fit as early as possible, the atmospheric temperature profile can be determined by the inversion over a significant altitude range.

TABLE II

VARIATION OF H_c WITH RANGE OF DATA USED FOR FIT

h_{max}/H	h_s/H	$\phi(h_s)$	H_c (km)[a]
6.0	1.1	0.75	11.98 ± 2.83
	0.6	0.65	10.88 ± 1.59
5.0	2.5	0.92	10.08 ± 8.56
	2.4	0.92	8.52 ± 5.79
4.0	2.0	0.88	7.73 ± 2.93
	1.4	0.80	13.35 ± 4.10
	0.9	0.71	9.67 ± 1.58
	0.3	0.57	12.31 ± 1.51
3.0	1.0	0.73	12.35 ± 2.80
	0.4	0.60	12.71 ± 1.99

[a] True value of scale height = 10 km.

VI. DISCUSSION

We have used the new inversion method to obtain number density, pressure, and temperature profiles of the Martian atmosphere from airborne observations of the occultation of ϵ Gem on 8 April 1976 (Elliot *et al.*, 1977b). Three light curves were obtained simultaneously, each probing the same region of the Martian atmosphere, but each containing a different sample of photon noise. Hence the profiles obtained from different light curves should agree within their error bars—which they do—providing an internal consistency check of our method for computing errors.

Further analysis of the temperature profiles obtained from the ϵ Gem occultation showed that temperature variations, having a vertical scale of order one scale height, are determined much more precisely than the mean temperature, in the presence of photon noise (see Figs. 12 and 13 in Elliot *et al.*, 1977b). The present analysis could be extended to understand quantitatively the reliability of temperature information over various length scales, perhaps by a power spectrum analysis of temperature variations.

Fractional errors in $n(h)$, $p(h)$, and $H(h)$ due to photon noise minimize at very low fluxes, and at this point other sources of uncertainty become important. Baseline instability and uncertainty remain to be studied in detail. Additionally, as the inversion is extended into the noise-dominated tail of a light curve, statistical fluctuations will give solutions Δt_i in (7) even if the flux from the star is zero. This would have the effect of producing a spurious high-temperature tail on the deduced profile. In practice, inversions must be terminated for other reasons before this effect becomes important.

To some extent, each of the assumptions in Section IIA is only approximately satisfied. On the basis of scintillation theory, several authors (Young, 1976; Jokipii and Hubbard, 1977) have concluded that the assumption of spherical symmetry is so strongly violated as to invalidate the inversion method. By comparing the light curves obtained by several observers of the ϵ Gem occultation, it may be possible to place some limits on the degree of spherical symmetry of the Martian atmosphere, and hence to test this important assumption. This work is being pursued.

VII. CONCLUSIONS

With the new method of analysis of occultation light curves described above, we are able to place error bars on temperature, pressure, and number density profiles due to photon noise in the data, given the assumptions stated in Section IIA. An improved initial condition renders the inversion less sensitive to its starting point, and thus is less arbitrary than previous methods. An important result is that temperature profiles are shown to be as reliable as refractivity, number density, and pressure profiles. The manner in which prior data are weighted is responsible for large initial fractional errors in $n(h)$, $p(h)$, and $H(h)$, but also accounts for the fact that errors in these quantities due to photon noise minimize at very low flux levels. Consequently, as long as baselines are stable, the inversion can be extended deep in the atmosphere; by inverting in increments Δh, rather than Δt, the inversion need not be halted when the first negative data point is reached.

We have computed the errors in $n(h)$, $p(h)$, and $H(h)$ for an isothermal light curve with a known level of photon noise. The noise quality of an occultation can be estimated by scaling the isothermal solution to the appropriate value of $(v_\perp/H)^{1/2}\epsilon(\phi)$. Fractional errors due to photon noise are only a few percent when $(v_\perp/H)^{1/2}\epsilon(\phi) \approx 0.01$, a reasonable value for high quality observations. Additionally, we have shown that minimum fractional errors in scale height determined from the inversion are comparable to those from an isothermal fit to a noisy isothermal light curve.

APPENDIX A

We derive here the quantities used to determine $\sigma^2[\Sigma_m(h_i)]$, $\sigma^2[H(h_i)]$, and $\sigma^2[I_m(h_i)]$ given in Section IIE. From (18),

$$\sigma^2[\Sigma_m(h_i)] = \sum_{j=j_{\min}+1}^{i} \left[\frac{\partial \Sigma_m(h_i)}{\partial \phi_j}\right]^2 \sigma^2(\phi_j). \quad \text{(A1)}$$

The variance in ϕ_j, $\sigma^2(\phi_j)$ is given by (12). Let

$$\Gamma_j = \frac{(1-\phi_j)}{(1+m)D\phi_j}\Big[\Big(\sum_{l=j}^{i} v_\perp\phi_l\Delta t_l\Big)^{m+1} - \Big(\sum_{l=j+1}^{i} v_\perp\phi_l\Delta t_l\Big)^{m+1}\Big]. \quad \text{(A2)}$$

Then

$$\Sigma_m(h_i) = \sum_{j=j_{\min}+1}^{i} \Gamma_j \quad \text{(A3)}$$

and

$$\frac{\partial \Sigma_m}{\partial \phi_j} = \frac{\partial \Gamma_j}{\partial \phi_j} + \sum_{k=j_{\min}+1}^{j-1} \frac{\partial \Gamma_k}{\partial \phi_j}. \quad \text{(A4)}$$

From (A2) and the relation $\Delta h = v_\perp\phi_j\Delta t_j$, we find

$$\frac{\partial \Gamma_j}{\partial \phi_j} = \frac{-\Delta h^{m+1}}{D(1+m)\phi_j^2}\big[(1+m)(\phi_j-1)(i-j+1)^m + (i-j+1)^{m+1} - (i-j)^{m+1}\big] \quad \text{(A5)}$$

and

$$\left.\frac{\partial \Gamma_k}{\partial \phi_j}\right|_{k\neq j} = \frac{\Delta h^{m+1}}{D\phi_j\phi_k}(1-\phi_k) \times [(i-k+1)^m - (i-k)^m] \quad \text{(A6)}$$

All of the terms in (A1) are now known.

From (25),

$$\sigma^2[H(h_i)] = \left(\frac{\partial H(h_i)}{\partial a}\right)^2\sigma^2(a) + \left(\frac{\partial H(h_i)}{\partial c}\right)^2\sigma^2(c) + \sum_{j=j_{\min}+1}^{i}\left(\frac{\partial H(h_i)}{\partial \phi_j}\right)^2\sigma^2(\phi_j). \quad \text{(A7)}$$

The variances in a and c are determined from the fit of (13) to the data as modified by (14). The partial derivatives in (A7) are:

$$\frac{\partial H(h_i)}{\partial a} = \frac{\frac{2}{3}\frac{\partial I_{3/2}(h_i)}{\partial a} - H(h_i)\frac{\partial I_{1/2}(h_i)}{\partial a}}{[I_{1/2}(h_i)+\Sigma_{1/2}(h_i)]}, \quad \text{(A8)}$$

$$\frac{\partial H(h_i)}{\partial c} = \frac{\frac{2}{3}\frac{\partial I_{3/2}(h_i)}{\partial c} - H(h_i)\frac{\partial I_{1/2}(h_i)}{\partial c}}{[I_{1/2}(h_i)+\Sigma_{1/2}(h_i)]}, \quad \text{(A9)}$$

$$\frac{\partial H(h_i)}{\partial \phi_j} = \frac{\frac{2}{3}\frac{\partial \Sigma_{3/2}(h_i)}{\partial \phi_j} - H(h_i)\frac{\partial \Sigma_{1/2}(h_i)}{\partial \phi_j}}{[I_{1/2}(h_i)+\Sigma_{1/2}(h_i)]}, \quad \text{(A10)}$$

where the derivatives in Σ_m have been defined in (A4)–(A6). Letting $u = a(h_0 - h_i)$, we find from (15)

$$\partial I_m(h_i)/\partial a = [(u+\tfrac{1}{2})/a]I_m(h_i) - I_{m+1}(h_i), \quad \text{(A11)}$$

$$\partial I_m(h_i)/\partial c = I_m(h_i)/c, \quad \text{(A12)}$$

where

$$I_{1/2}(h) = (c/a)[u^{1/2} + \tfrac{1}{2}\pi^{1/2}e^{u}\,\mathrm{erfc}\,(u^{1/2})], \quad \text{(A13)}$$

$$I_{3/2}(h) = (c/a^2)[u^{1/2}(u+\tfrac{3}{2}) + \tfrac{3}{4}\pi^{1/2}e^{u}\,\mathrm{erfc}\,(u^{1/2})], \quad \text{(A14)}$$

$$I_{5/2}(h) = (c/a^3)\Big[u^{1/2}\Big(u^2 + \frac{5}{2}u + \frac{15}{4}\Big) + \frac{15}{8}(\pi)^{1/2}e^{u}\,\mathrm{erfc}\,(u^{1/2})\Big], \quad \text{(A15)}$$

and

$$\mathrm{erfc}\,(x) = \left(\frac{2}{\pi^{1/2}}\right)\int_x^\infty e^{-t^2}dt. \quad \text{(A16)}$$

The fractional error in H can be computed from (A7).

APPENDIX B

Isothermal curve fitting has often been used to obtain an estimate of the mean scale height of the atmosphere sampled by the light curve. The merits and hazards of this practice have been the subject of considerable debate, and we wish to show only that, for the high background case ($n_b \gg n_s$), the error in an isothermal fit to a noisy isothermal light curve is approximately equivalent to the minimum error given by the inversion method. In other words, even in the most favorable case for an isothermal fit, its error is not significantly smaller than that given by the inversion method.

Assume that the isothermal light curve equation of Baum and Code, Eq. (B1), is being fit to an isothermal light curve with known noise $\epsilon(\phi)$, but unknown scale height, H, and midtime, t_0. We assume that the baselines are known exactly.

$$v_\perp(t-t_0)/H = (1/\phi - 2) + \ln(1/\phi - 1). \quad \text{(B1)}$$

Then the errors in the values of H and t_0 given by the fit can be computed from standard formulas (Clifford, 1973):

$$\sigma(H) = (c_{t_0}/d)^{1/2}, \quad \text{(B2)}$$

$$\sigma(t_0) = (c_H/d)^{1/2}, \quad \text{(B3)}$$

where

$$d = c_H c_{t_0} - c^2_{Ht_0} \quad \text{(B4)}$$

$$c_{t_0} = [1/\epsilon^2(\phi)]\int_{-\infty}^{\infty}(\partial\phi/\partial t_0)^2 dt, \quad \text{(B5)}$$

$$c_H = [1/\epsilon^2(\phi)]\int_{-\infty}^{\infty}(\partial\phi/\partial H)^2 dt, \quad \text{(B6)}$$

$$c_{Ht_0} = [1/\epsilon^2(\phi)]\int_{-\infty}^{\infty}(\partial\phi/\partial H)(\partial\phi/\partial t_0)dt. \quad \text{(B7)}$$

The correlation coefficient for H and t_0 is

$$\rho(H, t_0) = -c_{Ht_0}/(c_H c_{t_0})^{1/2}. \quad \text{(B8)}$$

Evaluating the above expressions after some manipulation, we find

$$c_{t_0} = [v_\perp/\epsilon^2(\phi)H]\int_0^1 \phi^2(1-\phi)d\phi = v_\perp/12H\epsilon^2(\phi), \quad \text{(B9)}$$

$$c_H = [1/v_\perp H\epsilon^2(\phi)]\int_0^1 [(1/\phi - 2) + \ln(1/\phi - 1)]^2\phi^2(1-\phi)d\phi \approx 0.441/v_\perp H\epsilon^2(\phi), \quad \text{(B10)}$$

$$c_{Ht_0} = [1/H\epsilon^2(\phi)]\int_0^1 [(1/\phi - 2) + \ln(1/\phi - 1)]\phi^2(1-\phi)d\phi = -1/24H\epsilon^2(\phi), \quad \text{(B11)}$$

$$d = 0.035/H^2\epsilon^4(\phi). \quad \text{(B12)}$$

From the above quantities, we find the fractional error in scale height obtained from an isothermal fit to the entire light curve to be

$$\sigma(H)/H = 1.54(v_\perp/H)^{1/2}\epsilon(\phi). \quad \text{(B13)}$$

By comparison, the minimum fractional error in scale height given by the inversion method for the same conditions is given from Section IV as

$$\sigma(H)/H|_{\min} = 1.96(v_\perp/H)^{1/2}\epsilon(\phi). \quad \text{(B14)}$$

We conclude that the inversion method has minimum fractional errors comparable to those of an isothermal fit for the case of a noisy isothermal light curve.

The error in the estimate to the midtime, t_0, from the isothermal fit, is

$$\sigma(t_0) = 3.55(H/v_\perp)^{1/2}\epsilon(\phi). \quad \text{(B15)}$$

This gives a fundamental limit to the accuracy of the "half-light" time, a quantity which is useful for occultation astronomy (Taylor, 1976).

Finally, the correlation coefficient has the value $\rho_{Ht_0} = 0.217$. This very low value means that the formal error in t_0 will be nearly the same whether or not H is a free parameter in the fit, and vice versa.

ACKNOWLEDGMENTS

We wish to thank L. H. Wasserman for very helpful discussions concerning an earlier version of this paper, and acknowledge several helpful suggestions from J. T. Jokipii and D. M. Hunten as referees of this paper. Additionally, we are grateful to M. Roth for help in preparing the manuscript and B. Boettcher for drawing the figures. This work was supported in part by NASA Grants NGL 33-010-086, NSG-7126, and NSG-2174. One of us (P.J.G.) acknowledges the support of an Alfred P. Sloan research fellowship.

REFERENCES

Baum, W. A., and Code, A. D. (1953). A photometric observation of the occultation of σ Arietis. *Astron. J.* 58, 108–112.

Clifford, A. A. (1973). *Multivariate Error Analysis.* Applied Science Publishers, Essex, England.

Elliot, J. L., and Veverka, J. (1976). Stellar occultation spikes as probes of atmospheric structure and composition. *Icarus* 27, 359–386.

Elliot, J. L., Veverka, J., and Millis, R. L. (1977a). Uranus occults SAO 158687. *Nature* 265, 609.

Elliot, J. L., French, R. G., Dunham, E., Gierasch, P. J., Veverka, J., Church, C., and Sagan, C. (1977b). Occultation of ε Geminorum by Mars. II. The structure and extinction of the Martian upper atmosphere. *Astrophys. J.* 217, 661–679.

French, R. G. (1977). Ph.D. thesis, Cornell University.

Hubbard, W. B., Nather, R. E., Evans, D. S., Tull, R. G., Wells, D. C., van Citters, G. W., Warner, B., and Vanden Bout, P. (1972). The occultation of β Scorpii by Jupiter and Io. I. Jupiter. *Astron. J.* 77, 41–59.

Hunten, D. M., and Veverka, J. (1976). Stellar and spacecraft occultations by Jupiter: A critical review of derived temperature profiles. In *Jupiter* (T. Gehrels, Ed.), pp. 247–283. University of Arizona Press, Tucson.

Jokipii, J. R., and Hubbard, W. H. (1977). Stellar occultations by turbulent planetary atmospheres: The Beta Scorpii events. *Icarus* 30, 537–550.

Kovalevsky, J., and Link, F. (1969). Diamètre aplatissement et propriétés optiques de la haute atmosphère de Neptune d'après l'occultation de l'étoile BD-17° 4388. *Astron. Astrophys.* 2, 398–412.

Pannekoek, A. (1904). Über die Erscheinungen, welche bei einer Sternbedeckung durch einen Planeten auftreten. *Astron. Nachr.* 164, 5–10.

Taylor, G. E. (1976). Oblateness of the atmosphere of Mars. *Nature* 264, 160–161.

Vapillon, L., Combes, M., and Lecacheux, J. (1973). The β Scorpii occultation by Jupiter. II. The temperature and density profiles of the Jovian upper atmosphere. *Astron. Astrophys.* 29, 135–149.

Veverka, J., Wasserman, L. H., Elliot, J. L., Sagan, C., and Liller, W. (1974). The occultation of β Scorpii by Jupiter. I. The structure of the Jovian upper atmosphere. *Astron. J.* 79, 73–84.

Wasserman, L. H., and Veverka, J. (1973). On the reduction of occultation light curves. *Icarus* 20, 322–345.

Young, A. T. (1976). Scintillations during occultations by planets. *Icarus* 27, 335–358.

Uranus occults SAO158687

On March 10, 1977, Uranus will occult SAO158687, a star of late spectral type with a visual magnitude of ≈ -9.5 (refs 1,2). The occultation will be visible from land areas surrounding the Indian Ocean[1,2]. From high-quality light curves of this event one can obtain temperature, pressure and number density profiles of the uranian atmosphere; information about its composition; and by combining occultation timings from several stations the precise diameter and oblateness of the planet can be found. For the atmospheres of Jupiter[3-6] and Mars[6-9] these quantities have been obtained from recent stellar occultations by these planets. This experience can be used to predict what can be learned from the forthcoming occultation by Uranus.

Although Uranus is several magnitudes brighter than SAO 158687 at visual wavelengths, the strong methane absorption bands in the far red and infrared spectrum of Uranus make the intensity of both objects nearly equal at these wavelengths[8]. To see how to use the methane absorption bands to best advantage, we obtained the spectra of Uranus and SAO 158687 (Fig. 1). These spectra are meant to show the relative instrumental intensities of the two objects and have therefore not been calibrated on an absolute scale. The resolution of the spectra is 10 Å and the cutoff near 9,000 Å is due to a cutoff in

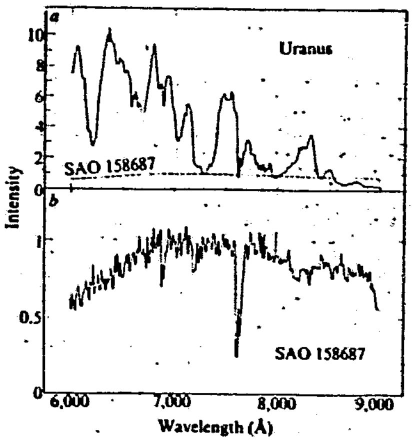

Fig. 1 Relative intensity of Uranus and SAO158687. Each spectrum was obtained with a 10-Å slit; the intensity scales are linear in the instrumental system. *a*, The two spectra on a common scale; *b*, an expanded version of the SAO158687 spectrum. In the deep methane band near 8,600 Å the stellar flux exceeds that of Uranus. The common absorption feature near 7,600 Å is the telluric Fraunhofer A band of molecular oxygen.

the instrumental response. The contribution from the sky background and dark current is negligible.

Table 1 lists four passbands where the relative intensities (integrated over the passband) of SAO158687 and Uranus are most nearly equal. Since the passbands are narrow, the ratio of these intensities is, for practical purposes, equal to the ratio of the photon fluxes f_u/f_*, where f_u and f_* are the photons $cm^{-2}\ s^{-1}\ Å^{-1}$ incident on the Earth's atmosphere from SAO158687 and Uranus, respectively. We have assumed SAO158687 to have UBVRI colours appropriate for a K5 main sequence star[1,8,10] and computed the expected photon fluxes f_* (Table 1).

If observing conditions are good during the occultation, then the signal-noise ratio of the light curves should be limited by photon statistics. The latter give a fundamental limit for the signal-noise ratio achievable. We define $\varphi(t)$ to be the flux from SAO158687 observed during the occultation, normalised to the unocculted intensity of the star. Hence $\varphi(t)$ begins at 1.0 and decreases to 0.0 as the occultation proceeds. If ε_φ is the r.m.s. error in φ due to photon statistics for a 1-s integration, then ε_φ is equal to the square-root of the total photons detected from Uranus and the star, divided by the photons that would have been detected from the unocculted star

$$\varepsilon_\varphi = \frac{(\bar{\varphi}f_* + f_u)^{1/2}}{f_*\sqrt{(q\Delta\lambda A)}} \qquad (1)$$

where $\bar{\varphi}$ is the average value of $\varphi(t)$ during a 1-s interval, A is the area (cm^2) of the telescope, $\Delta\lambda$ the passband of the filter (in Å) and q the fraction of the photons incident on the Earth's atmosphere that are ultimately detected by the photomultiplier. The factor q includes the transmission of the Earth's atmosphere, telescope optics, photometer optics and the quantum efficiency of the photomultiplier. The quantity ε_φ has the dimensions of $s^{1/2}$, the actual r.m.s. error in φ for an arbitrary integration time of Δt is found by dividing ε_φ by $(\Delta t)^{1/2}$. In writing equation (1) we assume that the background counting rates from the photomultiplier itself and the sky are negligible. This may not be entirely true, since a quarter Moon will be only 17° away[4] during the occultation.

Values of ε_φ (Table 1) were computed for $\Delta t = 1$ s, $q = 0.04$, $A = 6.6\times10^3\ cm^2$ (36-inch telescope) and $\bar{\varphi} = 1/3$.

From Table 1 we see that low photon noise errors can be achieved by choosing appropriate passbands for observation. Such low errors could be realised in ideal conditions, but in practice changes in transparency, guiding errors, severe scintillation[10] and other problems could increase the effective noise in the signal above the level of photon noise.

From the photon noise levels in Table 1, we can calculate the r.m.s. error expected for the temperature profiles obtained from the occultation light curves, if we assume that the gravity gradient model[8] applies to the uranian atmosphere. From the improved procedure of French *et al.*[11] for obtaining temperature profiles from occultation light curves, the minimum r.m.s. error in the scale height $\sigma(H)$, expressed as a fraction of the scale height H is

$$\left.\frac{\sigma(H)}{H}\right|_{min} \approx 1.5\left(\frac{v_\perp}{H}\right)^{1/2}\varepsilon_\varphi \qquad (2)$$

where $v_\perp$ is the apparent velocity of SAO158687 perpendicular to the limb of Uranus. The scale height is related to the temperature T by $H = RT/\mu g$, where g is the gravitational acceleration, R the universal gas constant and μ the mean molecular weight of the atmosphere. At the occultation level we expect $T \sim 140$ K (ref. 13), hence $H \sim 65$ km (for $\mu \sim 2$). For this occultation $v_\perp \sim 12\ km\ s^{-1}$ (ref. 2). Even for the largest value of ε_φ in Table 1 (0.04), the fractional error in the scale height is only 2.6% (equation (2)). The minimum error in the temperature then will probably be dominated by uncertainties in the mean molecular weight.

At the occultation level the main constituents are likely to be H_2, He and CH_4. For solar composition the mixing ratio of CH_4 would be $\sim 7\times10^{-4}$ (ref. 13), which would leave H_2 and He as the major constituents. It may be possible to obtain a value for the helium number fraction [He]/[H_2], from light curves at two wavelengths (6,200 and 8,600 Å, for example), as was done for Jupiter[14], and for the [Ar]/[CO_2] fraction in the case of Mars[9]. *A priori*, it is difficult to predict the expected accuracy of this measurement, since the accuracy will depend on the number and intensity of the 'spikes' in the light curves[3].

The level of the atmosphere probed by the occultation corresponds to a number density n given approximately by the number density at 'half-light' for an ideal isothermal atmosphere[15]

$$n = \frac{\mathscr{L}}{\nu_{STP}}\left(\frac{T}{273\ K}\right)\left(\frac{H}{D}\right)\frac{1}{\sqrt{2\pi(R_u/H)}} \approx 6\times10^{15} \qquad (3)$$

where $\mathscr{L}$ is Loschmidt's number, ν_{STP} the refractivity of the atmosphere at STP, D the distance to Uranus and R_u the radius of Uranus.

The 'central flash', observed during the occultation of ε Gem by Mars[16], and used to determine the extinction of the martian atmosphere[9], will probably not be observable, since the centre of the Uranus shadow is predicted to be off the edge of the Earth.

Observers of this occultation should record their data digitally. The shortest timescale of importance for the 'spikes' will be $\sim \delta D/2v_\perp \approx 0.3$ s, where $\delta = 5.8\times10^{-4}$ arc s (ref. 2) is the angular diameter of SAO158687. Higher time resolution data recording would be desirable, but is not essential.

We plan to observe this occultation from Perth and over the Indian Ocean with the 91-cm airborne telescope[16]. Observers of this occultation interested in coordinating the analysis of their results should write to one of us. We acknowledge the support of grants from NASA.

Note added in proof: An updated prediction for this occultation can be found elsewhere[17].

J. L. Elliot
J. Veverka

Laboratory for Planetary Studies,
Cornell University,
Ithaca, New York 14853

R. L. Millis

Planetary Research Center,
Lowell Observatory,
Flagstaff, Arizona 86002

Received October 28, 1976; accepted January 6, 1977.

1 Taylor, G. E. *J. Br. astr. Ass.* 83, 352 (1973).
2 Smith, B. A. in *The Atmosphere of Uranus* (ed. Hunten, D. M.) 162–166 (Proc. Workshop at Ames Res. Center, September 30, 1974).
3 Elliot, J. L. & Veverka, J. *Icarus* 27, 359 (1976).
4 Hunten, D. M. & Veverka, J. in *Jupiter* (ed. Gehrels, T.) 247–283 (University of Arizona Press, Tucson, 1976).
5 Hubbard, W. B. & Van Flandern, T. C. *Astrophys. J.* 77, 65 (1972).
6 Taylor, G. E. *Nature* 264, 160–161 (1976).
7 Wasserman, L. H., Millis, R. L., White, N. M., Williamon, R. M. & McCracken, C. W. (in preparation).
8 Elliot, J. L. *et al. Science* 195, 485–486 (1977).
9 Elliot, J. L. *et al.* (submitted to *Astrophys. J.*).
10 Johnson, H. L., MacArthur, J. W. & Mitchell, R. I. *Astrophys. J.* 152, 465 (1968).
11 French, R. G., Gierasch, P. J. & Elliot, J. L. (submitted to *Icarus*).
12 Young, A. T. *Astrophys. J.* 72, 747 (1967).
13 Wallace, L. *Icarus* 25, 538 (1975).
14 Elliot, J. L., Wasserman, L. H., Veverka, J., Sagan, C. & Liller, W. *Astrophys. J.* 190, 719 (1974).
15 Baum, W. A. & Code, A. D. *Astron. J.* 58, 108 (1953).
16 Elliot, J. L., Dunham, E. & Church, C. *Sky Telescope* 52, 23 (1976).
17 *IAU Circ* (in the press).

Table 1 Photon noise errors for selected passbands

Centre wavelength (Å)	Passband, $\Delta\lambda$ (Å)	Flux ratio, f_u/f_*	Flux† from SAO158687, f_*	r.m.s. photon noise error for a 1-s integration ε_φ
6,200	100	0.14	0.2	0.04
7,300	200	0.5	0.4	0.011
8,000	300	0.7	0.5	0.007
8,600	400	1.2	0.6	0.006

†Photons $cm^{-2}\ s^{-1}\ Å^{-1}$ outside the Earth's atmosphere.

APPENDIX 3

Lunar Occultation of Saturn. II. The Normal Reflectances of Rhea, Titan, and Iapetus (1978). Icarus 35, 237-246.

Lunar Occultation of Saturn. III. How Big Is Iapetus? (1978). Icarus 33, 301-310.

ICARUS 35, 237–246 (1978)

Lunar Occultation of Saturn

II. The Normal Reflectances of Rhea, Titan, and Iapetus[1]

J. L. ELLIOT,[2] E. W. DUNHAM, J. VEVERKA,[2] AND J. GOGUEN[2]

Laboratory for Planetary Studies, Cornell University, Ithaca, New York 14853

Received May 4, 1977; revised January 16, 1978

An inversion procedure to obtain the reflectance of the central region of a satellite's disk from lunar occultation data is presented. The scheme assumes that the limb darkening of the satellite depends only on the radial distance from the center of the disk. Given this assumption, normal reflectances can be derived that are essentially independent of the limb darkening and the diameter of the satellite. The procedure has been applied to our observations of the March 1974 lunar occultation of Tethys, Dione, Rhea, Titan, and Iapetus. In the V passband we derive the following normal reflectances: Rhea (0.97 ± 0.20), Titan (0.24 ± 0.03), Iapetus, bright face (0.60 ± 0.14). For Tethys and Dione the values derived have large uncertainties, but are consistent with our result for Rhea.

I. INTRODUCTION

The 1974 March occultations of Tethys, Dione, Rhea, Titan, and Iapetus were observed simultaneously with the 224 and 61 cm telescopes at Mauna Kea Observatory (Elliot *et al.*, 1975; hereafter Paper I). Lightcurves were obtained in three colors with the 224 cm telescope and in a single broadband channel with the 61 cm telescope. The center wavelengths and passbands of the four channels are given in Table I. For later reference, Fig. 1 shows these filter passbands superimposed on a portion of the spectral reflectance curve of Titan given by McCord *et al.* (1971).

Photon counting systems were used on all four channels, and all light curves were recorded on digital magnetic tape as a series of 10 msec integrations of photon counts. Altogether 19 occultation light curves were obtained. An example of the data is shown in Fig. 2, where the occultation curve for Titan obtained at 7400 Å is shown at the full time resolution of 10 msec. A detailed description of the instrumentation, observations and circumstances of the occultations is given in Paper I. One particularly fortunate circumstance was the position of Iapetus in its orbit, only 3° from western elongation. Hence at the time of the occultation we were getting almost a full view of the bright face of this unique satellite.

In Paper I we fit model light curves to the data and, for each satellite, found solutions constraining the diameter and limb darkening parameter k assuming a Minneart law ($I(\epsilon) = I_0 \cos^{2k-1} \epsilon$) for the limb darkening. Only for Titan was the signal-to-noise ratio great enough to constrain both the diameter and the exponent k. In this paper we introduce a novel method for obtaining the normal reflectance of the satellites from the lunar occultation light curves.

[1] Presented at the 1975 Meeting of the Division of Planetary Sciences, Columbia, Maryland.

[2] Guest Observer, Mauna Kea Observatory.

0019-1035/78/0352-0237$02.00/0

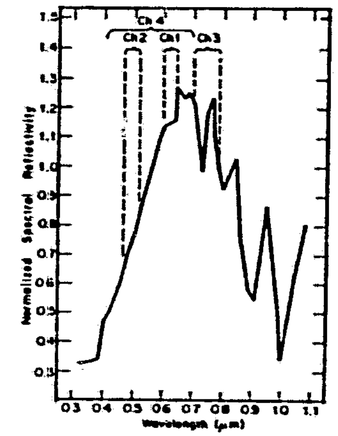

FIG. 1. Normalized spectral reflectivity for Titan (after McCord *et al.*, 1971). Occultation light curves were obtained for each of the four wavelength intervals shown (cf. Table I).

II. METHOD OF ANALYSIS

When a satellite of large angular diameter is occulted by the moon, diffraction effects are not important (Paper I), and the observed light curve will be that of an illuminated disk occulted by a uniformly moving straightedge (Fig. 3). In the schematic light curve shown, the background has been subtracted and the light curve normalized to the unocculted intensity of the satellite. Hence the intensity starts at 1.0 and drops to 0.0 as the occultation proceeds, with midoccultation occurring at time t_0. The lunar limb starts occulting the satellite at time t_1, and during the first time interval Δt the light decreases by an amount $(I_1 - I_2)$. This drop in intensity equals the amount of light reflected from strip number 3 of the satellite (see Fig. 3). The intensity drop $(I_1 - I_2)$ depends on the integral of the brightness distribution within the occulted strip, and we immediately see that a single occulta-

TABLE I

FILTER PASSBANDS

Channel No.	Telescope	Center wavelength (Å)	Passband (FWHM)[a] (Å)
1	224 cm	6200	400
2	224 cm	4900	400
3	224 cm	7400	750
4	61 cm	~5500[b]	3000

[a] Full width at half maximum.

[b] The center wavelength of this filter is ill-defined because of the broad passband.

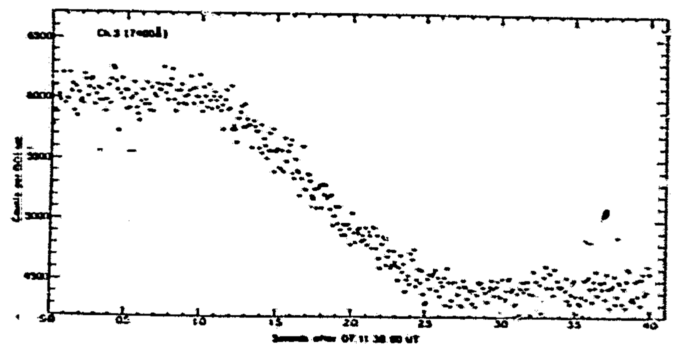

FIG. 2. Occultation light curve for Titan obtained with the 224 cm telescope at Mauna Kea Observatory. Each data point represents a 0.01 sec integration.

tion curve can correspond to many different brightness distributions, each yielding the same value when integrated over the occulted strip. In principle it is possible to uniquely recover any brightness distribution from the light curves of several occultations, if each occurred with a different angle between the direction of lunar limb motion and the polar axis of the satellite; in practice this situation is unlikely to be realized.

However, an approximation of the brightness distribution on a satellite's disk can be recovered from a single lunar occultation observation, if we are willing to assume that the distribution is symmetric about the center of the disk. Consider the model satellite with three concentric rings, shown in Fig. 3. The central ring (a circle) has unit radius; the inner radius of the ith ring is $(i-1)$ and its outer radius is i. Within the ith ring the brightness is assumed to have a constant value b_i per unit area of the ring system. Hence the ith ring contributes a fraction $\pi(2i-1)b_i$ of the total light reflected by the satellite. This normalization implies that the total light reflected from the satellite is unity: $\sum_{i=1}^{N} \pi(2i-1)b_i = 1.0$, for a satellite of N rings.

From Fig. 3 we see that we can find the value of b_3 from the intensity difference $(I_3 - I_2)$ and the area of the third ring intersected by the third strip. In general, any b_i can be computed from the drop in light intensity across the ith strip, the areas of the rings intersected by the ith strip and the b_i values for the rings exterior to the ith ring. However, for direct evaluation of errors in the b_i, we shall find it expedient to eliminate the dependence of each b_i on the b_i values of exterior rings. We express each b_i in terms of the light curve intensities I_j:

$$b_i = \sum_{j=0}^{N} c_{ij} I_j, \qquad (1)$$

where N is the number of rings used to construct the model satellite. The coeffi-

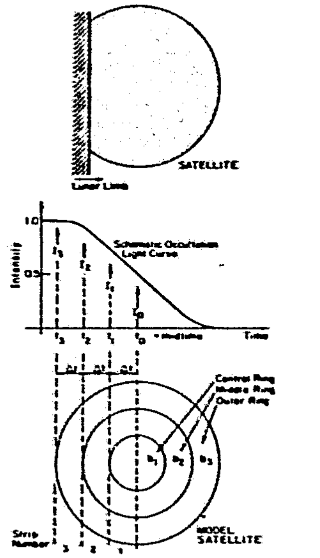

FIG. 3. Model satellite for computing central reflectances. When a satellite is occulted by the lunar limb, the observed light curve is the strip brightness distribution of the satellite. If we assume that the limb darkening of the satellite is symmetric about its center, the average reflectance for each ring of a concentric system can be recovered from the occultation light curve. The reflectance of the central ring, for all practical purposes, equals the normal reflectance of the satellite's visible disk.

cients c_{ij}, which depend on the areas defined by ring and strip boundaries, are given in Table II for model satellites consisting of 2, 3, 4, and 5 rings.

To obtain the intensities I_j required by (1), we must normalize the light curves and integrate the result over a time interval t, centered about the time t_j. Following Paper I, the instantaneous photon counting rate is denoted by $n(t)$, and the desired intensity I_j is given by

$$I_j = (1/\Delta t) \int_{t_j-\Delta t/2}^{t_j+\Delta t/2} (1/n_s) \times \{n(t) - [\alpha + \beta(t - t_0)]\} dt, \quad (2)$$

TABLE II

INVERSION COEFFICIENTS c_{ij}

Ring No. (i)	Intensity number (j)					
	0	1	2	3	4	5
a. 2 rings						
1	−0.63662	1.22113	−0.58451			
2	0	−0.40704	0.40704			
b. 3 rings						
1	−0.63662	1.22113	−0.66976	0.08525		
2	0	−0.40704	0.76133	−0.35428		
3	0	0	−0.32284	0.32284		
c. 4 rings						
1	−0.63662	1.22113	−0.66976	0.15378	−0.06853	
2	0	−0.40704	0.76133	−0.40632	0.05203	
3	0	0	−0.32284	0.59908	−0.27624	
4	0	0	0	−0.27575	0.27575	
d. 5 rings						
1	−0.63662	1.22113	−0.66976	0.15378	−0.06638	−0.00215
2	0	−0.40704	0.76133	−0.40632	0.09735	−0.04532
3	0	0	−0.32284	0.59908	−0.31839	0.04215
4	0	0	0	−0.27575	0.50973	−0.23398
5	0	0	0	0	−0.24465	0.24465

where n_s is the unocculted satellite counting rate and $[\alpha + \beta(t - t_0)]$ is the background counting rate. Values of the constants α, β, t_0, and n were obtained from Tables II and VI of Paper I.

Since photon noise (not scintillation) is the principal source of noise in these occultation light curves, the intensities I_j are uncorrelated random variables, and the variances $\sigma^2(b_i)$ are given by the usual equation for error propagation (Young, 1962):

$$\sigma^2(b_i) = \sum_{j=0}^{N} c_{ij}^2 \sigma^2(I_j), \qquad (3)$$

where $\sigma^2(I_j)$ are the variances of the intensities I_j, arising from photon noise. To reduce errors in b_i caused by photon noise, we can sum the light curves of all channels. Additionally, if the assumption of radial symmetry of the brightness distribution is correct, the summed light curve can be folded about the midtime t_m, forming a new set of intensities I_j':

$$I_j' = \tfrac{1}{2}[I_j + (1 - I_{-j})]. \qquad (4)$$

We now demonstrate, that to the accuracy of the data, the brightness distribution on each satellite disk is independent of color and is radially symmetric. Thus we are justified in summing the light curves for our four channels and in folding the summed light curves about their midtimes.

III. TESTING THE ASSUMPTIONS

For each satellite we must test the two assumptions on which (4) is based. This procedure is best illustrated using the Titan light curves since these data have the highest signal-to-noise ratio.

First, we shall verify that at each wavelength the Titan light curves can be folded about the midtime t_0. Using (1) and (2) we calculate b_i's for each of the four light curves using $N = 3$ and $\Delta t = 0.34$ sec. As discussed below, a three-ring model ($N = 3$) is a good choice for the Titan data. For $\Delta t = 0.34$ sec the outer diameter of the third ring corresponds to 5975 km at the distance of Titan. The values of b_1, b_2, and b_3 calculated for Titan using (a) the first half, (b) the second half, and (c) the folded light curve are given in Table III. The b_i's obtained for cases (a), (b), and (c) agree within their errors (except perhaps for ring 2, where the difference between the results for the two halves of the light curve may be significant). We conclude that in general we are justified in using the folded data in our Titan analysis. Similar calculations show that this assumption is also valid for the other satellites.

Next, we verify that in the case of the Titan data the light curves from all four channels may be summed to increase the signal-to-noise ratio.

The values of b_i ($i = 1, 2, 3$) computed for the folded light curves are plotted as a function of wavelength in Fig. 4. Within the error bars no color dependence is evident. Thus, in the case of Titan the light curves for all four channels may be summed (cf. Table III). Similarly, the validity of this procedure can be verified for the other satellites

Thus we conclude that for all satellites we can use the summed and folded light curves in our analysis.

IV. SENSITIVITY OF METHOD TO OTHER ASSUMPTIONS

In our discussion of the Titan data in Section III we used $N = 3$ (three rings) and $\Delta t = 0.34$ sec (corresponding to a diameter of 5975 km for the three rings at the distance of Titan) in (2). We now demonstrate that the calculated b_i's are not very sensitive to the specific choice of these parameters.

Values of b_i for Titan calculated from the summed and folded light curves for $\Delta t = 0.34$ sec and for $N = 3$, 4, and 5 are compared in Table IV. We see that the addition of a fourth and fifth ring does not affect the values of b_1 and b_2; even the value of b_3 is not affected significantly. Thus we conclude that our choice of $N = 3$ has not biased the values of b_1 and b_2 derived from our analysis.

In calculating the normal reflectances of the satellites, we define b_i' to be the fraction of the total light reflected by the satellite per square kilometer for the ith ring. The b_i' are related to the ring brightnesses b_i for an N ring model satellite and the satellite diameter d by the equation

$$b_i' = b_i(d)[2N/d]^2. \qquad (5)$$

In writing (5) we have indicated the functional dependence of the b_i on the assumed diameter d. This dependence exists because, by their definition, the b_i's depend on the choice of Δt, and d is determined by the choice of Δt through the relation

$$d = 2N[\rho\Delta\Delta t/206265], \qquad (6)$$

where ρ (arcsec sec^{-1}) is the radial rate of the lunar limb (Table VII of Paper I); Δ, (km) the topocentric distance to the satellite and 206265 the number of arc seconds in a radian.

Figure 5 shows the values of b_i' calculated from the summed and folded Titan data for $N = 3$, as a function of Δt (or diameter). Since the basic time resolution of the data is 10 msec, we have incremented Δt by 20 msec per ring in Fig. 4. For $N = 3$ this corresponds to diameter increments of about 400 km. Considering the error bars, we see that b_1' is independent of the choice of Δt. The value of b_2' is weakly sensitive to Δt while b_3' is very sensitive to the choice of this parameter. Since the main purpose

TABLE III

NORMALIZED SURFACE BRIGHTNESSES (b_i) FOR TITAN

Channel No.	Portion of occultation light curve		
	First half	Last half	Folded
a. b_1 (ring 1, center)			
1	0.058 ± 0.010	0.061 ± 0.007	0.060 ± 0.006
2	0.066 ± 0.013	0.048 ± 0.011	0.057 ± 0.008
3	0.055 ± 0.018	0.044 ± 0.015	0.050 ± 0.010
4	0.046 ± 0.012	0.059 ± 0.009	0.053 ± 0.009
Data added	0.058 ± 0.007	0.053 ± 0.005	0.055 ± 0.004
b. b_2 (ring 2)			
1	0.058 ± 0.006	0.044 ± 0.004	0.051 ± 0.004
2	0.049 ± 0.008	0.044 ± 0.007	0.046 ± 0.005
3	0.056 ± 0.011	0.048 ± 0.009	0.052 ± 0.006
4	0.058 ± 0.007	0.044 ± 0.006	0.051 ± 0.005
Data added	0.055 ± 0.004	0.045 ± 0.003	0.050 ± 0.003
c. b_3 (ring 3)			
1	0.017 ± 0.003	0.023 ± 0.002	0.020 ± 0.002
2	0.022 ± 0.004	0.024 ± 0.003	0.023 ± 0.002
3	0.020 ± 0.005	0.024 ± 0.005	0.022 ± 0.003
4	0.020 ± 0.004	0.026 ± 0.003	0.023 ± 0.003
Data added	0.020 ± 0.002	0.024 ± 0.002	0.022 ± 0.001

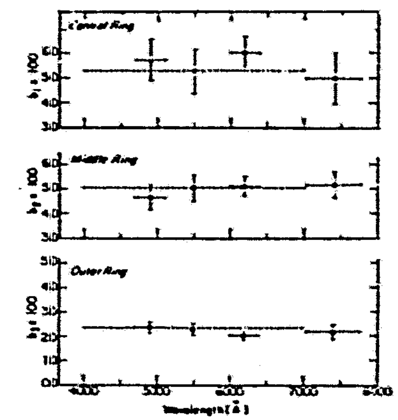

FIG. 4. Normalized ring brightness for Titan. The vertical bars indicate the ±σ errors from photon noise in the light curves, while the horizontal bars represent the wavelength passbands. No significant variation with wavelength is seen, implying that for these passbands the limb darkening of Titan is independent of wavelength to the accuracy of the data (see text).

TABLE IV

NORMALIZED SURFACE BRIGHTNESSES FOR TITAN[a]

No. of rings	b_1 (ring 1, center)	b_2 (ring 2)	b_3 (ring 3)	b_4 (ring 4)	b_5 (ring 5)
3	0.055 ± 0.004	0.050 ± 0.003	0.0221 ± 0.0013	—	—
4	0.055 ± 0.004	0.050 ± 0.003	0.0204 ± 0.0021	0.0017 ± 0.0011	—
5	0.055 ± 0.004	0.050 ± 0.003	0.0207 ± 0.0021	0.0002 ± 0.0018	0.0015 ± 0.0010

[a] Extra rings added.

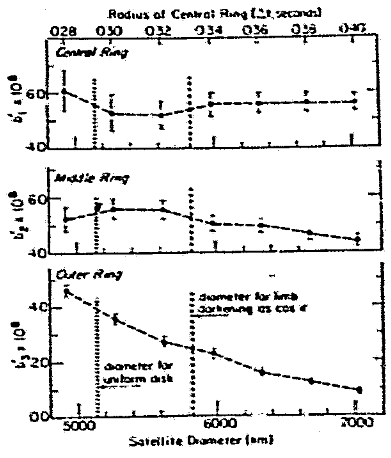

FIG. 5. Normalized ring brightness for Titan. The computed brightness of the central ring is insensitive to the assumed diameter of Titan. The diameters corresponding to no limb darkening ($k = 0.5$) and to limb darkening according to Lambert's law ($k = 1.0$) are indicated (cf. Paper I).

of this paper is to determine b_1, we can conclude that the method is insensitive to the choice of Δt (i.e., independent of the actual satellite diameter).

The above conclusions can be extended to the other satellites, with the important modification that since they are considerably fainter than Titan, only two rings can be used if the random errors in the calculated value of b_1 are to be kept at a reasonable level. Again one can demonstrate that the values of b_1 are not biased significantly by the choice of $N = 2$ or the specific value of Δt used. For example, in Fig. 6, we show the calculated values of b_1' and b_2' as a function of Δt for the summed and folded observations of Rhea. Within the error bars we see that even for $N = 2$, b_1' (and hence b_1) is not sensitive to the precise choice of Δt (that is, to the actual diameter).

The final assumption that we must test is that the b_i' values, particularly b_1', are not dependent on how many rings we fit to a particular satellite diameter. Figure 7 shows the b_i' values calculated from the summed and folded Titan light curves for $N = 3$, 4, and 5 models where $2N\Delta t$ is approximately constant. Because of the finite time resolution of the data, it was not possible to have these models fit exactly the same satellite diameter. It is important to note that the profiles and the b_1' values for the three models agree within their error bars, showing that the method is independent of the number of rings we fit to a given satellite diameter.

It is also interesting to see that the error bars for the $N = 4$ and $N = 5$ models are considerably larger than those for the $N = 3$ model. This is the major reason that the $N = 3$ model was chosen as the final one for Titan.

Similar conclusions result from the application of this analysis to the other satellite light curves with the exception that the $N = 2$ model is the optimum one for these satellites.

V. NORMAL REFLECTANCE

We have demonstrated that reliable values of b_1, the brightness of the central

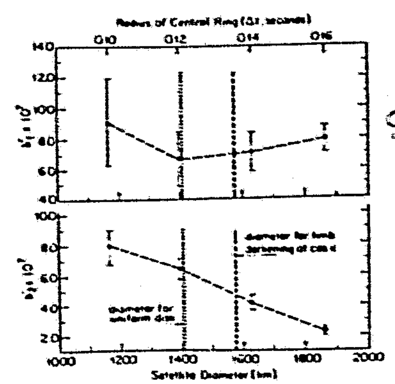

FIG. 6. Normalized ring brightnesses for Rhea. The computed brightness of the central ring is insensitive to the assumed diameter of Rhea.

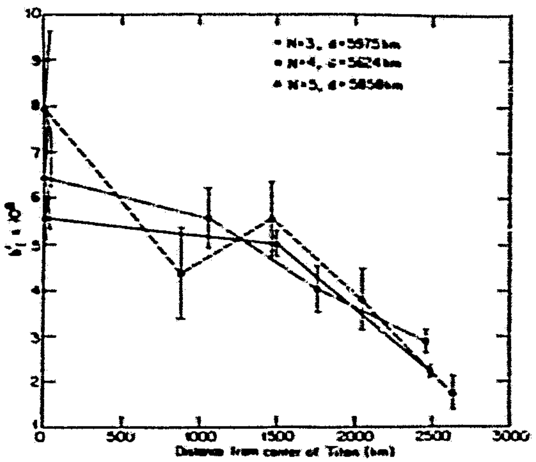

FIG. 7. Normalized ring brightnesses for Titan. The computed brightness profile and central ring brightness are independent of the number of rings (N) used for models with a fixed satellite diameter ($2N\Delta t$ = constant, see text).

portion of an occulted satellite, can be calculated with the method outlined in Section II. We now show that the value of b_1 can be used to obtain an accurate estimate of the normal reflectance of the satellite surface.

Let $r_i(\alpha, \theta, \lambda)$ be the average reflectance of the satellite's ith ring at a wavelength λ when the solar phase angle is α and the orbital longitude of the satellite is θ, and define $r_i(\alpha, \theta, \lambda)$ relative to a perfectly reflecting, plane Lambert ring, whose surface normal points toward the Sun. This definition implies that if the satellite were replaced by a Lambert disk (not a sphere), then $r_i(\alpha, \theta, \lambda)$ would equal 1.00 for all rings.

Since within the accuracy of our data the derived b_i's are independent of wavelength for the colors observed, we will assume that they apply to the V passband as well. Let $V(\alpha, \theta)$ be the visual magnitude of the satellite as a function of solar phase angle α and orbital longitude θ, but referred to the mean opposition distance of Saturn from the Earth ($R = 8.54$ AU) and the Sun ($\Delta = 9.54$ AU). Then:

$$r_1(\alpha, \theta, V) = \pi b_1'[1.50 \times 10^8 (\mathrm{km/AU}) R\Delta]^2 \times 10^{-0.4[V(\alpha,\theta) - V_{\odot}]}, \quad (7)$$

where b_1' is given in terms of b_1 by (5), 1.50×10^8 is the number of kilometers in 1 AU, R, and Δ are mean opposition distance in AU, and $V_{\odot} = -26.77$ (Gehrels *et al.*, 1964).

This reflectance, $r_1(\alpha, \theta, V)$, which we shall call the central reflectance of the satellite, is the average reflectance of the central portion of the disk enclosed by ring 1. Computed values of $r_1(\alpha, \theta, V)$ for the five occulted satellites are given in Table V.

Strictly these values apply only to the satellite faces visible at the time of the occultations. Next we estimate $r_1(V)$, the average normal reflectance of the entire satellite surface in the V passband, averaged over orbital longitude.

From (7), we can write

$$\frac{r_1(\alpha, \theta, V)}{r_1(0°, \bar{\theta}, V)} = \frac{b_1(\alpha, \theta, V)}{b_1(0°, \bar{\theta}, V)} \times \left[\frac{10^{-0.4(V(\alpha,\theta)-V_{\odot})}}{10^{-0.4(V(0°,\bar{\theta})-V_{\odot})}}\right], \quad (8)$$

where $\bar{\theta}$ denotes an orbital longitude at which the satellite achieves its mean brightness (averaged over θ), and $V(0°, \bar{\theta})$ is the mean opposition magnitude which from now on will be denoted by $\bar{V}(0°)$.

Given the likely assumption that the degree of limb darkening over the disk does not change strongly between $\alpha = 6°.26$ and $\alpha = 0°$, it follows from the definition of b_1 that the ratio of the b_1 terms in the above expression can be taken to be unity. In effect, if we represent the limb darkening by a Minnaert law we are assuming that in k would not change for values of α between 0° and 6°.26. Hence

$$r_1(0°, \bar{\theta}, V) \simeq r_1(\alpha, \theta, V)10^{-0.4\Delta V}, \quad (9)$$

where $\Delta V \equiv \bar{V}(0°) - V(\alpha, \theta)$.

Finally we must relate the central reflectance which refers to the average reflectance of the finite spherical cap enclosed within the first ring to the average normal reflectance of the material: $\bar{r}_1(V)$. To convert $r_1(0°, \bar{\theta}, V)$ to $\bar{r}_1(V)$ we assume that the limb darkening follows a Minnaert law with an exponent k, since the correction does not depend strongly on the value of k. For a satellite divided into N rings, we find

$$\bar{r}_1(V) = r_1(0°, \bar{\theta}, V) \times [m(1-\gamma)/(1-\gamma^m)], \quad (10)$$

where $m = 2k$, and $\gamma = (1 - 1/N^2)^{1/2}$. The bracketed correction is close to unity for most practical cases of interest. For example for $N = 3$, it equals 1.03 for $k = 1.0$; for $N = 2$ it equals 1.07 for $k = 1.0$. For $k = 0.5$ the correction term is unity, independent of N.

The average normal reflectances for Rhea, Titan, and the bright face of Iapetus, computed from (10) are given in Table VI. The corresponding values for Tethys and Dione have been omitted due to the large errors in the central reflectances of these two satellites (Table V). Note that the values of k indicated in Table VI have been assumed, but that the results are only weakly dependent on this assumption (see above).

In computing the errors in $\bar{r}_1(V)$ given in Table VI, we have included (i) the shot noise errors in b_1' (Table V), (ii) an estimated uncertainty of $\pm 0^m.05$ for $V_{\odot}$, (iii) errors in the mean opposition magnitudes (Noland *et al.*, 1974), (iv) changes in b_1' (about $\pm 7\%$) for different assumed satellite diameters over the range for k (Figs. 5 and 6), and (v) uncertainties in the cap correction factor [Eq. (10)] resulting

TABLE V

CENTRAL RING REFLECTANCES

Satellite	No. of rings	Δt[a] (sec)	Diameter of central ring (km)	b_1	Orbital longitude (θ, deg)	Magnitude $V(\alpha, \theta)$[b]	Central reflectance $r_1(\alpha, \theta, V)$
Tethys	2	0.10	578	0.13 ± 0.04	332	10.41 ± 0.09	1.0 ± 0.3
Dione	2	0.08	465	0.14 ± 0.08	22	10.44 ± 0.05	1.6 ± 0.9
Rhea	2	0.14	313	0.12 ± 0.02	227	9.93 ± 0.02	0.71 ± 0.12
Titan	3	0.34	1992	0.055 ± 0.004	128	8.37 ± 0.01	0.228 ± 0.017
Iapetus[c]	2	0.16	843	0.14 ± 0.03	273	10.44 ± 0.04	0.48 ± 0.10

[a] Δt chosen such that ring system is the smallest one definitely enclosing the satellite.
[b] $R = 9.54$ AU, $\Delta = 8.54$ AU, $V_{\odot} = -26.77$ (Gehrels *et al.*, 1964), $\alpha = 6°.26$.
[c] Bright side only.

TABLE VI

AVERAGE NORMAL REFLECTANCES

Satellite	Minnaert limb darkening parameter, k[a]	Mean opposition magnitude[b]	Av normal reflectance for 0° solar phase angle, $\bar{r}_1(V)$
Rhea	1.0 ± 0.5	9.67 ± 0.01	0.97 ± 0.20
Titan	$1.25^{+0.75}_{-0.25}$	8.34 ± 0.01	0.24 ± 0.03
Iapetus[c]	0.75 ± 0.25	10.24 ± 0.02	0.60 ± 0.14

[a] The errors in k are guesses.
[b] Noland *et al.* (1974).
[c] Bright hemisphere.

from the uncertainties in k. For each satellite the errors were added quadratically. Although this is not a statistically rigorous procedure, we believe that it yields a realistic estimate of the true uncertainties in the normal reflectances.

CONCLUSIONS

We have demonstrated that the normal reflectance of the central portion of a satellite's disk can be estimated from a lunar occultation light curve and that this estimate does not depend strongly on the actual diameter or on the limb darkening law. The normal reflectances derived in this paper for Tethys, Dione, Rhea, and the bright face of Iapetus are high, and are consistent with values expected for frost covered surfaces. We note that our value of the normal reflectance of the bright face of Iapetus (0.60 ± 0.14) is at best only marginally consistent with the value of about 0.35 derivable from the radiometric analysis of Morrison *et al.* (1975). (cf. Veverka *et al.*, 1978 for details).

For Titan we conclude that the normal reflectance in the V passband is 0.24 ± 0.03. We recall that in Paper I we showed that the disk of Titan is highly limb darkened and that the satellite's diameter is certainly ≳5800 km, and possibly may exceed 6200 km (cf. Fig. 14 of Paper I). We also note that our data place limits on the color dependence of the limb darkening of Titan. If the Minnaert law is used as reference form for the limb darkening, we found that the difference between the value of k for any two of the wavelength bands that we used (cf. Fig. 1) is ≲0.1 (cf. Table V of Paper I).

ACKNOWLEDGMENTS

We appreciate the observing time which was made available to us by the Mauna Kea Observatory and thank the MKO staff for their assistance. D. Morrison, T. Jones, and J. Bart provided helpful discussions. This research was supported by NASA Grants NGR 33-010-082 and NSG 7126.

REFERENCES

ELLIOT, J. L., VEVERKA, J., AND GOGUEN, J. (1975). Lunar occultation of Saturn. I. The diameters of Tethys, Dione, Rhea, Titan, and Iapetus. *Icarus* 26, 387–407.

GEHRELS, T., COFFEEN, T., AND OWINGS, D. (1964). Wavelength dependence of polarization. III, The lunar surface. *Astron. J.* 69, 826–852.

McCORD, T. B., JOHNSON, T. V., AND ELIAS, J. H. (1971). Saturn and its satellites: Narrow-band spectrophotometry. *Astrophys. J.* 165, 413–424.

MORRISON, D., JONES, T. J., CRUIKSHANK, D. P., AND MURPHY, R. E. (1975). The two faces of Iapetus. *Icarus* 24, 157–171.

NOLAND, M., VEVERKA, J., MORRISON, D., CRUIKSHANK, D. P., LAZAREWICZ, A. R., MORRISON, N. D., ELLIOT, J. L., GOGUEN, J., AND BURNS, J. A. (1974). Six-color photometry of Iapetus, Titan, Rhea, Dione, and Tethys. *Icarus* 23, 334–354.

VEVERKA, J., BURT, J., ELLIOT, J. L., AND GOGUEN, J. (1978). Lunar occultation of Saturn. III. How big is Iapetus? *Icarus* 33, 301–310.

YOUNG, H. D. (1962). *Statistical Treatment of Experimental Data*, pp. 96–98. McGraw-Hill, New York.

ORIGINAL PAGE IS
OF POOR QUALITY

From (7), we can write

$$\frac{r_1(\alpha, \theta, V)}{r_1(0°, \bar\theta, V)} = \frac{b_1(\alpha, \theta, V)}{b_1(0°, \bar\theta, V)} \times \left[\frac{10^{-0.4(V(\alpha,\theta)-V_\odot)}}{10^{-0.4(V(0,\bar\theta)-V_\odot)}}\right], \quad (8)$$

where $\bar\theta$ denotes an orbital longitude at which the satellite achieves its mean brightness (averaged over θ), and $V(0°, \bar\theta)$ is the mean opposition magnitude which from now on will be denoted by $\bar V(0°)$.

Given the likely assumption that the degree of limb darkening over the disk does not change strongly between $\alpha = 6°.26$ and $\alpha = 0°$, it follows from the definition of b_1 that the ratio of the b_1 terms in the above expression can be taken to be unity. In effect, if we represent the limb darkening by a Minnaert law we are assuming that in k would not change for values of α between 0° and 6°.26. Hence

$$r_1(0°, \bar\theta, V) \simeq r_1(\alpha, \theta, V)10^{-0.4\Delta V}, \quad (9)$$

where $\Delta V \equiv \bar V(0°) - V(\alpha, \theta)$.

Finally we must relate the central reflectance which refers to the average reflectance of the finite spherical cap enclosed within the first ring to the average normal reflectance of the material: $\bar r_1(V)$. To convert $r_1(0°, \bar\theta, V)$ to $\bar r_1(V)$ we assume that the limb darkening follows a Minnaert law with an exponent k, since the correction does not depend strongly on the value of k. For a satellite divided into N rings, we find

$$\bar r_1(V) = r_1(0°, \bar\theta, V) \times [m(1-\gamma)/(1-\gamma^m)], \quad (10)$$

where $m = 2k$, and $\gamma = (1 - 1/N^2)^{1/2}$. The bracketed correction is close to unity for most practical cases of interest. For example for $N = 3$, it equals 1.03 for $k = 1.0$; for $N = 2$ it equals 1.07 for $k = 1.0$. For $k = 0.5$ the correction term is unity, independent of N.

The average normal reflectances for Rhea, Titan, and the bright face of Iapetus, computed from (10) are given in Table VI. The corresponding values for Tethys and Dione have been omitted due to the large errors in the central reflectances of these two satellites (Table V). Note that the values of k indicated in Table VI have been assumed, but that the results are only weakly dependent on this assumption (see above).

In computing the errors in $\bar r_1(V)$ given in Table VI, we have included (i) the shot noise errors in b_1' (Table V), (ii) an estimated uncertainty of $\pm 0^m.05$ for $V_\odot$, (iii) errors in the mean opposition magnitudes (Noland *et al.*, 1974), (iv) changes in b_1' (about $\pm 7\%$) for different assumed satellite diameters over the range for k (Figs. 5 and 6), and (v) uncertainties in the cap correction factor [Eq. (10)] resulting

TABLE V

CENTRAL RING REFLECTANCES

Satellite	No. of rings	Δt[a] (sec)	Diameter of central ring (km)	b_1	Orbital longitude (0, deg)	Magnitude $V(\alpha, \theta)$[b]	Central reflectance $r_1(\alpha, \theta, V)$
Tethys	2	0.10	578	0.13 ± 0.04	332	10.41 ± 0.09	1.0 ± 0.3
Dione	2	0.08	465	0.14 ± 0.08	22	10.44 ± 0.05	1.6 ± 0.9
Rhea	2	0.14	813	0.12 ± 0.02	227	9.93 ± 0.02	0.71 ± 0.12
Titan	3	0.34	1992	0.055 ± 0.004	128	8.37 ± 0.01	0.228 ± 0.017
Iapetus[c]	2	0.16	843	0.14 ± 0.03	273	10.44 ± 0.04	0.48 ± 0.10

[a] Δt chosen such that ring system is the smallest one definitely enclosing the satellite.
[b] $R = 9.54$ AU, $\Delta = 8.54$ AU, $V_\odot = -26.77$ (Gehrels *et al.*, 1964), $\alpha = 6°.26$.
[c] Bright side only.

TABLE VI

AVERAGE NORMAL REFLECTANCES

Satellite	Minnaert limb darkening parameter, k[a]	Mean opposition magnitude[b]	Av normal reflectance for 0° solar phase angle, $\bar r_1(V)$
Rhea	1.0 ± 0.5	9.67 ± 0.01	0.97 ± 0.20
Titan	$1.25^{+0.75}_{-0.25}$	8.34 ± 0.01	0.24 ± 0.03
Iapetus[c]	0.75 ± 0.25	10.24 ± 0.02	0.60 ± 0.14

[a] The errors in k are guesses.
[b] Noland *et al.* (1974).
[c] Bright hemisphere.

from the uncertainties in k. For each satellite the errors were added quadratically. Although this is not a statistically rigorous procedure, we believe that it yields a realistic estimate of the true uncertainties in the normal reflectances.

CONCLUSIONS

We have demonstrated that the normal reflectance of the central portion of a satellite's disk can be estimated from a lunar occultation light curve and that this estimate does not depend strongly on the actual diameter or on the limb darkening law. The normal reflectances derived in this paper for Tethys, Dione, Rhea, and the bright face of Iapetus are high, and are consistent with values expected for frost covered surfaces. We note that our value of the normal reflectance of the bright face of Iapetus (0.60 ± 0.14) is at best only marginally consistent with the value of about 0.35 derivable from the radiometric analysis of Morrison *et al.* (1975). (cf. Veverka *et al.*, 1978 for details).

For Titan we conclude that the normal reflectance in the V passband is 0.24 ± 0.03. We recall that in Paper I we showed that the disk of Titan is highly limb darkened and that the satellite's diameter is certainly $\gtrsim 5800$ km, and possibly may exceed 6200 km (cf. Fig. 14 of Paper I). We also note that our data place limits on the color dependence of the limb darkening of Titan. If the Minnaert law is used as reference form for the limb darkening, we found that the difference between the value of k for any two of the wavelength bands that we used (cf. Fig. 1) is ≤ 0.1 (cf. Table V of Paper I).

ACKNOWLEDGMENTS

We appreciate the observing time which was made available to us by the Mauna Kea Observatory and thank the MKO staff for their assistance. D. Morrison, T. Jones, and J. Burt provided helpful discussion. This research was supported by NASA Grants NGR 33-010-082 and NSG 7126.

REFERENCES

ELLIOT, J. L., VEVERKA, J., AND GOGUEN, J. (1975). Lunar occultation of Saturn. I. The diameters of Tethys, Dione, Rhea, Titan, and Iapetus. *Icarus* 26, 387–407.

GEHRELS, T., COFFEEN, T., AND OWINGS, D. (1964). Wavelength dependence of polarization. III. The lunar surface. *Astron. J.* 69, 826–852.

MCCORD, T. B., JOHNSON, T. V., AND ELIAS, J. H. (1971). Saturn and its satellites: Narrow-band spectrophotometry. *Astrophys. J.* 165, 413–424.

MORRISON, D., JONES, T. J., CRUIKSHANK, D. P., AND MURPHY, R. E. (1975). The two faces of Iapetus. *Icarus* 24, 157–171.

NOLAND, M., VEVERKA, J., MORRISON, D., CRUIKSHANK, D. P., LAZAREWICZ, A. R., MORRISON, N. D., ELLIOT, J. L., GOGUEN, J., AND BURNS, J. A. (1974). Six-color photometry of Iapetus, Titan, Rhea, Dione, and Tethys. *Icarus* 23, 334–354.

VEVERKA, J., BURT, J., ELLIOT, J. L., AND GOGUEN, J. (1978). Lunar occultation of Saturn. III. How big is Iapetus? *Icarus* 33, 301–310.

YOUNG, H. D. (1962). *Statistical Treatment of Experimental Data*, pp. 96–98. McGraw-Hill, New York.

ICARUS 33, 301–310 (1978)

Lunar Occultation of Saturn

III. How Big Is Iapetus?

J. VEVERKA, J. BURT, J. L. ELLIOT, AND J. GOGUEN

Laboratory for Planetary Studies, Cornell University, Ithaca, New York 14853

Received April 13, 1977; revised June 30, 1977

By considering both the orbital lightcurve of Iapetus and data obtained during the March 30, 1974, occultation of the satellite by the Moon, we obtain information about the brightness distribution on the bright face of Iapetus and derive an accurate value for the satellite's radius. From the observed orbital lightcurve we find that the trailing face of Iapetus must consist predominantly of a single bright material with an effective limb-darkening parameter of $k = 0.62^{+0.10}_{-0.12}$. Given this result the occultation observations imply a radius of 718^{+37}_{-75} km. If the patchy albedo model proposed by Morrison *et al.* represents the surface of Iapetus accurately (as far as the relative albedo distribution is concerned) then the radius of Iapetus is 724 ± 60 km. Both estimates are consistent with the radiometric radius of 835 (+50, −75) km derived by Morrison *et al.* Combining our results with the value of 0.60 ± 0.14 for the normal reflectance (in V) of the material at the center of the bright face derived by Elliot *et al.* we find that the normal reflectance of the dark side material is $0.11^{+0.04}_{-0.03}$. These values are higher than the corresponding values of 0.35 and 0.05 quoted by Morrison *et al.*

1. INTRODUCTION

Various attempts have been made to determine the size of Iapetus. Methods based on measuring the apparent size of the satellite in a telescope are uncertain since Iapetus subtends, at best, only 0.3 arcsec. The best measurements of this type, the diskmeter measurements quoted by Dollfus (1970), give a radius of 650 ± 200 km (see Elliot *et al.*, 1975).

More recently, Morrison and his collaborators used the "radiometric method" described by Morrison (1973) to determine the radius. Their original value was 850 ± 100 km, but subsequent refinements both in the technique and in the observations led to their current value of 835 (+50, −75) km (Morrison *et al.*, 1975).

In this paper we present an independent determination of the radius based on observations of an occultation of Iapetus by the Moon on March 30, 1974. These observations have already been published by Elliot *et al.* (1975). It is noted in that paper that for Iapetus, the signal-to-noise ratio achieved during the occultation did not allow independent determinations of *both* (i) the absolute radius, and (ii) the brightness distribution across the disk. Elliot *et al.* (1975) derived two radii for Iapetus from their data; the first, 694 ± 58 km, assuming no limb darkening; the second, 798 ± 70 km, assuming limb darkening according to Lambert's law. In the present paper we exploit the fact that the large periodic brightness variations that Iapetus exhibits as it orbits Saturn constrain possible brightness distributions on its surface, and attempt to find models of Iapetus which satisfy *both* the observed orbital lightcurve, and the occultation observations made on March 30, 1974.

0019-1035/78/0332-0301$02.00/0

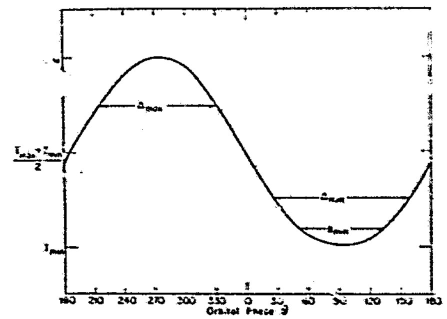

FIG. 1. Nominal lightcurve of Iapetus from Morrison *et al.* (1975) (their Fig. 5). The curve shown, based on observations by Millis (1973), Franklin and Cook (1974) and Noland *et al.* (1974), is plotted on a brightness scale. The total amplitude corresponds to 1.75 magnitudes. Three important lightcurve parameters Δ_{max}, Δ_{min}, and δ_{min}, defined in the text, are indicated.

For our purposes finding a suitable "model" amounts to finding an absolute radius and a brightness distribution on the surface which are consistent with the observations.

In agreement with previous investigators (e.g., Cook and Franklin, 1970; Morrison *et al.*, 1975) we find that the observed lightcurve requires a "two-faced" model of Iapetus—that is, a model in which the leading face of the satellite is almost completely covered with low-albedo material, while the trailing side is almost completely covered with bright material. Furthermore, the orbital lightcurve places useful constraints on the degree of limb darkening of the bright material, a fact which is crucial to our analysis since it was the bright face of Iapetus which was occulted on March 30, 1974. (Iapetus was occulted only 16 hours after its western elongation, so that its bright face was turned almost exactly toward the Earth.)

Having constrained the degree of limb darkening on the bright face, we are able to calculate the radius of the satellite from our occultation data using methods described in detail by Elliot *et al.* (1975).

2. ORBITAL BRIGHTNESS VARIATIONS

Reproducible light variations of Iapetus with a period equal to the satellite's orbital period about Saturn (79 days) have been observed for about three centuries, proving that the satellite's spin period is synchronous with its orbital period. It is generally argued that the large brightness variations which are observed are due to albedo differences on the surface and not to an irregular shape.

Modern photometric observations of the lightcurve of Iapetus are summarized by Millis (1973), Noland *et al.* (1974), Morrison *et al.* (1975), and Veverka (1977). A nominal lightcurve based on the data compiled by Morrison *et al.* (1975) in which longitude-dependent solar phase effects have been removed is shown in Fig. 1. Its significant characteristics can be summarized as follows:

(a) Maximum brightness occurs at Western Elongation (orbital longitude $\theta = 270°$); minimum brightness occurs at Eastern Elongation ($\theta = 90°$).

(b) The amplitude in V is about 1.75 magnitudes, corresponding to a brightness ratio of about 5 to 1 between the bright and dark sides.

(c) The lightcurve is only weakly wavelength dependent.

(d) Plotted on a linear brightness scale, the lightcurve is approximately sinusoidal.

Cook and Franklin (1970) and Morrison *et al.* (1975) have shown that only a limited class of models can reproduce the light curve in Fig. 1. One such model, developed by Morrison *et al.*, is shown in Fig. 2, and is discussed at length below. We note that the shape and amplitude of the lightcurve depend only on the relative albedos of the patches. The absolute albedos given in Fig. 2 are determined by the value of the absolute radius derived by Morrison *et al.* The albedo pattern shown in Fig. 2 reproduces the nominal observed lightcurve (Fig. 1) precisely.

To demonstrate how sensitive the lightcurve is to the brightness distribution on the surface, it is convenient to define the three lightcurve parameters Δ_{max}, Δ_{min}, and δ_{min} shown in Fig. 1.

If we represent the average disk-integrated intensity of Iapetus by

$$\langle I \rangle = (I_{max} + I_{min})/2,$$

the definitions of the above parameters are as follows:

Δ_{max} = width of the lightcurve (in degrees of orbital longitude) halfway between $\langle I \rangle$ and I_{max}, Δ_{min} = width of the lightcurve halfway between $\langle I \rangle$ and I_{min}, and δ_{min} = width of the lightcurve five-sixths of the way between $\langle I \rangle$ and I_{min}.

For Iapetus, in V, the observed values of these parameters are:

$\Delta_{max} = 114 \pm 5°$, $\Delta_{min} = 132 \pm 5°$, and $\delta_{min} = 75 \pm 5°$.

The uncertainty of $\pm 5°$ is estimated from the scatter in the observed data points.

These parameters provide a simple and convenient measure of the "shape" of the lightcurve and, as we are about to demonstrate, are very sensitive to the brightness distribution (including the limb darkening) on the bright side of Iapetus.

3. LIGHTCURVE MODELS

To appreciate the sensitivity of the lightcurve shape to the brightness distribution (including limb darkening) on the surface of Iapetus we begin by considering a family of very simple models which describes Iapetus as a spherical satellite with one uniformly limb-darkened bright hemisphere, and one uniformly limb-darkened dark hemisphere. Although no member of this family fits the lightcurve of Iapetus as well as the "spotted model" shown in Fig. 2, it is very easy to see from such an

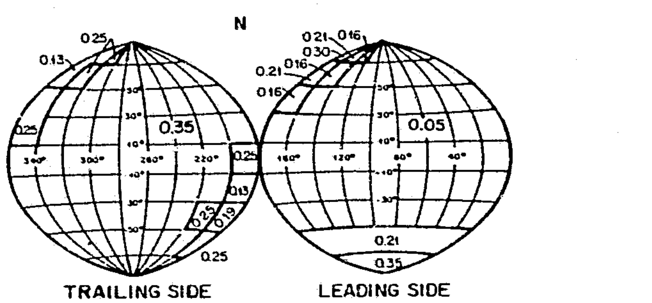

FIG. 2. Model albedo distribution on the surface of Iapetus derived by Morrison *et al.* (1975). This albedo distribution reproduces the lightcurve in Fig. 1 precisely. Note that the lightcurve shape and amplitude depend only on the relative albedos of the patches, and not on the absolute values. In the original paper the values shown are called *geometric albedos*, but according to Jones (private communication), they are in fact normal reflectances. According to our data (Section 7) the normal reflectance of the brightest material is 0.60 ± 0.14 and that of the darkest is $0.11^{+0.01}_{-0.03}$.

exercise how the shape of the lightcurve is affected by the degree of limb darkening.

The limb darkening can be described by either one of two convenient expressions. Since our observations are made very close to opposition we can assume that $i = \epsilon = \eta$ (where i = incidence angle and ϵ = emission angle) and write for the intensity of the scattered light

$$I(\eta) = (1 - b) + b \cos \eta, \quad (1)$$

or

$$I(\eta) = B_0 \cos^{2k-1} \eta, \quad (2)$$

where B_0 can be chosen equal to 1. The connection between these two representations is shown in Fig. 3. In general, the Minnaert representation (2) gives zero brightness at the limb (except for $k = \frac{1}{2}$), while the linear representation (1) gives a nonzero brightness at the limb (except for $b = 1$). It turns out that in practice the exact behavior of $I(\eta)$ near the limb is *not* important for our purposes. For example, the lightcurve for $k = 0.7$ is

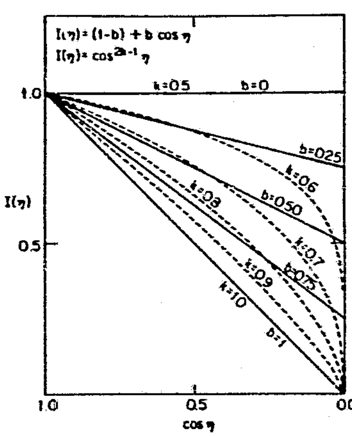

FIG. 3. Comparison of two models of limb darkening: a linear limb-darkening law characterized by a parameter b, and a Minnaert limb-darkening law characterized by a parameter k. The cases $b = 0$ and $k = 0.5$ coincide exactly, as do the cases $b = 1.0$ and $k = 1.0$.

similar to that for $b = 0.5$. Thus our results are essentially independent of the analytic form used to represent the limb darkening. We note that laboratory measurements (Veverka *et al.*, 1978) show that Minnaert's law gives a good representation of the limb darkening of most particulate materials near opposition.

We now consider simple models of Iapetus in which the leading hemisphere (seen at Eastern Elongation) is entirely dark, and the trailing hemisphere (seen at Western Elongation) is entirely bright.

The observed photometric characteristics of the leading hemisphere suggest that the surface material is at least as dark, and at least as porous, as the average lunar regolith (Veverka, 1977). We therefore expect that this material, like the lunar regolith, shows no limb darkening at opposition, so that $k \sim 0.5$, or $b \sim 0$.

Our main task is to estimate the amount of limb darkening displayed by the bright-side material. The recent discovery of water frost on the bright side of Iapetus by Morrison *et al.* (1976) and by Fink *et al.* (1976) suggests that k for the bright-side material may be as high as 1 (Veverka, 1973) if the frost cover on the bright side is complete. If the frost cover is not uniform, or if the texture of the frost is unusually rough, the effective value of k could be significantly less than unity (Veverka *et al.*, 1978). Fortunately, the observed lightcurve places significant constraints on the degree of limb darkening of the bright material.

Our simple model has a dark hemisphere which shows no limb darkening and a bright hemisphere which is limb darkened according to either (1) or (2). By centering the dark hemisphere at $\theta = 90°$ and the bright hemisphere at $\theta = 270°$ we immediately satisfy two key characteristics of the observed lightcurve (the locations of the maximum and minimum). The observed lightcurve amplitude fixes the ratio B_0(bright)/B_0(dark) once k(bright) is spec-

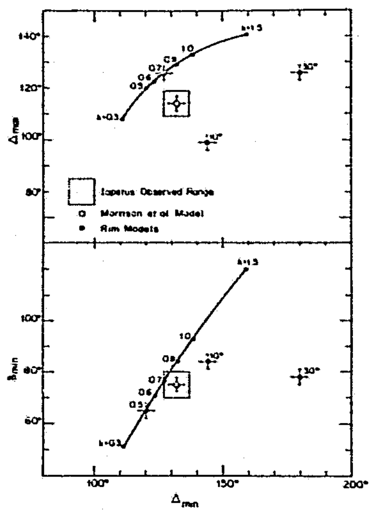

FIG. 4. Plots of the lightcurve parameters Δ_{max} vs Δ_{min} and of δ_{min} vs Δ_{min}, for various models. Values for the model of Morrison *et al.* (1975) agree closely with the observed values. A simple hemispherical model with Minnaert limb darkening is marginally consistent with the observations if $k \sim 0.6$–0.7. Models with dark rims (see text) are incompatible with the observed lightcurve.

ified. Since we have fixed k(dark) ~ 0.5, the shape of the lightcurve and specifically the parameters Δ_{max}, Δ_{min}, and Δ_{min} should be very sensitive to k (bright).

Figure 4 shows that this is in fact the case. Note that a plot of Δ_{max} against Δ_{min} (Fig. 4, top) provides a measure of the relative widths of the maximum peak and of the minimum trough, whereas a plot of Δ_{min} against δ_{min} (Fig. 4, bottom) provides a measure of the shape of the minimum trough. A little consideration makes it evident that a narrow (small Δ_{min}) and peaked (small δ_{min}) minimum trough requires either no limb darkening ($k \sim 0.5$) or limb brightening ($k < 0.5$) for the bright-side material. If the bright-side material is very limb darkened ($k \geqslant 1$) the minimum will be very broad (large Δ_{min}) and very flat-bottomed (large δ_{min}). It is also clear that a large value of k (say $k \geqslant 1$) leads to a small value of Δ_{max} and a large value of Δ_{min}, whereas if the degree of limb darkening is negligible, Δ_{min} and Δ_{max} are comparable.

Although none of the simple models in Fig. 4 fits the observed parameters exactly, we see that an effective brightside k of about 0.6 to 0.7 is indicated. Values of $k < 0.5$ give unacceptably small values of Δ_{min} and δ_{min}, while once k exceeds ~ 0.8, values of Δ_{max} become too large. It is clear from Fig. 4 that the bright side of Iapetus must have an effective limb-darkening parameter less than that for a Lambert surface ($k = 1$).

Figure 5 is the equivalent of Fig. 4, but for a linear limb-darkening law. No value of b gives an accurate match with the observed lightcurve parameters. A

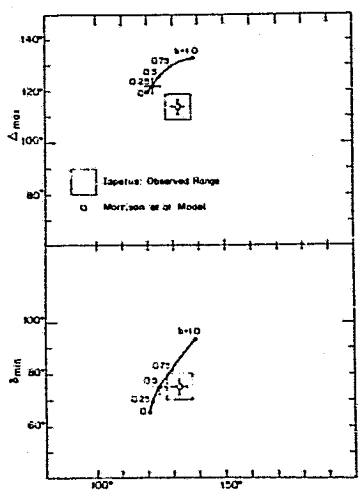

FIG. 5. Same as Fig. 4, but for a linear limb darkening law. Hemispherical models with $b \sim 0.2$–0.5 are marginally consistent with the observations, but a patchy model such as that of Morrison *et al.* (1975) is needed to reproduce the observed parameters precisely.

value of $b \sim 0.2$ to 0.5 appears to be a reasonable compromise; for $b \geqslant 0.7$, Δ_{max} becomes much too wide, while for $b \leqslant 0.1$, Δ_{min} becomes too narrow.

To better estimate the range of k (or b) consistent with the orbital lightcurve we have compared the observed lightcurve with the calculated lightcurves at 12 points at intervals of 30° in orbital longitude (i.e., at $\theta = 0°, 30°, 60°, \cdots$) and evaluated $\sum = (O - C)^2$, the sum of the squares of the residuals.

In Fig. 6 we have plotted $\sum$ as a function of k. We see that Δ reaches a minimum around $k = 0.62$; the formal one-sigma uncertainty in k is ± 0.05.

A plot of $\sum$ in terms of b gives a curve similar to that shown in Fig. 6. In this case, the minimum occurs at $b = 0.25$ and the formal one-sigma uncertainty is ± 0.15, values which are in good agreement with those obtained from the analysis in terms of k (cf. Fig. 3).

We stress that none of the above simple

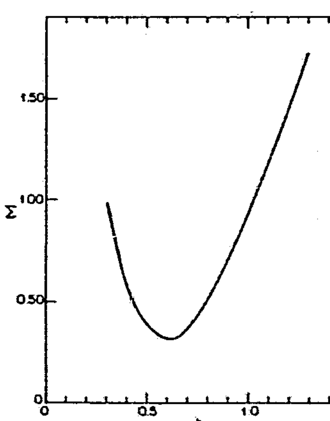

FIG. 6. Plot of Σ, the sum of the squares of the residuals $(O - C)$ for model lightcurves calculated for simple two-faced models. k is the limb darkening (Minnaert) parameter of the bright-side material. For the dark-side material $k = 0.5$ is assumed.

"two-faced" models matches the orbital lightcurve precisely.

To match the lightcurve precisely one must consider an albedo distribution which isn't precisely "two-faced." Unfortunately, "spotted" albedo distributions cannot be derived uniquely from the lightcurve (Russell, 1906) but one can produce models which match the observed lightcurve accurately. One such model produced by Morrison *et al.* (1975) has already been mentioned (Fig. 2). In that model some darkish material overlaps onto the bright hemisphere and some bright material overlaps onto the dark one. The brightest material is limb darkened according to (1) with $b = 0.5$, while the dark material shows no limb darkening. Note that the model of Morrison *et al.* matches the observed lightcurve precisely (Figs. 4 and 5) so that $\sum = 0$.

In summary, we conclude that the lightcurve of Iapetus requires an approximately, but not exactly, "two-faced" albedo distribution with the leading side essentially all dark and the trailing side essentially all bright. It is probable that the dark material shows no limb darkening. The best value of the limb-darkening parameter of the bright material is $k = 0.62^{+0.10}_{-0.12}$ (cf. Fig. 6), where we have quoted a conservative 3-sigma uncertainty.

4. ABSOLUTE RADII FROM OCCULTATION DATA

Once the albedo distribution on the trailing face of Iapetus has been specified, we can calculate the corresponding absolute radius from the occultation observations of Elliot *et al.* (1975), using the techniques described in that paper.

In essence the procedure used is as follows: Given a model of the brightness distribution on the bright side of Iapetus, a model lightcurve was generated by calculating the strip brightness at 75 equally spaced points on the disk. This number was chosen because it approximates the number of data points of 0.01-sec time resolution in the observed lightcurve across a satellite 700–800 km in radius. The model lightcurves were normalized to a preoccultation value of 1.0 and a postoccultation value of 0.0. An analytic expression for each lightcurve (in terms of a sixth-order Legendre polynomial) was found by least squares.

The observed lightcurve used consists of data points at 0.01-sec intervals, normalized so that before the occultation the signal = 1.0 and after the occultation, the signal = 0.0 (cf. Elliot *et al.*, 1975).

Each model lightcurve, in its analytic form, was fitted by least squares to the observed lightcurve to determine the single parameter, T, the duration of the occultation in seconds, and the statistical (one-sigma) uncertainty in T: ΔT.

In the notation of Elliot *et al.* (1975), the duration of the occultation, T (sec), is related to the radius of the satellite, R (km), by

$$R = \tfrac{1}{2} \cdot C \cdot \rho \cdot \Delta_s \cdot T, 206\,265,$$

where Δ_s = distance of the occulted satellite from the Earth = 9.14 AU, ρ = radial rate of advance of the mean lunar limb = 0.3970 arcsec/sec, and C = correction factor to ρ = 1.0.

The results of such calculations for the models discussed in Section 3 are given in Table I, first for the simple uniform hemisphere models and second for the model of Morrison *et al.* (1975). The results of this section are not sensitive to whether we specify the limb darkening of the bright material according to (1) or (2). For example, from Fig. 3 we see that $b = 0.5$ corresponds approximately to $k \sim 0.7$; Table I shows that the inferred radius for $k = 0.7$ is practically identical to that inferred for $b = 0.5$. This fact is generally true for corresponding values of k and b. We note that the errors quoted in Table I represent statistical errors only, determined from the signal-to-noise characteristics of the occultation data (cf. Elliot *et al.*, 1975).

TABLE I

RADII OF IAPETUS DERIVED FROM THE OCCULTATION DATA OF ELLIOT *et al.* (1975)

A. Hemispherical models			
k	R (km)	b	R (km)
0.5	698 ± 58	0.00	698 ± 58
0.6	714 ± 60	0.25	709 ± 59
0.7	738 ± 63	0.50	734 ± 62
0.8	762 ± 65	0.75	765 ± 65
1.0	798 ± 69	1.00	798 ± 69
$I(\eta) = \cos^{2k-1}\eta$		$I(\eta) = (1-b) + b\cos\eta$	

B. Patchy model	
Albedo distribution	R (km)
From Morrison *et al.* (1975); cf. Fig. 2	724 ± 60

In Section 3 we concluded that for the bright material $k = 0.62^{+0.10}_{-0.12}$; hence, from Table I, we infer that for Iapetus

$$R = 718^{+67}_{-73}\ \text{km},$$

which is consistent with the nominal radiometric value of 835 (+50, −75) km quoted by Morrison *et al.* (1975).

The specific albedo model for the bright side of Iapetus proposed by Morrison *et al.* (cf. Fig. 2) gives a radius of

$$R = 724 \pm 60\ \text{km}.$$

Since the albedo distribution on the bright side is asymmetric in this model, the orientation of the spin axis of Iapetus relative to the lunar limb at the time of the occultation had to be considered in this calculation. Note that this value for the radius is consistent with those given by the simple two-faced models which have $k \sim 0.64$ or $b \sim 0.4$ (Table I).

Although the Morrison *et al.* surface albedo model (Fig. 2) does reproduce the orbital lightcurve exactly, it is not unique and hence need not represent the true albedo distribution on Iapetus precisely. However, from the discussion in Section 3 it is clear that the true albedo distribution can differ from that in Fig. 2 only to the extent that the average limb darkening on the bright side remains within the range 0.5 to 0.8. According to Table I, $k > 0.5$ implies $R > 640$ km, while $k < 0.8$ implies $R < 827$ km. Thus, it appears unlikely that the true radius of Iapetus can differ from that derived for the Morrison *et al.* albedo model, by more than about ±100 km. Therefore, conservatively, we adopt 724 ± 100 km as the nominal *lunar occultation radius* of Iapetus.

5. RIM MODELS

Since the radiometric radius of Iapetus is slightly larger than our occultation value, we investigated various special models which could conceivably produce larger occultation radii. For example, we considered a series of *dark-rim models* in which a rim of dark leading-side material is seen as an annulus around the limb when the bright side is viewed at $\theta = 270°$. We assumed that the dark rim material does not show limb darkening, while the bright material is limb darkened according to $\cos^{2k-1}\eta$. Once again the lightcurve amplitude fixes the ratio of the normal reflectances of the bright and dark materials $B_n(\text{bright})/B_n(\text{dark})$ for any specific value of k(bright). Evidently, for k fixed, the above ratio increases as the width of the rim increases, and for a fixed rim width the ratio increases as k increases.

Although the addition of a significant dark rim can increase the occultation diameter appreciably (Table II), none of the rim models considered came close to matching the lightcurve.

We considered models with rims extending 10, 30, 40, and 50° from the limb and found that any rim in excess of 10° is grossly inconsistent with the observed lightcurve for all values of k between 0.5 and 2.0. The best agreement with the lightcurve was obtained for a 10° rim with $k \simeq 0.5$ on the bright side. Data points corresponding to this model are shown in Fig. 4; it is evident that the agreement with the observed parameters is not good. Also shown in Fig. 4 are data points for a 30° rim model with $k = 0.5$. This model is absolutely unacceptable. It should be noted that the agreement becomes even worse if $k > 0.5$ is used in the 30°-rim model.

TABLE II

OCCULTATION RADII DERIVED FOR RIM MODELS

Rim extent[a] (deg)	Radius[b] (km)
10	704 ± 58
30	780 ± 65
40	873 ± 72
50	989 ± 88

[a] Measured from limb.
[b] Assuming $k = 0.5$ for both the dark and bright materials (see text).

6. OTHER EFFECTS

At the time of the occultation the solar phase angle of Iapetus was $\alpha = 6°.26$, a fact neglected in the preceding analysis. Using the precise occultation geometry of the event, we computed occultation lightcurves at $\alpha = 6°.26$ for the two cases of a uniform bright side limb darkened as $k = 0.5$ and $k = 1.0$. The radii derived from these occultation lightcurves were compared with the corresponding values calculated under the $\alpha = 0°$ assumption. In both cases the difference (1.36 km for $k = 0.5$, and 0.1 km for $k = 1.0$) was considerably less than our error bars, and we conclude that our previous analysis is not affected by our neglect of the small nonzero phase of Iapetus at the time of the occultation.

ORIGINAL PAGE IS OF POOR QUALITY

7. NORMAL REFLECTANCE AND GEOMETRIC ALBEDO

From an independent analysis of the occultation data Elliot *et al.* (1978), derive 0.60 ± 0.14 for the normal reflectance (r_n) of the bright-side material in V. Since $k = 0.62^{+0.10}_{-0.12}$, we have for the geometric albedo of the bright side (Veverka, 1977)

$$p_v = \frac{r_n(V)}{k + \frac{1}{2}} = \frac{(0.60 \pm 0.14)}{0.62^{+0.10}_{-0.12} + 0.5} = 0.54^{+0.20}_{-0.16}.$$

From the observed lightcurve amplitude we know that

$$p_v(\text{bright side})/p_v(\text{dark side}) = 5,$$

so that $p_v(\text{dark side}) = 0.11^{+0.04}_{-0.03}$.

If, as assumed, the dark side shows no limb darkening, then for the dark side

$$r_n(V) = p_v = 0.11^{+0.04}_{-0.03}.$$

We now compare our values of the normal reflectances with those derived by Morrison *et al.* (1975). According to the caption of Fig. 7 (our Fig. 2) of Morrison *et al.* the geometric albedos in V for the "bright" and "dark" material are 0.35 and 0.05, respectively. However, T. J. Jones (private communication) informs us that these values refer to *normal reflectances* and not to geometric albedos. Thus for the bright material the normal reflectance of 0.35 derived by Morrison *et al.* is to be compared with our value of 0.60 ± 0.14. For the dark material, their value of 0.05 is to be compared to our $0.11^{+0.4}_{-0.3}$.

Thus although the occultation radius and the radiometric radius agree within their stated error bars, the normal reflectances derived by Morrison *et al.* are at most marginally consistent with our values. Our analysis indicates that both the "bright" and the "dark" materials are brighter than supposed by Morrison *et al.*

8. THE MEAN DENSITY OF IAPETUS

The mass of Iapetus is only poorly determined from perturbations on Titan (Struve, 1933). The formal result ($1.4 \pm 0.7 \times 10^{24}$ g) corresponds to about 2% of a lunar mass. Combined with the occultation radius based on the albedo model of Morrison *et al.* (724 ± 60 km), we obtain a mean density of 0.9 (+0.9, −0.5) g/cm^3, a result consistent with Iapetus being an icy object. However, the uncertainties are too large at present to place any useful constraints on the bulk composition of the satellite.

9. SUMMARY AND CONCLUSIONS

From the oribtal lightcurve of Iapetus we find that the bright material on the trailing face of the satellite has an effective limb-darkening parameter of $k = 0.62^{+0.10}_{-0.12}$. Given this fact, we can use the observations of the March 30, 1974, occultation of Iapetus by the Moon (Elliot *et al.*, 1975) to derive the radius of the satellite. The result is $R = 718^{+37}_{-75}$ km.

The specific patchy albedo model proposed by Morrison *et al.* (Fig. 2) fits the observed orbital lightcurve precisely and yields an occultation radius of 724 ± 60 km. We note that as far as fitting the observed orbital lightcurve is concerned it is the relative albedos in Fig. 2 that are important, and *not* the absolute values. In fact, it appears from the work of Elliot *et al.* (1978) that the absolute values of the albedos shown in Fig. 2 are all too low. Elliot *et al.* find the normal reflectance of the bright material to be 0.60 ± 0.14 in V, and not 0.35 as shown in Fig. 2. A value of $r_n(V) = 0.60 \pm 0.14$ for the bright material implies that for the dark material $r_n(V) = 0.11^{+0.04}_{-0.03}$ (Section 7) and not 0.05 as shown in Fig. 2.

We note that the values of $p_v = 0.60 \pm 0.14$ and $k = 0.62^{+0.10}_{-0.12}$ are consistent with a partial water frost cover on the bright side of Iapetus (McCord *et al.*, 1971; Morrison *et al.*, 1976; Fink *et al.*, 1976).

We conclude that *if* the albedo model of Morrison *et al.* turns out to represent the surface of Iapetus reliably (that is, as far

as the relative distribution of albedos is concerned, if not in terms of absolute albedos) then the radius of Iapetus is 724 ± 60 km. This value is consistent with the radiometric radius of 835 (+50, −75 km) derived by Morrison *et al.* (1975).

We stress that even though the Morrison *et al.* albedo model does reproduce the observed orbital lightcurve accurately it is not unique and need not represent the actual albedo distribution on the surface of Iapetus. Nevertheless, as we saw in Section 3, the true relative albedo distribution on the bright face of Iapetus can differ from that shown in Fig. 2 only to the extent that the average limb-darkening parameter k of the bright face remains within the range 0.5 to 0.8. This in turn implies that the true radius probably lies between 640 and 827 km; in other words the true radius can differ at most by about 100 km from the value of 724 km derived for the Morrison *et al.* model. Thus, we adopt $R = 725 \pm 100$ km as the lunar occultation radius of Iapetus, and note that if the relative albedo distribution shown in Fig. 2 is correct, then the radius lies within 724 ± 60 km.

ACKNOWLEDGMENTS

We are grateful to D. Morrison and T. J. Jones for helpful comments and discussions. This work was supported by NASA Grants 33-010-082 and NSG 7126, and NSF Grant MPS 75-06670.

REFERENCES

Cook, A. F., and Franklin, F. A. (1970). An explanation of the light curve of Iapetus. *Icarus* 13, 282–291.

Dollfus, A. (1970). Diametres des planetes et satellites. In *Surfaces and Interiors of Planets and Satellites.* (A. Dollfus, Ed.), pp. 45–139. Academic Press, New York.

Elliot, J. L., Veverka, J., and Goguen, J. (1975). Lunar occultation of Saturn. I. The diameters of Tethys, Dione, Rhea, Titan and Iapetus. *Icarus* 26, 387–407.

Elliot, J. L., Dunham, E. W., Veverka, J., and Goguen, J. (1977). Lunar occultation of Saturn. II. The normal reflectances of Tethys, Dione, Rhea, Titan and Iapetus. *Icarus* 35, in press.

Fink, U., Larson, H. P., Gautier, N., and Treffers, R. (1976). Infrared spectra of the satellites of Saturn: Identification of water ice on Iapetus, Rhea, Dione, and Tethys. *Astrophys. J.* 207, L63–L67.

Franklin, F. A., and Cook, A. F. (1974). Photometry of Saturn's satellites: The opposition effect of Iapetus at maximum light and the variability of Titan. *Icarus* 23, 355–362.

McCord, T. B., Johnson, T. V., and Elias, J. H. (1971). Saturn and its satellites: Narrow-band spectrophotometry (0.3–1.1 microns). *Astrophys. J.* 165, 413–424.

Millis, R. L. (1973). UBV photometry of Iapetus. *Icarus* 18, 247–252.

Morrison, D. (1973). Determination of radii of satellites and asteroids from radiometry and photometry. *Icarus* 19, 1–14.

Morrison, D., Jones, T. J., Cruikshank, D. P., and Murphy, R. E. (1975). The two faces of Iapetus. *Icarus* 24, 157–171.

Morrison, D., Cruikshank, D. P., Pilcher, C. B., and Rieke, G. H. (1976). Surface compositions of the satellites of Saturn from infrared photometry. *Astrophys. J.* 207, L213–L216.

Noland, M., Veverka, J. Morrison, D., Cruikshank, D. P., Lazarewicz, A., Morrison, N., Elliot, J., Goguen, J., and Burns, J. (1974). Six-color photometry of Iapetus, Titan, Rhea, Dione and Tethys. *Icarus* 23, 334–354.

Pilcher, C. B., Ridgeway, S. T., and McCord, T. B. (1972). Galilean satellites: Identification of water frost. *Science* 178, 1087–1088.

Russell, H. N. (1906). On the light variations of asteroids and satellites. *Astrophys. J.* 24, 1–18.

Struve, G. (1933). Quoted in Brouwer, D., and Clemence, G. M. (1961). Orbits and masses of planets and satellites. In *Planets and Satellites* (G. Kuiper and M. Middlehurst, Eds.), pp. 31–94. Univ. of Chicago Press, Chicago.

Veverka, J. (1973). The photometric properties of natural snow and of snow-covered planets. *Icarus* 20, 304–310.

Veverka, J. (1977). Photometry of satellite surfaces. In *Planetary Satellites* (J. Burns, Ed.), pp. 171–209. Univ. of Arizona Press, Tucson.

Veverka, J., Goguen, J., Yang, S., and Elliot, J. L. (1978). Near-opposition limb darkening of solids of planetary interest. *Icarus* 32, 368–379.